Optical engineering of colour centres in diamond

Andrew R. Kirkpatrick

Wolfson College

University of Oxford

A thesis submitted for the degree of

Doctor of Philosophy

February 10, 2023

Abstract

Ultrafast laser fabrication of NV^- centres has been shown to produce highly coherent NV^- centres within diamond with high fabrication accuracy, expanding the applicability of the defect within quantum technologies. However this technique is yield limited due to a required thermal annealing step. Within, this thesis presents the first, near-unity yield, fabrication of single NV^- centres in commerically available high purity diamond using a homebuilt ultrafast fabrication system. Thermal annealing is replaced by a low energy ultrafast pulse train which allows for NV^- generation to be monitored using confocal fluorescence microscopy. Each fabrication site showed a $g^{(2)}(0) < 0.5$, demonstrating singularity. The fabrication precision has been calculated to be isotropically $\sim$250 nm, suggesting that nitrogen concentration is the limiting factor. This thesis details the construction and operating principles of the homebuilt fabrication system, which includes the use of adaptive optic elements. Additionally this thesis investigates phenomena observed during ultrafast farbication of NV^- centres using *ab initio* calculations of defect interactions within diamond. These simulations suggest that hybridisation may be responsible for transient effects seen during fabrication. In addition, these simulations demonstrate that the ultrafast laser fabrication of defects may provide an invaluable window into defect formation and fabrication in the solid state.

Optical engineering of colour centres in diamond

Andrew R. Kirkpatrick

Wolfson College

University of Oxford

A thesis submitted for the degree of

Doctor of Philosophy

February 10, 2023

For kicking me out of the house when I was 18,

Mum & Dad,
Kuldip & Ian Kirkpatrick.

Acknowledgements

The recent years of researching at the University of Oxford have been amongst my most enjoyable and I have had the pleasure to meet and work with many fantastic people. Namely I would like to thank the members, past and present, of the Photonic Nanomaterials Group and the Dynamic Optics and Photonics Group; in particular Shazeaa Ishmael, Shannon Nicley, Gareth Jones, Jonas Becker, Amit Dhawan, Jiahe Cui and John Standford-O'Neill for being a constant source of joy both in and out of the lab. I would like to give special thanks to Matt Mai, who has been by my side throughout my whole DPhil, through highs and lows, whose friendship and encouragement truely shaped the scientist I am today. At Wolfson College I would like to thank Ryan, Tom, John and Grigore and the porters Steve, Joe, Ant and Jerry. Additionally I would like to thank my supervisors Jason Smith and Martin Booth, not only for their supervision and assitance but for their patience and friendship throughout my DPhil. In particular, I would like to give thanks to Patrick Salter for his thoughtful lessons, companionship and for keeping up with me in the pub. Speaking of pubs it would be amiss to not thank the staff and establishment of the Royal Oak for providing the home for many of our research ideas. This is not to say I shouldn't thank other pubs in Oxford but we really would be here all day.

Adjunct to the groups at Oxford are those at Warwick and I would like to give thanks to Yashna Lekhai, Joe Gore, Colin Stephens, James Brixey, Guy Stimpson, Ben Green, Gavin Morely and Mark Newton. All of whom have been fantastic collaborators and teachers throughout my research. This is an appropriate place to also thank the Diamond Science and Technology, Centre for Doctoral Training for teaching me the skills to really succeed in my DPhil and for providing an incredible environment for collaboration and training. Additionally, I would like to thank EPSRC and De Beers for their funding of this project and in particular David Fisher and Phil Diggle. Thanks also go to Element 6 for their support with samples. Finally, I would like to thank the QCS Hub and its members.

Most of all I would like to thank my friends, the majority of whom might not get the whole academia thing, but have never the less been a bottomless source of

emotional, mental and on rare occasions spiritual strength. These include friends from home; James, Jordan, Hannah, Ethan, Emma, Anthony, Malcolm, Olivia and John. Friends from the Bromfield; Cari, Ben, Hector, Connah, Guy and Helen. And a friend who passes etherially without place but is always one letter away; John Davies. I would also like to thank my dearest friend, Jade Tiplady-Taylor, for her patience and understanding. Last, but by no means least, I would like to thank my childhood dunga heads Sunita and James Kirkpatrick. To both of you, know that every word was written with the love that you gave me.

Thank you.

Abstract

Ultrafast laser fabrication of NV^- centres has been shown to produce highly coherent NV^- centres within diamond with high fabrication accuracy, expanding the applicability of the defect within quantum technologies. However this technique is yield limited due to a required thermal annealing step. Within, this thesis presents the first, near-unity yield, fabrication of single NV^- centres in commerically available high purity diamond using a homebuilt ultrafast fabrication system. Thermal annealing is replaced by a low energy ultrafast pulse train which allows for NV^- generation to be monitored using confocal fluorescence microscopy. Each fabrication site showed a $g^{(2)}(0) < 0.5$, demonstrating singularity. The fabrication precision has been calculated to be isotropically $\sim$250 nm, suggesting that nitrogen concentration is the limiting factor. This thesis details the construction and operating principles of the homebuilt fabrication system, which includes the use of adaptive optic elements. Additionally this thesis investigates phenomena observed during ultrafast farbication of NV^- centres using *ab initio* calculations of defect interactions within diamond. These simulations suggest that hybridisation may be responsible for transient effects seen during fabrication. In addition, these simulations demonstrate that the ultrafast laser fabrication of defects may provide an invaluable window into defect formation and fabrication in the solid state.

List of Publications

Journal articles

1. *Microscopic Processes During Ultra-Fast Laser Generation of Frenkel Defects in Diamond*, B. Griffiths, **A. R. Kirkpatrick**, S. Nicley, R. Patel, J. Zajac, G. Morley, M. Booth, P. Salter, J. Smith, Physical Review B, 104 (2021) - Many of the arguments within Chapters 5 and 6 are based upon this article.

2. *Generalised adaptive optics method for high-NA aberration-free refocusing in refractiveindex-mismatched media*, J. Cui, J. Antonello, **A. R. Kirkpatrick**, P. S. Salter, and M. J. Booth, Optics Express, 30 (2022) - Many of the arguments within Chapter 5 are based upon this article.

3. *Visible light emissions during flash sintering of 3YSZ are thermal radiation*, C. Bechteler, **A. R. Kirkpatrick**, R. I. Todd, Scripta Materialia, http://dx.doi.org/10.2139/ssrn.4102466 (2022)

4. *Defect interactions during ultra-fast laser writing of NV centres in diamond*, **A. R. Kirkpatrick**, G. Chen, J. Brixey, H. Witkowska, P. Salter, M. Booth, J. Smith, *Manuscript in preparation* - Many of the results of Chapter 6 are found within this article.

5. *Deterministic fabrication of NV^- centres in high purity diamond*, **A. R. Kirkpatrick**, S. N. Ishmael, G. Chen, M. F. Mai, G. S. Jones, P. S. Salter, M. J. Booth, J. M. Smith, *Manuscript in preparation* - Many of the results of Chapter 7 are found within this article.

Conference presentations

1. **32^{nd} International Conference on Diamond and Carbon Materials:** *Deterministic creation of single NV centres in high purity diamond*, Sep. 2022

2. **De Beers 72nd Diamond Conference:** *Deterministic fabrication of single NVs within high purity diamond*, Jul. 2022

3. **Invited Seminar; Michigan State University:** *Ultrafast laser fabrication of NV centres in diamond*, May 2022

4. **MRS Fall Meeting:** *Ultrafast laser fabrication of NV centres in diamond*, Nov. 2021

5. **De Beers 71st Diamond Conference:** *Defect interactions during ultrafast laser writing of NV centres in diamond*, Jul. 2021

6. **Quantum Technology International Conference 2020:** *Ultrafast laser fabrication of NV centres in diamond*, Nov. 2020

7. **IOP Photon 2020:** *Ultrafast laser fabrication of NV centres in diamond*, Sep. 2020

8. **Invited Seminar; Universitë Paris-Saclay, Paris:** *Ultrafast laser fabrication of NV centres in diamond*, Sep. 2020

9. **De Beers 70th Diamond Conference:** *Adaptive optics for cavity coupled NV centres to make efficient spin-photon interfaces*, Jul. 2019

10. **Oxford Photonics Day:** *Engineering the optical properties of Diamond: Towards an efficient spin-photon interface*, Apr. 2019

Patents

1. Patent Contributor; PCT/GB2019/052820 *Laser method and apparatus of analysing crystals*, Filed October 2018, Pending.

Contents

List of Figures

List of Abbreviations

1-D, 2-D, N-D	One-, two- or N-dimensional.
AO	Adaptive optics.
AOM	Acousto-optic modulator.
CVD	Chemical vapour deposition.
CW	Continuous wave.
DFT	Density functional theory.
DPSSL	Diode-pumped solid-state laser.
FPGA	Field programmable gate array.
FWHM	Full width half maximum.
GGA	Generalised gradient functional.
HPHT	High pressure, high temperature.
LDA	Local density functional.
MPI	Multiphoton ionisation.
NA	Numerical aperture.
NCP	Norm-conserving pseudopotentials.
NV^x	The nitrogen-vacancy centre in diamond, where x refers to the centre's charge state.
PL	Photoluminescence.
RF	Remote focusing.
RIM	Refractive index mismatch.
SHG	Second harmonic generation.
SLM	Spatial light modulator.
SPAD	Single photon avalanche detector.
USP	Ultra-soft pseudopotentials.
ZPL	Zero phonon line.

Chapter 1

Introduction

1.1 Solid state colour centres

At the turn of the 20$^{\text{th}}$century, colour centres in various wide band gap materials have emerged as a versatile set of systems capable of generating single photons, sensing magnetic fields and providing a photonic interface for quantum entagled systems. These discoveries were being made with defects in crystals that had been otherwise thouroughly characterised. The negatively charged Nitrogen-Vacancy (NV^-) centre in diamond, the defect in focus within this thesis, was among the first of these defects and within a handful of years was the first demonstration of loophole-free quantum entanglement.[1]

Solid state colour centres quickly became one of the most promising candidates for quantum systems technologies and with good reason. They provided an optical interface for initilisation and readout of a qubit,[2] all whilst achieving record spin coherence properties. They showed applications in quantum key distribution and information processing as they were potentially a stable source of single photons.[3] A key notch in colour centre's belt was their host medium. With entanglement processes being sensitive to environmental noise, the ability to produce qubits

within an otherwise defect-free, low noise, environment allowed colour centres to maintain excellent spin and optical coherence properties.

The field has now been able to evolve with a focus on producing defect-engineered materials and devices. This includes a shift in commerical synthetic diamonds which have made high quality material more accessible for academic research and industry. The solid state naturally allows for the potential of scalable devices, a key step in the impact of any technology. Additionally the vast history of crystollographic research has lead to the convergence of many research fields. For example, lithographic fabrication has lead to the creation of resonance structures[4–9] and solid immersion lenses[10] within the mediums that can play host to these new quantum interfaces.

1.2 Engineering the NV^- centre in diamond

Diamond crystals tick a lot of the boxes outlined above. Their basic building block is the spinless ^{12}C with a natural abundance of 98.9%. In addition, they are a host to over 500 optically active impurities,[11] made possible by the large 5.5 eV band gap. One of these, as touched on previously, was the first colour centre to be realised for quantum applications, the NV^- centre. Owing to nitrogen being the most abundant defect in synthetic diamond, it is now one of the most well studied colour centres in the solid state and remains a promising candidate for many quantum applications.

As discussed in more detail in Chapters 2 & 3, the NV^- centre exhibits spin-dependent fluorescence due to transitions within its electronic structure, resulting in an optical interface for spin. Additionally, the NV^- centre is a source of single photons, and through the use of optical cavities can be an efficient source of indistinguishable photons.

The fabrication of any NV^- centre based device needs one more ingredient, the ability to create the defect itself. Within Chapter 2 of this thesis many of these techniques are discussed and compared. However the focus of this thesis is on the fabrication of NV^- centres through the use of femotosecond laser pulses. This technique exploits non-linear processes to create highly localised, high quality NV^- centres at nearly any position within the diamond bulk. Additionally this technique is able to be combined with other optical techniques to bypass the yield limiting processes present in other techniques. This thesis demonstrates the novel generation of high quality NV^- centres in high purity diamond with a unity yield. Additionally, this thesis outlines a unique theoretical study to demonstrate how observed phenomena during fabrication can be used as a source of new insight into defect dynamics at the atomic scale.

1.3 Thesis outline

Chapter 2: Literature review

This chapter presents a detailed review of research surrounding the topics of this thesis. It begins with a historical review of colour centres and related defects in diamond. The chapter then discusses and compares other methods of NV^- fabrication, before concluding with a review into NV^- fabrication using ultrafast laser pulses.

Chapter 3: Theoretical background

This chapter outlines the various theoretical principles underlying the research presented in this chapter. There are three main topics covered in this background.

The chapter begins by presenting the theoretical principles of ultrafast laser fabrication, including a theoretical derviation of key equations used for aberration correction. Secondly, the chapter discusses the defect structure of the NV^- centre. Finally this chapter presents a overview of density functional theory (DFT) and Monte-Carlo methods which are used within Chapter 6.

Chapter 4: Experimental methods

This chapter discusses the various experimental methods used throughout the thesis. In addition, this chapter presents the various techniques used in the characterisation of the fabricated NV^- centres, including confocal microscopy, Hanbury-Brown-Twiss measurements and photoluminescence lifetime measurements. In addition, this chapter discusses the various diamond samples used themselves.

Chapter 5: Ultrafast laser fabrication system with fluorescence feedback

This chapter discusses in detail the design and build of an ultrafast laser fabrication system with an inbuilt confocal fluorescence microscope. This includes the techniques used to produce vacancies within diamond and then diffuse them to produce NV^- centres. This chapter also includes the design of an in situ confocal fluorescence microscope used to probe the laser writing process. Particular attention has been paid to the use of adaptive optics within this system, which will prove to be key in producing defects within diamond. Therein, considerable attention has been paid to the construction of a home built laser writing system for NV^- centres due to its significance in the rest of the thesis.

Chapter 6: *Ab initio* simulations of interactions between laser written defects

This chapter presents a series of density functional theory (DFT) simulations on the electronic and strain interactions between defects involved in ultrafast laser fabrication. This section shows from electronic interactions that hybridisation can occur between the carbon self-interstitial and the NV^- orbitals involved in photoluminescence. This information is then used to inform a Monte Carlo simulation to replicate experimentally observed fluorescence traces during laser fabrication.

Chapter 7: Deterministic fabrication of NV^- centres in high purity diamond

This chapter presents the deterministic farbication of single NV^- centres in commercially available high purity diamond typically used in quantum applications. This work builds heavily upon the previous chapters to demonstrate how the many challenges of this fabrication can be overcome. This chapter additionally establishes a new regime of monitoring the fabrication process since previously presented monitoring techniques are unavailable at high repetition rates. Finally this chapter concludes with several characterisations of the NV^- centres created.

Chapter 2

Literature review

2.1 Introduction

Diamond, one of the carbon allotropes, is a covalently bonded network of carbon atoms which boasts an array of interesting optical properties such as a high refractive index,[12] large bandgap[13] and minor long-wavelength absorption bands.[14] These properties mean that light extraction from the diamond is mostly limited by reflections at the surface. In addition, an isotopically pure diamond lattice provides a spin-free environment due to the zero spin of carbon-12, and even at natural abundance (98.9%) the lattice is almost spin-free.[15]

These properties provide an ideal photonic environment for diamond's colour centres,[16, 17] many of which are room temperature single photon emitters, such as the neutral and negatively charged nitrogen-vacancy (NV) centre, silicon-vacancy centre (SiV) and a host of transition metal based defects.[3] Several of these centres are being investigated for applications in photonic devices, capitalising on the natural scalability of solid state technology.[16] Research fields developing applications for these defect structures require accurate positioning of single defects within a device, often with separations of 10 nm. In order to address this demand,

ultrafast laser writing is being developed as a method of fabricating localised single vacancy-based defects within the bulk of diamond, whilst maintaining coherence properties required for quantum applications.

This chapter aims to review three fields of relevant literature. Firstly, and in order to provide context, relevant colour centres in diamond will be investigated. Secondly an exploration into several fabrication methods of vacancies and nitrogen-vacancies will be used to set a foundation to introduce the third topic of ultrafast laser writing.

2.2 Colour centres in diamond

2.2.1 Substitutional vacancy

Studies into the diamond vacancy began with investigations on an unattributed optical feature seen in diamond samples exposed to radiation, historically labelled as GR1. In a comprehensive survey of fifty-two type I (nitrogen concentraion, [N]>1 ppm) and II ([N]<1 ppm) diamonds, Clark *et al.*[18] demonstrated that neutron, electron and γ radiation all lead to generation of the GR1 feature at approximately 1.6eV. Previously in 1953, Dugdale[19] had already suggested that this feature is likely to be due to the generation of vacancies and interstitials. This model was developed in 1957 by Coulson *et al.*[20], where it was assumed that the electronic character of the defect is determined by dangling bonds pointing into the vacancy. From this Coulson *et al.* predicted a $^1E \rightarrow ^1 T_2$ transition. Evidence that the GR1 optical feature is a signature of the lattice vacancy grew in 1973 when Clark *et al.*[21] studied the feature using optical absorption and uniaxial stress measurements. The study was able to assign tetrahedral symmetry with the defect, which was consistent with previously unpolarised emission[22]. In addition the

study assigned the previously predicted $^1E \rightarrow^1 T_2$ state with the 1.673 eV (741 nm) transition and the 1.653 eV (750 nm) feature with a $^1A \rightarrow^1 T_2$ transition. Finally a unified argument for the assignment of spectral features was presented by Davies in 1977,[23] where it was argued that GR1 and ND1 are neutral and negative charge states of vacancy from their symmetry, charger transfer and production in different diamond types. Determining whether a subtitutional vacancy is a single photon emitter or not presents difficulty due to its long radiative lifetime and short non-radiative components.[24] Regardless, it is a fundamental building block in many single photon sources in diamond.

2.2.2 Nitrogen-vacancy centre

The nitrogen-vacancy (NV) centre, particularly the NV^- charge state, is currently the focus of many research fields from solid state quantum computing[3] and sensing[15]. The formation of the NV^- was first presented in the PhD thesis of du Preez in 1965.[25] du Preez discovered the optical signature of the centre at 1.95 eV following radiation damage and annealing of type Ib diamond, a classification of diamond known for its high substitutional nitrogen concentration. The assertion that this optical feature was produced by the NV^- was corroborated with its inverse relationship between the emission from the lattice vacancy, suggesting that this new feature incorporated a lattice vacancy in some way. Further photoluminescence polarisations[22] and uniaxial stress[26] studies on the optical feature were consistent with its attribution to the NV^- centre by discovering trigonal symmetry and an associated $A_1 - E$ electric dipole transition.

The confirmation of the association between the 1.95 eV feature and the NV^- centre was first discovered by Loubser and van Wyk in 1977[27] through electron

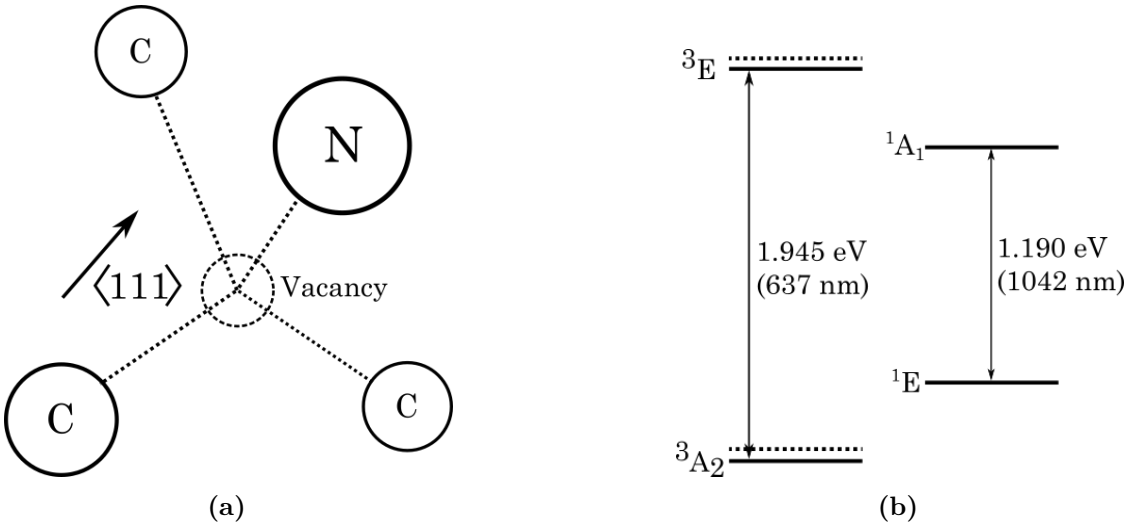

Figure 2.1: (a) Schematic diagram of the structure of the NV defect in diamond as proposed by Loubser and van Wyk in 1977.[27] (b) The electronic structure of the NV^- defect centre[31] the dashed lines on the triplet states represent the degenerate $m_s = \pm 1$ states.

paramagnetic resonance (EPR) of irradiated diamond. Loubser and van Wyk also expanded upon the first proposal of the electronic structure of the NV^- through their observation of a ^3A triplet state which established the model of a six electron structure, where five electrons occupied nitrogen and carbon dangling bonds surrounding a vacancy and the sixth electron, likely from a nearby donor, formed the negative charge state.[27] This model can be seen schematically drawn in figure 2.1a. Lenef and Rand[28] proposed a counter model based upon *ab initio* simulations where the observed defect was neutrally charged, however this model has since been disproven.[29, 30]

Further work by van Oort *et al.*[32] in 1988 determined that the $^3A_2$ state is the ground state, which has a zero-field splitting of 2.88 GHz. Following from this research the electronic energy level order was derived to be $^3A_2$, $^1A_1$, ^1E and ^3E,[33] as shown in fig. 2.1a. Following from this assignment, two important optical properties were discovered; firstly that there exists an inter-system crossing

between the ^{3}E and ^{1}A$_1$ and that the zero-phonon line (ZPL) of the NV$^-$ at 637 nm (1.95 eV) indicates a transition between ^{3}A$_2 \rightarrow ^3$E ($m_s = 0$).[26] Electrons that transition between the $m_s = \pm 1$ states have a $\leq$30% probability of decaying through through the inter-system crossing and into the $m_s = 0$ state of the ^{3}A$_2$ level.[34] This leads to a transition between the ^{1}A$_1$ and ^{1}E states that can be detected by a 1042 nm photoluminescence feature.[35]

These series of discoveries lay the foundation of why the NV$^-$ centre is applicable to quantum computing. The previous discoveries lead to three important conclusions:

1. The initial spin state of the electron, $m_s = 0$ or $m_s = \pm 1$, effects the probability of the decay route through the band structure.

2. The two decay mechanisms have different optical signatures.

3. Regardless of the transitions an excited electron makes through the NV$^-$ band structure, it will preferentially return to the $m_s = 0$ spin state.

It is at this point that the motivation behind the NV$^-$ is identifiable. The spin dependent fluorescence of the NV$^-$ means that a purely optical initialisation and read-out of the electron spin states is possible, providing a powerful interface to control a solid state qubit. However applications that take advantage of the NV$^-$ centre's spin properties, such as quantum computing, additionally require the spin to be coherent over time. Coherence time is typically reduced by interactions with other spins, typically coming from the nuclear spin of defects or, in the case of diamond, ^{13}C.

The research conducted by van Oort *et al.* was the first to present spin coherence experiments of the NV$^-$, reporting a coherence time of 41 μs. Since then spin

coherence studies of the NV^- centre have become necessary when discussing the centre's application, reporting coherence times of usually 130 - 250 μs.[36–39] Eventually leading to the NV^- centre demonstrating a long room temperature dephasing time of 0.5 - 2 ms in isotopically pure diamond,[15, 40] due to the reduction of ^{13}C spins. It is also important to note that the other charge states of the NV centre do not exhibit this spin-orbit structure, so optical control of those spins is not possible. The NV^- centre does suffer from spectral broadening caused by phonon interactions that de-phase the spin state.[16] However, research efforts have been made to increase the emission into the ZPL through the use of cavity coupling.[41, 42]

2.2.3 Silicon-vacancy centre

The SiV centre structure was confirmed by electron paramagnetic resonance as an interstitial silicon atom occupying a space between two vacancies,[43] as shown in fig. 2.2. This structure is the most common (and arguably the only conclusively identified) silicon based defect in diamond and is usually formed during chemical vapour deposition of diamond where silicon substrates or quartz windows are used.[16] SiV concentration is also observed in silicon ion implantation.[16]

In comparison to the NV^-, the SiV^- centre has demonstrated bright, narrow optical transitions with a small inhomogeneous broadening.[44, 45] In addition, the inversion symmetry of the defect, which prevents an efficient coupling between electronic and vibrational energy states, protects its optical coherence.[46, 47] However spin coherence is limited to 100 ns at 4 K[48–52] but can be extended to 13 ms at 0.1 K.[53] This is due to phonons, which do not freeze out at these temperatures, coupling with the orbital doublet ground state.[50] The room temperature coherence

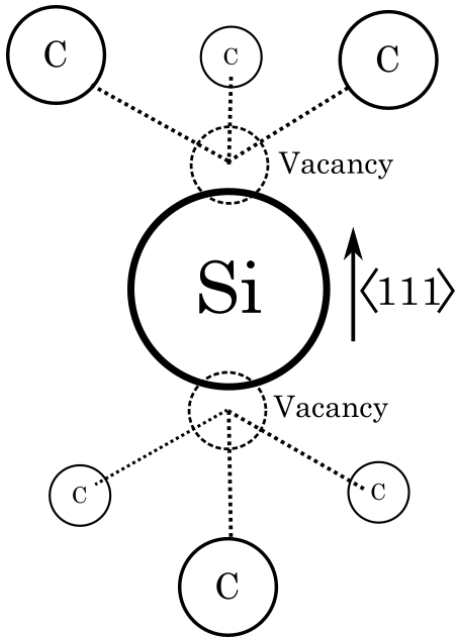

Figure 2.2: Schematic diagram of the structure of the SiV defect in diamond.

times is much less than those reported previously for the NV^- centre due to coupling to the phonon bath which is mediated by spin-orbit coupling.[48, 49, 54–56]

The neutral charge state of the SiV centre has recently been demonstrated to be a potential candidate for solid state quantum computing applications. Green *et al.* demonstrated that low-temperature ensemble coherence times can reach T_2 >100 μs whilst being able to be optically addressed independently from a NV^- defect in the same focal volume due to the 946 nm ZPL of the neutral SiV, which has implications for entangled photonic spin systems.[57] Spin initialisation was accomplished through optical excitation, and spin initialisation and readout was accomplished with an Electron Paramagnetic Resonance (EPR) spectrometer. The ability of initialising SiV and NV centres has been developed further and may represent a powerful tool in quantum computing applications.[58] Low temperature, long coherence times have been reported by Rose *et al.* as T_2 =1 ms at 4 K.[59]

The SiV^0 centre therefore demonstrates the ability to overcome the short falls

of the SiV^- centre whilst maintaining the long coherence times demonstrated by the NV^- centre. A similar conclustion can be drawn for other split vacancy defects in diamond such as the tin-[60] and nickel-vacancy[61] centres. There are issues in any practical implementation of SiV^0 devices since its ZPL emission which falls uncomfortably between the detection limits of Si and InGaAs detectors, and efficient implementation would likely require the use of superconducting detectors.[62]

2.3 Methods of nitrogen-vacancy fabrication

The fabrication of well localised NV^- centres is not a novel outcome of ultrafast laser fabrication and, prior to its conception, other techniques have been used to achieve this goal. Therefore, a review of these methods is required in order to provide context to ultrafast laser fabrication and highlight the advantages of the technique.

2.3.1 Chemical vapour deposition

Diamond is a meta-stable material at room temperature and requires high temperatures and pressures to grow by conventional thermodynamic processes.[63] Diamond can be formed kinetically by the deposition of hydrocarbon radicals.[64, 65] In 1967, Angus *et al.*[66] discovered that by using a hydrocarbon gas mixture the hydrogen radicals preferentially etch any graphitic carbon created, allowing for diamond phase carbon to be the only stable phase during growth. Generally two methods of CVD are commonly used, the simplest of the two uses a hot filament to radicalise the hydrocarbon gas. However in 1977, Argoitia *et al.*[67] discovered that this often results in filament materials being deposited in the grown diamond,

damaging the spin-free environment. Therefore the second method, involving a microwave cavity to radicalise the gas, is used for diamond growth.[68, 69]

This technique has been shown to demonstrate a high degree of control in diamond growth, allowing refinement of crystal size,[16, 65] and dopant concentration.[70, 71] Such a technique is especially beneficial for single emitters inside of diamond nanoparticles, whose emissive properties can be subject to quantum confinement. However, the ability to fabricate colour centres within diamond in a scalable, controlled and high-yield manner remains challenging.[16]

In 2014, Michl *et al.*[72] and Lesik *et al.*[73] demonstrated that CVD growth techniques are capable of generating highly orientated NV^- ensembles along the (111) crystallographic plane. Lesik in particular reports coherence times of T_2 =191 μs. This was then developed further by Ozawa *et al.*[74] who demonstrated growth of NV^- in concentrations up to two orders of magnitude higher than previously reported. Most recently, in 2019 Osterkamp *et al.*[75] discovered that annealing CVD grown NV^- in vacuum at 1500 °C can increase the coherence time and density of the NV^- with the cost of a 34% loss of preferential orientation. Apart from the (111) crystallographic face, Edmonds *et al.* discovered in 2012 that NV^- have a preferential orientation in the (110) grown diamond.[76] Preferential orientation is beneficial for magnetometry applications because Optically Detected Magnetic Resonance (ODMR) contrast is reduced with random orientation.[77]

To the credit of chemical vapour deposition, there remains some promise in the ability to fabricate nickel-nitrogen based single photon emitters.[78] It is the current state of the field that the best way to deterministically create colour centres within diamond is through post-growth processes and not *in situ* during the growth phase.

2.3.2 Ion implantation

When energetic ions penetrate the surface of a solid they will create well understood cascade patterns through the solid.[79] Such collisions will lead to the generation of single vacancies and dislocations throughout the cascade path. Meijer *et al.* demonstrated that ion implantation with 2 MeV $^{14}N^{+}$ ions followed by a 1150 K, 3 hour anneal can produce single NV^{-} centres in high purity diamond to a depth of 1 ± 0.5 μm.[80] In addition, they reported that there was a 50% efficiency between the number of ions implanted and NV^{-} centres generated. Rabeau *et al.* criticised this technique, proposing that it was unable to determine if the NV^{-} centres generated were due to implanted ions or the small native nitrogen concentration in diamond. Following from this research, Rabeau *et al.* demonstrated that by implanting with $^{15}N^{+}$ ions one could distinguish implanted nitrogen atoms from the native nitrogen concentration by hyperfine methods, which exploited the different nuclear spins of the nitrogen isotopes.[81] They found that the efficiency of NV^{-} generation fell to 2.5 ± 0.6 %,[81] however there are sufficient differences between the Rabeau *et al.* and Meijer *et al.* techniques such that a direct comparison is complicated.

A number of techniques have been developed in order to improve the fabrication precision of ion implantation techniques, including using focused ion beams[82] or ion implantation with low energy nitrogen ions through a pierced atomic force microscope tip.[83]. Whilst these techniques improve fabrication accuracy to $100-150$ nm and 25 nm respectively, they have been criticised as not being scalable to larger devices. In order to address this, various mask based fabrication schemes have been developed which use apertures in acrylic[84–86] or nano-channels in mica[87] to achieve 30 nm resolution. Additionally, Becker *et al.* demonstrated that a modified

scanning electron microscope can be used to implant nitrogen into diamond, which permits the use of PMMA masks to reduce the implantation region.[88]

A limitation of using masks during the fabrication process is that they preclude the implantation of ions within nanostructures, reducing the application of the technique in devices. In addition, the yield of these devices are limited to 1−5 %, however dynamic annealing during co-implantation can enhance yield to 25 %.[89] Regardless of the implementation, the T_2 coherence time of NV^- centres fabricated by ion implantation have either been poor (<20 μs) or not reported.[80, 82, 84, 90] There are examples of ^{12}C implantation achieving T_2 >300 μs, however these times require using both δ-doped nitrogen layers and nanoscale apertures on the surface.[91]

In 2018 van Dam *et al.* reported experimental data of the optical linewidths of NV^- centres generated by ion implantation with ^{15}N.[92] They found that the optical linewidths, which is a measure of the defect's excited state lifetime, of NV^- centres created by implanted nitrogen (>1 GHz) was significantly higher than that of native nitrogen NV^-(<500 MHz). Linewidths fundamentally determined by the excited state lifetime of the emitter, however they can be broadened by effects such as strain, temperature or fast spectral diffusion. In addition, their results found that ion implantation with N does not routinely produce narrow linewidth centres, however the vacancy production from ion implantation could form narrow NV^- centres when they recombine with native nitrogen. However further work is required to form a statistically significant correlation.

2.3.3 Localised electron irradiation

Electron irradiation has also been developed for the purpose of producing NV^- within bulk diamond.[93] The motivation of developing localised electron irradiation over ion implantation is the improved coherence times of the fabricated NV^-, which is proposed to be due to the reduced cascade damage of the ion.[94] Cascade damage is caused by the implanted ion, and indeed high energy defects created by that ion, as it passes through the lattice.

Ohno *et al.* demonstrated that NV^- centres fabricated by electron irradiation can achieve coherence times of T_2 >600 μs and nanometre-precision depth control by using δ-doped nitrogen layers. Growing δ-doped layers is achieved using a chemical vapour deposition (CVD) reactor, where the nitrogen concentration can be controlled to create a 2 nm layer of high-N concentration diamond between two low-N concentration diamond layers.[95] However this method was later criticised by the authors for producing too few NV^- centres in the doped region for device integration.[91] Further work by McLellan *et al.* improved upon δ-doped localised electron implantation techniques to achieve lateral localisation of 450 nm, axial localisation of 4 nm whilst achieving long coherence times of T_2 >1 ms.[96] A limitation of their research is that NV^- centres are generated at the surface due to surface channelling of electrons.

In terms of yield, NV^- centres are produced in δ-doped diamond by electron irradiation at a 50% efficiency, which is an improvement over ion implantation but is still a detriment to scalability.[96] Scalability is also limited by the necessity for δ-doped layers, which further restrict the nanostructures that can be created. Finally it is important to note that NV^- centres fabricated in δ-doped layers

will have fundamentally limited T_2 coherence times due to high concentration of paramagnetic nitrogen atoms.[97]

2.4 Ultrafast laser fabrication in diamond

Laser based fabrication methods emerged in the 1960s as a powerful technique to provide significant anisotropic energy.[98] The radiation energy of the light sources could be coupled into the solid state through the use of spatially well-localised light-matter interactions, providing a novel means of advanced materials processing.[99] It has since been developed from a tool for cutting and welding into a powerful technique for the fabrication of photonic materials.[100] ultrafast laser writing has been developed since then, especially with the advent of pulsed lasers such as the Ti:sapphire, as a technique that can access an entirely new range of fabrication regimes.[101]

The process of ultrafast laser fabrication in diamond is partly motivated by diamond's optical transparency to the near infra-red spectrum, allowing light to pass through the diamond with little absorption losses.[102] The process of modification occurs by a multiphoton process that is highly non-linear, reducing fabrication to the focal spot. Lagomarsino *et al.* predicted that in order to achieve sufficient light-matter interaction to modify diamond the laser intensities must be of order $1-10$ TWcm^{-2}.[103] In order to achieve these intensities the fabrication laser must be focused using high NA optics and have a short pulse width ($\leq$400 fs).[104] The first reports of laser writing used to generate NV centres was in 2016 by Pimenov *et al.*[105] Within this article, picosecond laser irradiation lead to an increase in NV^- and NV^0 photoluminscence, however from the strain splitting of

the NV^- ZPL it was concluded that the modification included some microstructure changes. Such generation of strain or carbon phases would likely produce NV^- centres with poor coherence times.

Following this, Chen *et al.*[104] developed the technique in several ways. Firstly a femtosecond laser was used to produce more intense pulses and secondly the combination of a high numerical aperture (NA) objective lens and spatial light modulator was used to produce a small spot size. The uses of these objective lenses acts to reduce the fabrication volume such that the generation of single vacancies is dominant over ensemble generation around laser induced graphitisation. The necessity of high NA lenses can be understood when considering that to a first approximation the energy and intensity required to achieve fabrication is related by $E_{th} \propto I_{th}/NA^2$,[106] due to the axial profile of focused light. The use of a spatial light modulator is of particular importance and is discussed later. Chen's method of writing NV^- involved creating vacancies and annealing to produce the defects. Current methods indicate that NV^- centres cannot be directly written and there must be a post-vacancy generation processing step to produce NV^-. In 2019, Chen *et al.*[39] demonstrated that instead of an annealing step the post-processing can be replaced with a low energy pulse train. These post-processing methods, and how they affect the coherence properties of the NV^-, are discussed within this section.

2.4.1 Aberration correction

The ultrafast laser fabrication method is highly dependant on the ability to generate a small focal spot with the writing laser. One property that acts against this goal is diamond's high refractive index of $n = 2.4$.[107] The large refractive index change between an immersion oil lens and the diamond is significant and therefore produces

significant spherical aberration,[108, 109] which is exacerbated by increasing the focusing depth[110] and by using high NA lenses.[111]. Attempts at fabrication have demonstrated that surface relief structures[112] and graphitic wires within the bulk[113] can be made without correcting for this aberration. However, the fabrication of well localised features within the bulk of diamond has been limited by this refractive index mismatch.[108, 109] The ability to fabricate NV^- centres flexibly within the bulk of diamond facilitates implementations of the defect within situations where surface effects are undesirable and allows for the possibility the defect to couple to certain photonic structures, such as Solid Immersion Lenses (SILs).

The spherical aberration problem generated by refractive index mismatch is not a problem exclusive to diamond and there are several methods of correction. One solution used in literature involves the optimisation of a correction collar available on modern high NA objective lenses. However this technique is not ideal since there is no quantitative function that can be optimised during adjustment and the adjustment itself causes some focal shift.[114] Additionally, there forms of correction that typically only provide partial spherical aberration correction. Alternatively, a technique presented by Escobar *et al.* demonstrates a simple spherical correction by using purely absorbing beam-shaping elements.[110] However, an effective way of reducing aberrations has been shown to be through adaptive optic elements such as a Spatial Light Modulator (SLM) or Deformable Mirror (DM).

Implementation of adaptive optics into ultrafast laser writing in diamond has been performed by Simmonds *et al.* who used a dual set-up involving both an SLM and DM.[115] In order to assess the impact of aberration correction, they studied the fabrication behaviour in three cases. Firstly, with both the SLM and the DM set to a flat phase profile, which should provide no aberration correction.

Secondly, with the SLM providing feedback correction whilst the DM remained flat. Finally both the SLM and DM where active in correction in a scheme in which the DM provided correction for the predicted depth dependent aberration whilst the SLM provided fine correction.

Simmonds *et al.* found that without the adaptive elements there was insufficient confinement along the optical axis for well localised fabrication and when the adaptive elements were used the system was capable of fabricating micron scale graphitic structures at depths greater than 200 μm.[115] Fabrication efficiency was increased by using both the SLM and the DM. The publication reports that calibration issues limited the DM predicted depth correction to 80 μm, therefore at greater depths the correction was set for 50 μm whilst the SLM compensated for the remaining aberration. It is important to note that the diamond was modified to produce graphite rather than vacancies, however the principles of fabrication efficiency remain the same.[104] Unaddressed by Simmonds *et al.* is the temporal distortion of an ultrashort pulse when corrected by a two-dimensional reflective element such as a deformable mirror, which can be corrected through temporal pulse shaping.[116]

2.4.2 Post processing techniques

In order to create a vacancy based defect, the vacancy must be able to migrate and aggregate with a nitrogen atom. Vacancies first become mobile at 400 °C[117] and upon annealing diamond at 600 °C, photoluminescence studies suggest that single vacancies aggregate into divacancy centres, which can be destroyed by annealing at higher temperatures.[118] In nitrogen-containing diamond the formation of divacancy centres is suppressed by the formation of NV centres. Two other defects that can

effect the formation of vacancy based defects are higher order nitrogen based defects; two adjacent substitutional nitrogen atoms (N-N) and four adjacent substitutional nitrogen atoms surrounding a vacancy (4N-V). Commonly referred to as the A centre and B centre respectively and both schematically drawn in fig. 2.3.

These centres act to trap migrating vacancies[119] but do not result in the formation of an NV defect. Further annealing results in the generation of a photoluminescence feature at 503 nm, which has been associated with the (N-V-N)^0 defect centre.[118] This centre is considered to be the results of an A centre capturing a single vacancy. Vacancies trapped by the B centre results in the 496 nm photoluminescence feature, which indicates the generation of a (4N-2V) centre.[118] Both the (N-V-N)^0 and (4N-2V) centres are stable up to high temperatures[118] which makes diamonds containing A and B centres undesirable for the fabrication of NV$^-$ centres.

Chen *et al.* investigated the effect of different annealing recipes of laser written vacancies in diamond.[104] For samples annealed at 900 °C for 3 hours it was observed that few NV$^-$centres were generated after the anneal and that mostly vacancies and extended damage remained. This observation is consistent with annealing studies conducted by Davies *et al.* which found that extended vacancy structures are destroyed by annealing above 1000 °C.[118] The annealling studies by Chen *et al.* found that annealing at 1000 °C for 3 hours produced significantly more NV$^-$ centres and that annealing for 1200 °C for 24 hours resulted in the dissociation of many of those NV$^-$centres.[104] By comparing the annealing process with the Arrhenius equation, Chen *et al.* derived the activation energy of vacancy diffusion to be 2.0 eV, which is consistent with other reports.[79, 120, 121]

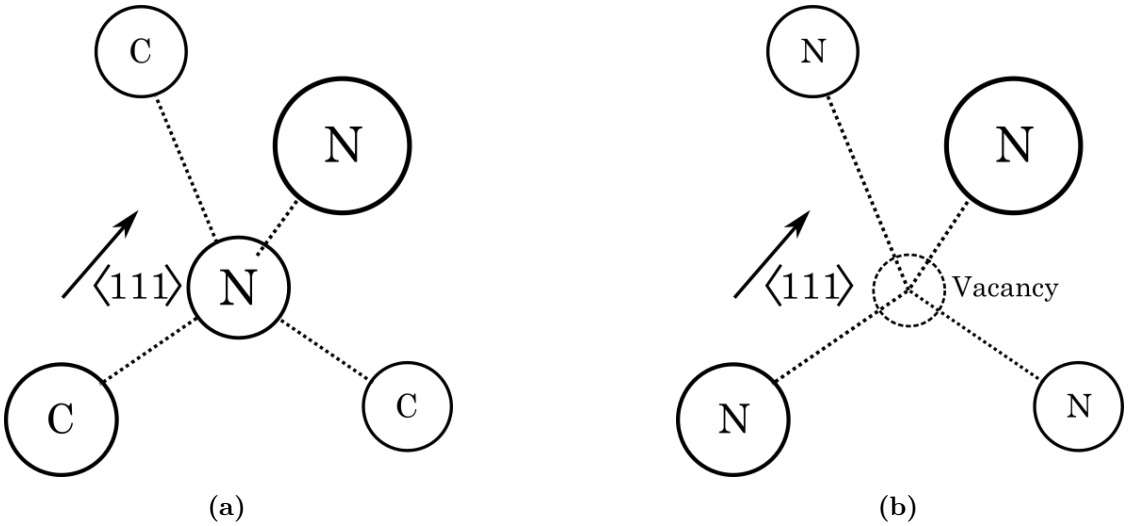

Figure 2.3: Schematic diagrams of (a) two adjacent substitutional nitrogen atoms, commonly referred to as the A-centre and (b) four adjacent nitrogen atoms surrounding a vacancy, commonly referred to as the B-centre.

The precision of fabrication has been determined by fabricating NV^- centres in a regular array and then using confocal fluorescence microscopy to compare the final positions of the centres to the actual array points. A comprehensive study of laser written NV^- centres by Stephen *et al.* calculated the fabrication precision to be $\pm$200 nm laterally and $\pm$250 nm axially,[122] which is comparable to the average nitrogen seperation in 1 ppb nitrogen containing diamond (178 nm). This lateral precision is an improvement over that previously discussed for electron irradiation and comparable to that found for ion implantation. A comparison in axial precision is somewhat inappropriate since both ion implantation and electron irradiation achieve these high precisions through the use of $\delta-$doped regions, instead of being an inherent product of the technique. The high axial precision is a product of the non-linearity of the fabrication procedure and is therefore not necessarily limited by the diffraction limited spot size.[122] It is theorised that the precision of fabrication is limited by the nitrogen concentration of the diamond used.[122]

Recent work by Chen *et al.* has demonstrated that NV^- centres can be generated

without a conventional thermal annealing scheme by instead following the initial vacancy generating pulse with a low energy pulse train.[39] The generation of NV^- was monitored using a confocal fluorescence feedback system, where the photon count rate demonstrated an intermittent signal eventually resulting in the stabilisation of NV^- fluorescence.[39] This intermittent signal is hypothesised to be the product of strain field interactions between the substitutional nitrogen, vacancy and an interstitial carbon, which prevents the stable formation of the NV^- orbital system until the interstitial dissociates. This proposed model is explored and challenged further in Chapter 6.

An important product of this technique is that NV^- defects can be created with near unity yield, which is a significant improvement over thermal annealling methods wherein the single defect yield was limited by Poissonian statistics to 37%.[39] This yield, on a fabrication site basis, is an improvement over ion implantation, even with dynamic annealing during co-implantation.[89]

Local laser annealing does, however, appear to effect the coherence properties of the fabricated NV^-. Stephens *et al.* demonstrated that, if a global thermal anneal is used, laser written NV^- centres have a coherence time of T_2 >500μs, which was fundamentally limited by the natural abundance of ^{13}C in the diamond.[122] Using a local laser anneal, these coherence times are reduced to T_2 <170 μs, potentially due to the presence nearby defects. However, due to the nature of the sample used, it is currently unkown if these defects are instrinsic to the sample or a product of laser fabrication.[39]

A strong incentive for this explanation can be found in the fabrication precision, which is ±20 nm laterally and ±50 nm axially, an which improves upon the

fabrication accuracy of globally annealed NV^- centres by a factor of 3.6.[39] It is important to note that this work was completed in a sample containing 1.8 ppm of substitutional nitrogen as opposed to the ppb concentrations usually used. The average distance between substitutional nitrogen in 1.8 ppm nitrogen containing diamond ($\langle r \rangle \sim 1/\sqrt[3]{n} = 21.7$ nm) is consitent with the fabrication precisions recorded. Finally, this post-processing technique appears to produce an 88% preferential orientation of NV^- centres in the plane perpendicular to the optical axis, although the authors recognise the statistical insignificance with respect to the same size ($N = 26$). This does, however, demonstrate the potential for the use of polarisation optics in the fluorescence feedback to produce aligned NV^- centres.

2.5 Summary

Ultrafast laser writing has been demonstrated to be a powerful tool in the fabrication of NV^- centres in diamond, which have promising applications in magnetometry and quantum computing. As discussed, diamond is host to two promising vacancy based single photon emitters, the NV^- and SiV^- centres. In particular the NV^- and SiV^- centres do have opposing trade-offs in terms of performance, with the NV^- centre demonstrating long room temperature coherence times but poor optical emission and the SiV^- centre demonstrating the opposite. Whilst ultrafast laser writing has been explored for the NV^- centre, there have been no published attempts of laser writing SiV defects in diamond. The most prevalent reason for this has already been discussed, but not addressed explicitly. The SiV is the most stable silicon based defect since the large silicon atom is accommodated by presence of two vacancies. The deterministic fabrication of this defect would most likely

require substitutional silicon defects as a prerequisite. Which is challenging due to the defects apparent rarity.[123]

However, as mentioned in this review's introduction, these are only two of the many single photon sources present in diamond. There is a host of transition metal and group-IV defects that have been identified and not explored within this review. Reasons for the exclusion of these defects range from their incompatibility with ultrafast laser writing, a technique capable of writing only vacancy based defects, to their lack of application based development. However there are some clear candidates amongst these, such as the nickel-nitrogen complex NE4,[124] which could possibly be fabricated by ultrafast laser writing. It is important to note that there is still development of new defects that show promise in terms of single photon sources and spin control,[125] it is therefore important to continue to survey literature for new developments in the diamond defect family.

Ultrafast laser writing provides well localised, coherent NV^- centres within the bulk of diamond without sacrificing scalability by using masks or $\delta-$doping. A common restriction of the other techniques explored within this review is that they involve steps that sacrifice scalability and device integration for better performing NV^- centres. Laser fabrication has additionally been shown through the use of "stick-on" SIL lenses instead of an SLM in order to maintain a high NA.[126] However, this technique does reduce fabrication flexibility and might potentially run into similar issues when fabricating within structures.

Scalability is also improved by using a local laser annealling, which produces NV^- centres with a near-unity yield, the highest reported for NV^- fabrication by a large margin. The laser post processing technique also improves upon the precision

of fabrication, but demonstrates poorer coherence times than electron irradiation and globally annealed NV^- centres. Future work can be focussed on refining the laser processing so that the isotopically limited coherence times can be achieved. Theoretically this would involve developing a post processing scheme that would allow any nearby interstitials to diffuse sufficiently from the fabricated NV^-.

Local laser annealing has only been used to fabricate NV^- centres, however the scope of the technique is not necessarily limited to this defect. The ability to selectively migrate defects provides a powerful tool for not only creating colour centres but also for dissociating them. In a broader scope, it would be useful to investigate how this technique can be used to modify other defects in diamond. This review also demonstrates how aberration correction has been used to significantly enhance optical techniques, especially with respect to diamond. The advantage that adaptive optics provides during laser fabrication acts as a strong motivater to extend its application in the characterisation of defects, which may improve the materials capabilities in quantum computing, magnetometry and sensing.

Chapter 3

Theoretical background

3.1 Introduction

This chapter aims to outline the relevant theory that underpins the research throughout this thesis. The chapter will begin with a discussion of the ultrafast laser writing process, with a focus on the two main regimes involved in achieving optical breakdown. These processes can be approximately linked through the Keldysh parameter, which contains key insight into which experimental parameters need to be controlled in order to optimise breakdown. Due to the importance of adaptive optics within the research presented, this chapter will then layout key optical theory in order to understand the aberration corrections applied.

Finally this chapter will outline the fundamental theory of Density Functional Theory (DFT), which is a Schrödinger equation solving technique used throughout 6. The theory presented here is not exhaustive, the chapter simply aims to outline the key underlying principles of how DFT calculates a system properties and then discusses the theory behind more practical elements of the implementation of DFT such as plane waves and pseudopotentials.

3.2 Mechanism of laser-induced damage

Using high power lasers to modify materials has been widely implemented throughout the late 20^{th} century to cut or mill metals. However recently this technique has been developed to create much more subtle modifications to a wider range of materials. The process of this laser induced modification within transparent dielectric materials allows for engineering of the materials local refractive index or to create macroscopic damage within the material.[127, 128] Laser machining generally relies on the optical excitation of free carriers which relax into the lattice to create damage. However in transparent materials such as diamond there is no linear absorption of near infrared to visible photons due to the materials large band gap. Instead non-linear effects are proposed to be responsible for the generation of free carriers.

In many light-matter interactions the intensity of the light is small enough to be considered as a weak field perturbation of a system. However, ultrafast laser pulses fall into the regime of strong field interactions, wherein the laser field intensity is much larger than atomic binding energies. With strong enough field intensities, laser excitation can be used to drive a large population of electrons into an excited state, which can relax and generate damage within the material.

As discussed, for transparent dielectric materials there is no linear absorption of laser light and therefore optical breakdown much be achieved through non-linear light-matter interactions. The key non-linear interactions which lead to optical breakdown in transparent dielectric materials are tunnelling ionisation, multiphoton ionisation and various scattering processes that occur in the excited state.[129, 130]

3.2.1 Tunnelling and Multiphoton Ionisation

Tunnelling and multiphoton ionisation are distinct from avalanche ionisation since they do not require the presence of free carriers. Additionally, both these processes can occur simultaneously but the dominance of any mechanism can be described by the Keldysh parameter:[131]

$$\gamma = \sqrt{\frac{I_p}{2U_p}} \tag{3.1}$$

where I_p is the ionisation energy of an electron and U_p is the average kinetic energy transferred from the laser field to an electron, or the pondermotive energy:

$$U_p = \frac{1}{2} m\omega^2 \langle x^2 \rangle \tag{3.2}$$

where ω is the laser frequency and the position of an electron, x, is given by $x = -\frac{q}{m\omega^2}\sqrt{\frac{2I}{nc\epsilon_0}} cos(\omega t)$. This results in the full expression for the Keldysh parameter:

$$\gamma = \frac{\omega}{q}\sqrt{\frac{mnc\epsilon_0 I_p}{I}} \tag{3.3}$$

where I is the laser intensity at the focus, m and q are the reduced mass and charge of the electron, c is the velocity of light, n is the refractive index of the material and ϵ_0 is the permitivity of free space. The Keldysh parameter describes a

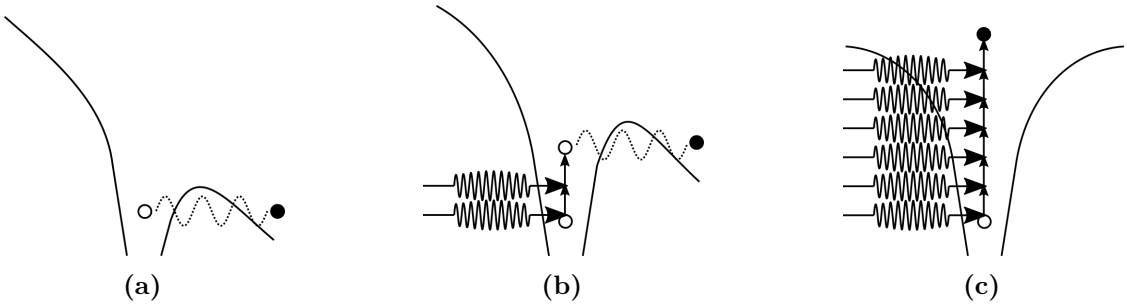

Figure 3.1: Schematic diagram of an electron escaping a potential well via (a) tunnelling, which occurs when the Keldysh parameter $\gamma << 1$. (b) a combination of tunnelling and multiphoton ionisation and (c) multiphoton ionisation when $\gamma > 1$.

comparison between the time required for tunnelling and the period of the laser field. In a regime where $\gamma << 1$, tunnelling ionisation dominates and where $\gamma > 1$, multiphoton ionisation dominates.

These two methods of ionisation are the result of different physical phenomena at the focal spot. Tunnelling ionisation occurs when the Coulomb potential that localises an electron is modified by an external laser field. As shown in figure 3.1(a), the barrier potential is reduced such that, given enough time, the electron is able to tunnel out of this potential well and into the excited state. Multiphoton ionisation requires the simultaneous excitation of an electron by more than one photon, with the sum energy of each photon being sufficient to ionise an electron into the conduction band. The probability of a n-photon ionisation event, P_n, is given by:

$$P_n = \sigma_n I^n \tag{3.4}$$

where σ_n is the multiphoton absorption coefficient for the absorption of n photons.[132] Finally, it is important to mention that defect states close to the conduction or valance band would result in a decreased non-linearity in multiphoton ionisation. However, for commercially available high purity diamond, such as those used within this thesis, the predominant defect is the substitutional nitrogen, which is a deep doner at $E_{CB} - 1.7$ eV.[133, 134]

3.2.2 Excited carrier dynamics

Whilst in the conduction band, electrons, and holes left behind in the valence band, are able to linearly absorb additional photons to gain energy. In this state many scattering events can occur between carriers and between carriers and phonons. Both energy and momentum can be transfered by the carriers through electron and phonon

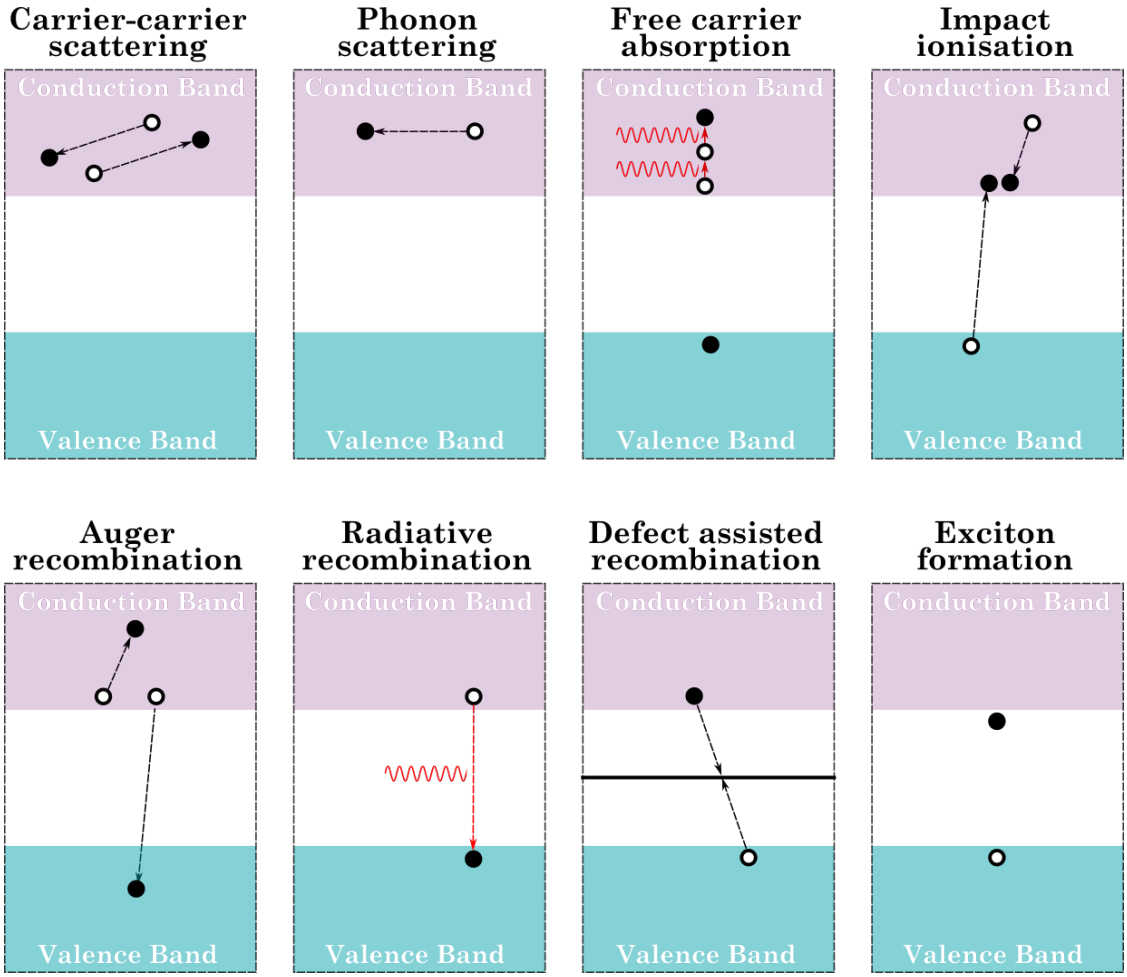

Figure 3.2: Schematic diagrams of the various scattering and recombination processes that can occur in excited carriers under an ultrafast laser pulse.

scattering respectively. Additionally, excess energy can be transfered to valence electrons through avalanche ionisation and a reverse process can occur through Auger recombination. Theses processes are offset by recombination processes. The group action of these mechanisms lead to the formation of a local free carrier plasma within the material which is able to relax and deposit its energy into the lattice creating damage.[135] The processes discussed are schematically shown in fig. 3.2.

3.3 Aberration Correction

As discussed, a key component to this process is the non-linear nature of the light-matter interactions used to modify the lattice. This forces the use of high numerical aperture (NA) optics to create a small, and therefore intense, focal spot within the diamond. This can be understood by calculating the lateral and axial size of a focal spot due to diffraction:[12]

$$\Delta\rho_{FWHM} = 0.51\frac{\lambda}{NA} \tag{3.5}$$

and

$$\Delta z_{FWHM} = \frac{0.9\lambda}{n - \sqrt{n^2 - NA^2}} \tag{3.6}$$

where $\Delta\rho_{FWHM}$ and Δz_{FWHM} is the lateral and axial FWHM of the focal spot respectively. λ is the wavelength of light and NA is the numerical aperture, defined as $NA = nsin(\alpha)$, where α is the semi-aperture angle of the focujsing lens. This equation for the axial focal spot size might be unfamiliar to readers that are used to the low NA approximation of Δz_{FWHM}, within this thesis only high NA optics are used. The derivation of this form of the axial FWHM does not use the small angle approximation and therefore is much better at describing high NA focal spots. However, the use of high-NA optics increases the effect of aberrations on the focal spot shape, leading to a non-ideal focal spot even within oil immersion lenses.[111] However, by using some adaptive optical element capable of introducing controllable, opposite sign, aberrations into an optical system, the original diffraction limited focal spot can be regained.

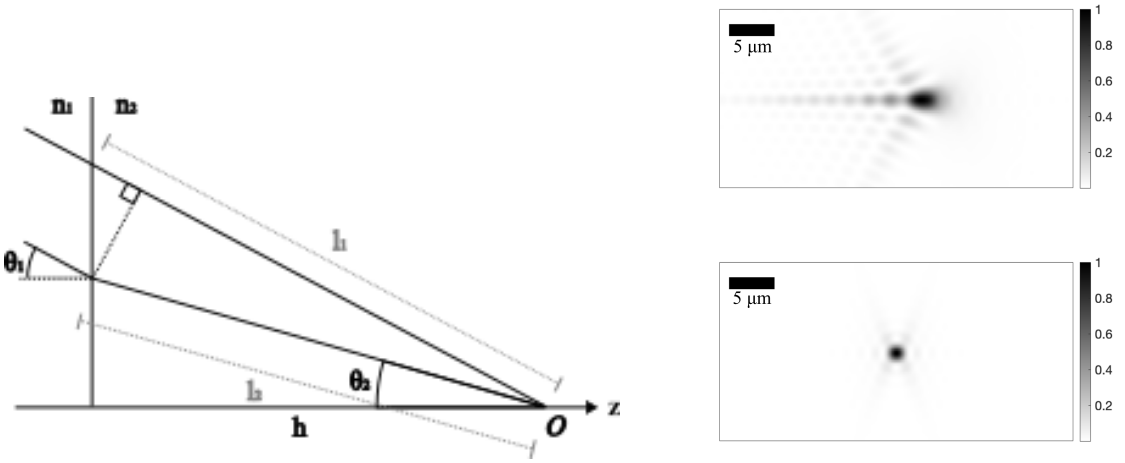

(a) **(b)**

Figure 3.3: (a) Geometric illustration of the refractive index mismatch (RIM) when focusing through a stratified medium with a single interface. Ray 1 depects no pertubation along its path to the focus O, as if it is travelling solely through a homogenous medium of n_1. Ray 2 demonstrates a pertubation due to refraction at the refractive index change. Illustrated case demonstrates $n_1 < n_2$. (b) Calculated phase amplitude of the uncorrected (top) and spherically corrected (bottom) focal spots of 790 nm light focused 10 μm into diamond (n_2 =2.4) using a 1.4NA oil objective (n_1 =1.51). Depth is represented along the horizontal axis.

3.3.1 Spherical aberration

The primary source of aberrations come from the refractive index interface between the objectives immersion medium and the sample. As a note, throughout this thesis a high-NA (NA = 1.4) oil objective was used during fabrication therefore this step change is between the immersion oil ($n_1 = 1.52$) and the diamond ($n_2 = 2.42$). This refractive index interface leads to the generation of spherical aberration. Fig. 3.3a illustrates the phase change due to the refractive index mismatch (RIM) caused by focusing through a stratified media with a single interface. By calculating the relative path lengths of the unperturbed (l_1) and perturbed (l_2) paths it is possible to construct the aberration function $\Psi_{RIM}(d, \rho)$ as:[136]

$$\Psi_{RIM}(d, \rho) = k(n_2 l_2 - n_1 l_1) \tag{3.7}$$

where ρ is the normalised radial coordinate of the pupil, $k = 2\pi/\lambda$ and d is the focusing depth. The geometry in Fig. 3.3a gives:

$$\Psi_{RIM}(d, \rho) = kd(n_2 \cos(\theta_2) - n_1 \cos(\theta_1)) \tag{3.8}$$

By assuming the Abbe sine law and introducing the normalised radius as $\rho = sin(\theta_1)/sin(\alpha)$, the aberration function is determined to be:

$$\Psi_{RIM}(d, \rho) = dkNA(\sqrt{\csc^2(\beta) - \rho^2} - \sqrt{\csc^2(\alpha) - \rho^2}) \tag{3.9}$$

where α is the maximum angle as determined by the NA and $n_1 sin(\alpha) = n_2 sin(\beta)$.

From equation 3.9 the spherical aberration caused by focusing through a planar refractive index interface can be determined analytically. The only necessary inputs required are the NA, refractive indexes n_1 and n_2, the focusing depth and the wavelength of light.

It is important to note that a full removal of spherical aberrations would remove the focusing effects of refraction at the refractive index change, which is not always desired. An expression for the spherical aberration responsible only for focus distortion has been presented by Jesacher *et al.*[109] Fig. 3.3b compares the effects of spherical aberration on 790 nm light focused 10 μm into diamond (n_2 =2.4) using a 1.4NA oil objective (n_1 =1.51) with an unaberrated focal spot focused at the same depth. Here the normalised phase-only intensity has been calculated from the magnitude of the Fourier transform for the phase component of the pupil function. Even at this moderate focus depth, the effects on the pupil are large.

3.3.2 Remote focusing

Adaptive optical elements can be useful for techniques other than just aberration correction. Of particular use is the ability to introduce tip, tilt or defocus phase

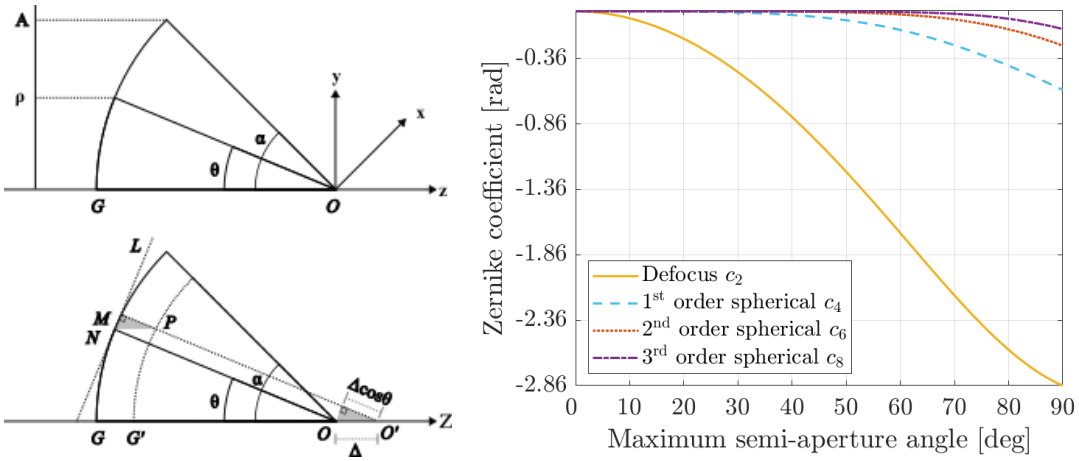

(a) **(b)**

Figure 3.4: Representation of defocus using a high-NA objective lens. (a) Top, a frame of reference for the Debye-Wolf diffraction integral and bottom the geometrical derivation of the defocus for a focal displacement Δ. (b) The dependence of the first four Zernike coeffecients (excl. Zernike piston) as a function of α for a 1 μm focal shift in a homogenous medium of refractive index $n = 1.51$ at a wavelength of $\lambda = 790$nm.

to control the position of the focal spot in all dimensions within the material. Particularly within this work, the technique of remotely focusing or defocusing the focal spot through the use of an adaptive element is used heavily to overlap multiple focal spots using the same objective lens. The field at the focus of a high-NA lens can be accurately modelled by the Debye-Wolf diffraction integral,[137] which is geometrically illustrated in fig. 3.4a(a).

From this geometry the phase representation of the high-NA defocus, $\Psi_{RF}(\rho)$, can be derived from the dependency of the diffraction integral upon the axial coordinate, z. Assuming an axial focal displacement of Δ that causes the Gaussian focus to shift from O to O', as shown by 3.4a. The corresponding phase change can then be derived as:

$$\Psi_{RF}(\rho) = k\Delta cos(\theta) \tag{3.10}$$

i	Zernike polynomial, $Z_i(\rho, \theta)$	Aberration name
1	1	Piston
2	$2\rho cos(\theta)$	Tip
3	$2\rho sin(\theta)$	Tilt
4	$\sqrt{3}(2\rho^2 - 1)$	Defocus
5	$2\sqrt{3}\rho^2 cos(2\theta)$	Astigmatism
6	$2\sqrt{3}\rho^2 sin(2\theta)$	Astigmatism
7	$2\sqrt{2}(3\rho^3 - 2\rho)cos(\theta)$	Coma
8	$2\sqrt{2}(3\rho^3 - 2\rho)sin(\theta)$	Coma
9	$2\sqrt{2}\rho^3 cos(3\theta)$	Trefoil
10	$2\sqrt{2}\rho^3 sin(3\theta)$	Trefoil
11	$\sqrt{5}(6\rho^4 - 6\rho^2 + 1)$	First Spherical

Table 3.1: The first 11 Zernike polynomials using the Noll indexing scheme.[138]

which can be represented with respect to ρ:

$$\Psi_{RF}(\rho) = k\Delta\sqrt{1 - \rho^2 sin^2(\alpha)} \tag{3.11}$$

This formalism allows for the independent axial shift of a focal spot using an adaptive element. As in what was previously established for spherical aberration this function only depends on the NA and wavelength of light, and arbitrary Δ can be selected to shift the focal spot the desired amount.

3.3.3 Zernike Polynomials

Aberrations other than those considered previously can be caused by slight system misalignment or a tilted sample surface. For convenience, these aberrations can be expressed through Zernike polynomials. Zernike polynomials are a set of functions that are orthogonal over the pupil. The Zernike polynomials were originally derived by Zernike[139] and given a more detailed analysis by Born & Wolf,[140] however the definition used within this thesis are of the polynomials described by Noll[138] and later by Mahajan[141]. Table 3.1 shows the first 11 Zernike modes and the terms used to commonly describe these modes as aberrations where appropriate.

It is important to note that the Zernike polynomials do have representations for defocus and spherical aberration. However, these functions are an approximation and do not sufficiently describe aberrations at high NA. This is demonstrated in fig. 3.4b, within the focal spot in a homogenous medium of refractive index $n = 1.51$ is shifted by 1 μm. It can be seen that as the NA starts to exceed 1, higher order Zernike modes are required in order to produce the same shift.[142]

3.4 NV centre

3.4.1 Energy level structure

The NV centre in diamond comprises a substitutional nitrogen atom and an adjacent lattice vacancy, as shown in figure 3.5(b). Due to the diamond crystal structure these centres are $\langle 111 \rangle$ orientated, giving the centre four possible orientations. The electronic structure of the NV^- centre is formed of 6 unpaired electrons; two from the substitutional nitrogen, three from the three carbon atoms adjacent to the vacancy and a final trapped electron. This leads to the generation of four additional states in the diamond band structure labelled as a_1, a_2, e_1 and e_2.[33]

The a_1 state exists within the valence band and is therefore of little importance to the electronic properties of the NV centre. The a_2 state exists 1.4 eV from the valence band and the e_1 and e_2 states, commonly referred together as the e-manifold, exists at 3.2 eV above the valence band.[33] The location of the orbitals of these states are shown in figure 3.5. Due to Hund's rule, the six electrons fill the four bands in a $a_1^2 a_2^2 e_1^1 e_2^1$ ground state configuration.[33] Exciting this ground state, typically with 532 nm light, results in a $a_1^2 a_2^1 e_1^2 e_2^1$ excited state. Relaxation from this excited state results in a 637 nm optical emission as the electron transitions

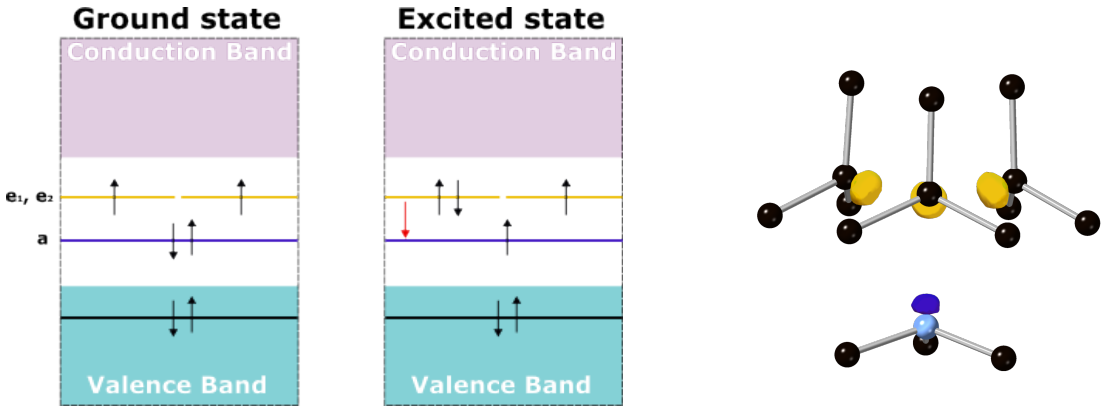

Figure 3.5: (a) The band structure of the NV centre in diamond, the red arrow depicts the $a_1^2 a_2^2 e_1^1 e_2^1 \rightarrow a_1^2 a_2^1 e_1^2 e_2^1$ transition which results in 637 nm fluorescence. (b) A diagram of the NV centre with the orbitals colour coded with (a).

between the e-manifold and the a_2 state which corresponds to the group transition of $a_1^2 a_2^1 e_1^2 e_2^1 \rightarrow a_1^2 a_2^2 e_1^1 e_2^1$.[33] This transition is shown diagrammatically in figure 3.5a. This electronic transition is however heavily coupled to lattice vibrations resulting in only 4% of the light emitted by the NV centre being part of its zero-phonon line (ZPL) and the rest is emmited into the phonon sideband that exists between 637 - 800 nm.[3]

3.4.2 Photon emission statistics

The NV centre is a single photon emitter with a three level system as shown in fig. 3.6. A single photon emission can be determined through the photon autocorrelation function which can be measured using a Hanbury-Brown-Twiss (HBT) interferometer.[143] The principle of a HBT measurement is that if the emission from a single photon emitter is passed through a 50:50 beam splitter then there should be no simultaneous detection of photons at either exit of the beamsplitter. A schematic diagram of a HBT interferometer is shown in a later chapter in fig. 4.3. By correlating detection events at these two detectors the photon

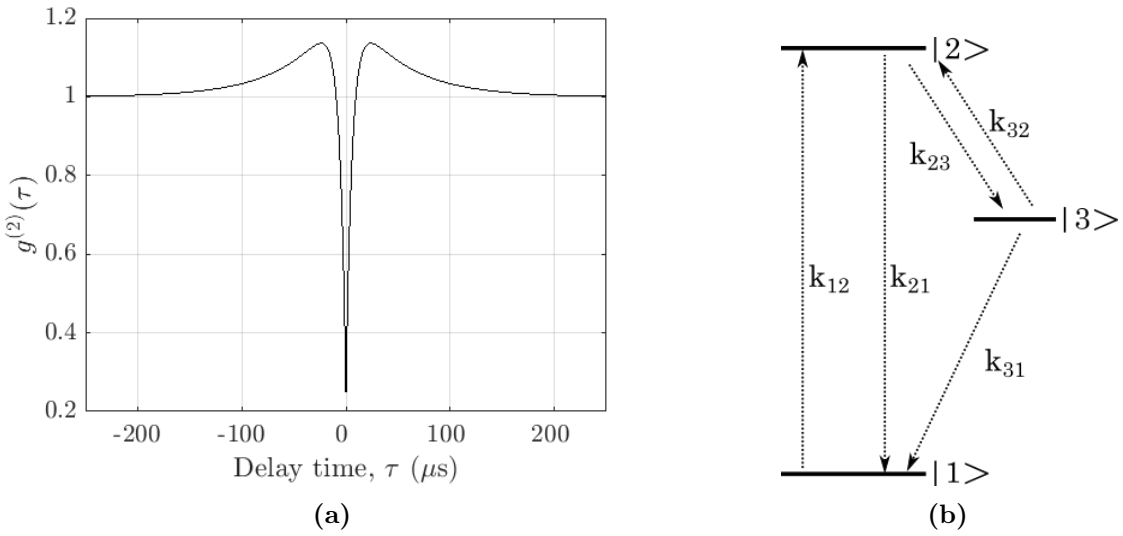

Figure 3.6: (a) Simulated second order correlation function, $g^{(2)}(\tau)$, of a three level system of a single photon emitter demonstrating photon anti-bunching at $\tau = 0$ and photon bunching at $\tau < 100\mu s$. (b) A schematic of a three level system which can be used to describe a single NV^- centre. Here the k_{21} transition results in the 637 nm fluorescence from the NV^- centre.

autocorrelation function can be constructed as a function of the delay time, τ. This correlation function for a HBT interferometer can be described as:[143]

$$g^{(2)}(\tau) = \frac{\langle I(t)I(t+\tau)\rangle}{\langle I(t)\rangle\langle I(t+\tau)\rangle} \tag{3.12}$$

where $I(t)$ is the intensity at time t and $\langle I(t)\rangle$ denotes the time average of $I(t)$. This histogram is shown diagrammatically in fig. 3.6a. For a single photon emitter $g^{(2)}(\tau) \to 0$ as $\tau \to 0$, this is called the anti-bunching dip. More generally for an N single photon emitters of equal brightness:

$$g^{(2)}(\tau \to 0) \to \frac{\langle N(N-1)\rangle}{\langle N\rangle^2} \tag{3.13}$$

Additionally, the shape of the histogram shown in fig. 3.6a demonstrates a rise in the $g^{(2)}(\tau)$ before $g^{(2)}(\tau \to 0)$, this is known as photon bunching. This is a result of NV^- centre being a three-level system where levels $i = 1, 2, 3$ refer to the ground state, excited state and phonon side band respectively. The existance of a third

state introduces a second decay pathway for electrons leading to the convolution of two decay patterns and therefore this photon bunching behaviour. The population dynamics of this system is described by the rate equations:[144]

$$\begin{bmatrix} \dot{L}_1 \\ \dot{L}_2 \\ \dot{L}_3 \end{bmatrix} = \begin{bmatrix} -k_{12} & k_{21} & 0 \\ k_{12} & -k_{21} - k_{23} & k_{23} \\ 0 & k_{23} & -k_{32} \end{bmatrix} \cdot \begin{bmatrix} L_1 \\ L_2 \\ L_3 \end{bmatrix} \tag{3.14}$$

where $\dot{L}_i$ is the first order time derivative of electron population level L_i and k_{ij} is the transition rate from level i to level j. From this an analytical expression for the second order correlation function can be obtained by solving the rate equation:[144]

$$g^{(2)}(\tau) = 1 + c_2 e^{-\frac{\tau}{\tau_2}} + c_3 e^{-\frac{\tau}{\tau_3}} \tag{3.15}$$

where the decay times τ_i and coefficients c_i are given by:

$$\tau_{2/3} = \frac{2}{A \pm \sqrt{A^2 - AB}} \tag{3.16}$$

$$c_2 = \frac{1 - \tau_2 k_{32}}{k_{32}(\tau_2 - \tau_3)} = -(1 + c_3) \tag{3.17}$$

$$A = k_{12} + k_{21} + k_{32} + k_{23} \tag{3.18}$$

$$B = k_{12}k_{23} + k_{12}k_{32} + k_{21}k_{32} \tag{3.19}$$

where the c_3 term is the origin of the photon bunching. This phenomenon is discussed further in chapter 4.

3.5 Density Functional Theory

Density functional theory (DFT) is a method of solving the many-body Schrödinger equation by expressing its components as functionals of electron density. These components hence become functions of density, which is itself a function over space, hence the use of the term functional. This is in order to reduce the computational

expense required in solving the Schrödinger equation for many body systems. The many-body Hamiltonian can be expressed as:

$$H = -\frac{1}{2}\sum_{i=1}^{N}\nabla_i^2 - \frac{1}{2}\sum_{a=1}^{M}\frac{1}{M_a}\nabla_a^2 - \frac{1}{2}\sum_{i=1}^{N}\sum_{a=1}^{M}\frac{Z_a}{r_{ia}} + \sum_{i=1}^{N}\sum_{j>i}^{N}\frac{1}{r_{ij}} + \sum_{a=1}^{M}\sum_{b=1}^{M}\frac{Z_a Z_b}{r_{ab}} \quad (3.20)$$

where i, j are an index for the systems N electrons and a, b are an index for the systems M nuclei.[145] This equations includes terms decsrribing electron and nuclear kinetic energy, electron-nuclear interactions, electron-electron interactions and finally nuclear-nuclear interactions.

The Born-Oppenheimer approximation is typically used to reduce the complexity of this model. This approximation assers that, due to the large mass difference between electrons and atomic nuclei, the nuclei can be considered stationary compared to the electrons

The terms within this equation, from left to right, are the electron kinetic energy, the nuclear kinetic energy, the electron-nuclear interaction energy, electron-electron interaction energy and nuclear-nuclear interaction energy. [146] This allows for the Hamiltonian to be reduced to:

$$\begin{aligned} H &= -\frac{1}{2}\sum_{i=1}^{N}\nabla_i^2 - \sum_{i=1}^{N}\sum_{a=1}^{M}\frac{Z_a}{r_{ia}} + \sum_{i=1}^{N}\sum_{j>i}^{N}\frac{1}{r_{ij}} \\ &= \hat{T} + \hat{V}_{ne} + \hat{V}_{ee} \end{aligned} \quad (3.21)$$

Whilst the computational difficulty of solving this version of the Hamiltonian is reduced, it is not yet feasible to compute. One important principle to note is that for a Hamiltonian that described the ground state of a system, any given trail wavefunction $|\tilde{\phi}\rangle$, will invariably overestimate the ground state energy of that system. This leads to a useful computation tool for searching for an accurate ground state wavefunction, known as the variational principle:[147]

$$E_0 \leq \tilde{E}_0 = \frac{\langle\tilde{\phi}|\, H\, |\tilde{\phi}\rangle}{\langle\tilde{\phi}|\tilde{\phi}\rangle} \quad (3.22)$$

This principle is used in DFT in order to solve for a systems ground state.

The formal definitions that structure DFT is laid out in the Hohenberg-Kohn theorems. These theorems are not presented in detail within this thesis, further reading on these can be found in references [145] and [147]. Following from these theorems there remains one problem which prevents the application of DFT. That is that a precise functional form for kinetic energy within an interacting system does not exist. This issue was circumvented by the Kohn-Sham equations, which rewrite the Hamiltonian such that it describes a non-interacting system with a modified effective potential that contains all interactions.

Whilst, there is an exact form for the non-interacting kinetic energy, there is not an exact form for this modified potential, $V_s(\boldsymbol{r}_i)$. Which can be decomposed into three parts:

$$V_s(\boldsymbol{r}_i) = V_J(\boldsymbol{r}_i) + V_{ext}(\boldsymbol{r}_i) + V_{xc}(\boldsymbol{r}) \tag{3.23}$$

where $= V_J(\boldsymbol{r}_i)$ is the exact functional form for the Coulomb potential and $V_{ext}(\boldsymbol{r}_i)$ is the exact functional form for the nucleus-electron interactions. However V_{xc} is the functional governing exchange and correlation interactions, which is not yet defined and must be approximated.

3.5.1 Exchange correlational functionals

Functionals for electron exchange and correlation are yet to be defined within DFT and must be approximated. The simplest of these approximations are local density approximations (LDA). These treat the exchange-correlation energies of each infinitesimal density element as equivalent to that of a uniform electron gas:

$$E_{xc}^{LDA}[\rho] = \int \rho(\boldsymbol{r})\epsilon(\rho(\boldsymbol{r}))d\boldsymbol{r} \tag{3.24}$$

where $\epsilon(\rho(\boldsymbol{r}))$ is the exchange-correlation energy density of a uniform electron gas.[147] One effect of using LDAs they typically overestimate bond energies by as much as 36 kcal mol^{-1} and therefore typically over-bind systems.[145, 148] This can be seen at long ranges, where LDA forces an exponential, instead of Coulombic, decay in energies calculated.

Generalised gradient approximations (GGA) attempt to improve upon LDA by considering the exchange-correlation dependent on the electron density and its gradient:

$$E_{xc}^{GGA}[\rho_\alpha, \rho_\beta] = \int E_{xc}(\rho_\alpha, \rho_\beta, \nabla\rho_\alpha, \nabla\rho_\beta,)\rho(\boldsymbol{r})d\boldsymbol{r} \tag{3.25}$$

The research presented within this thesis utilises a GGA known as PBE.[149] The gradient terms within GGAs can be constructed using experimental data, however PBE maintains absolute average errors of 5 kcal mol^{-1}[148, 150] whilst maintaining the *ab initio* approach of the simulations contained within this thesis. A more detailed discussion of the performance of various exchange-correlation functionals can be found in Chapter 6.

3.5.2 Plane waves

Within this thesis plane waves are used as a basis to represent wavefunctions. A linear expansion of plane waves can be used to express the one-electorn wavefunction, $\psi_j(\boldsymbol{r}, \boldsymbol{k})$:

$$\psi_j(\boldsymbol{r}, \boldsymbol{k}) = \frac{1}{\sqrt{V}} \sum_{\boldsymbol{G}}^{\boldsymbol{G}_{max}} c_{j,\boldsymbol{k}} e^{-i(\boldsymbol{k}+\boldsymbol{G})\cdot\boldsymbol{r}} \tag{3.26}$$

where $\boldsymbol{G}$ is a reciprocal lattice vector and c_{jk} are coeffecients. Not only do plane waves fufill the orthogonal criteria of a basis set, but in addition they are independent of atomic positions and therefore can represent any system with arbitrary accuracy.

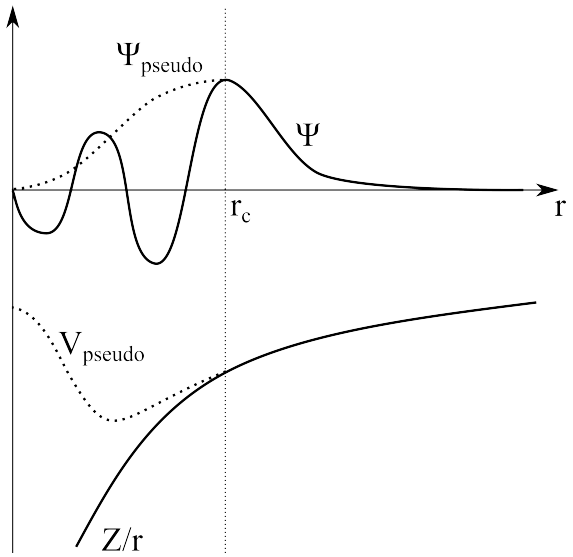

Figure 3.7: Schematic diagram showing the effect on the wavefunction and electronic potential when a psuedopotential is used to replace the complex sections of both these functions.

The size of the plane wave basis is entirely determined by the maximal value $\boldsymbol{G}$. In order to ensure computational accuracy, a calculated parameter is recorded with respect to the parameter $\boldsymbol{G}_{max}$. This results in convergent behaviour of the parameter and allows for an effecient value of $\boldsymbol{G}_{max}$ to be chosen. However the complexity of a wavefunction increases dramatically as they approach atomic nuclei, and indeed a plane wave basis struggles to maintain orthogonality at this limit. This effect can be avoided by using pseudopotentials.

3.5.3 Pseudopotentials

As discussed, wavefunctions fluctuate rapidly as they approach atomic nuclei. However, typically only valence electrons determine the majority of system properties. Therefore pseudopotentials can be used to replace the complex potential close to atomic nuclei, as shown in fig. 3.7, and facilitate a less intensive computation.[151] Within, this thesis ultrasoft pseudopotentials are used.

3.5.4 Brillouin zone sampling

Many system properties in DFT can be calculated by performing integrations over k-points in the Brillouin zone, such as the electron density and the density of states.[152] Integrations over all k-points in the Brillouin zone are computationally infeasible. Since the periodic element of the plane wave wavefunction is weakly dependent on $\boldsymbol{k}$, these integrations can be be approximated as a sum over a finite number of k-points, known as a k-point mesh.[152] Within this thesis, a Monkhorst-Pack (MP)[153] grid was used to sample k-space. In order to achieve accurate system properties, it is important to converge the size of this grid in a similar manner to the basis size discussed previously.

3.6 Summary

This chapter has outlined the various theoretical principles underpinning the research presented throughout this thesis. The physics underpinning the electronic processes of defect formation are complex in nature however understanding of these processes gives a key insight into how systems and equipment can be build to improve fabrication performance. As chapter 5 will demonstrate, research into the fundamental physics of laser fabrication has already proved useful to the practical implementation of the technique. However further understanding is required in order to expand the technique's usefulness into other areas of device fabrication and characterisation. Chapter 6 is one such example of how ultrafast laser fabrication can be used to access unique observables that may prove useful in understanding processes such as defect formation and migration.

This chapter also helped highlight the myriad of parameters that feed into successful defect characterisation. Namely amongst these are aberration control, which provides a powerful tool in defect creation and without which defect formation would be much less flexible and much more difficult if not impossible. As chapter 2 showed, there has yet been a case of defect fabrication by ultrafast laser pulses deep into the solid state without a method of increasing the NA and removing spherical aberrations. It is important to note that whilst any adaptive optical element introduces complexity (and to this authors opinion a degree of complexity that is rarely matched by other methods in optical design) it is important to understand that an adaptive optical element also grants access to additional degrees of freedom that are otherwise impossible to achieve. Whilst this is clearly shown in remote focusing, an adaptive optical element is also capable of modifying the NA of a optical system in real time or producing multiple focal spots through holography.

Chapter 4

Experimental methods

4.1 Introduction

The aim of this chapter is to describe the experimental set-ups used throughout the rest of the thesis. This chapter will begin with a description of common fluorescence characterisation techniques used throughout the thesis. This information is partly repeated in Chapter 5, however due to unique application of the confocal fluorescence microscope found within that chapter the repetition is useful. Additionally this chapter will cover non-optical experimental aspects of the research performed such as information on diamond samples and annealing.

4.2 Optical characterisation

Post characterisation of laser writing colour centres can be primarily performed through optical methods. Due to the fluorescence intensity from single defects this is performed using a confocal microscope in order to effeciently resolve them from the background. Principally fluorescence microscopy is the process of exciting a sample and detecting any resulting fluorescence. Confocal microscopy introduces

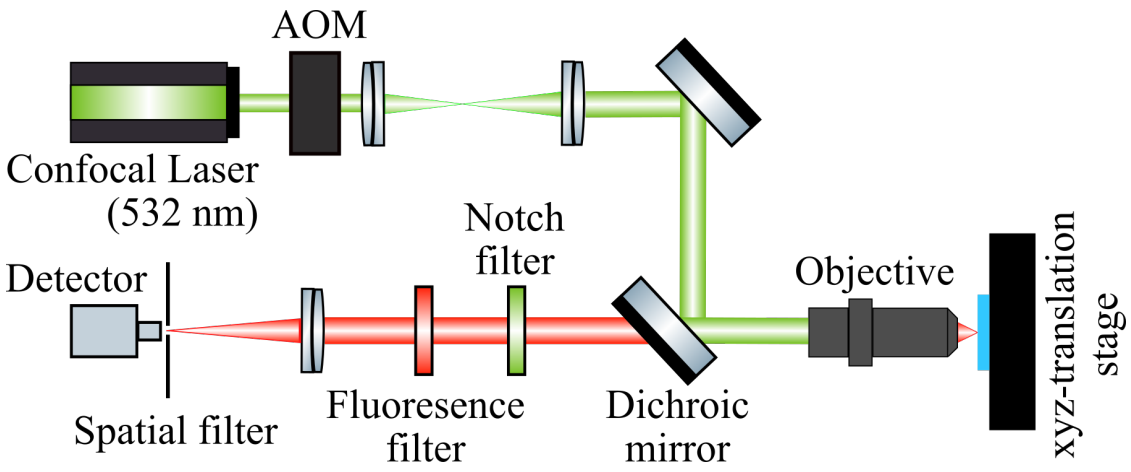

Figure 4.1: Schematic diagram a confocal fluorescence microscope which excites with a 532 nm CW laser and collects the NV^- emission (637 - 800 nm) on a single photon avalanche detector (SPAD). Positional control of the focal spot is acheived through the use of xyz-translation stages.

an aperture into the conjugate plane of the fluorescence, and by reducing the size of the aperture the amount of light outside of the Fourier plane (or "out-of-focus" light) arriving at the detector will also be reduced. This allows for diffraction limited optical sectioning of a sample, which is key to detecting the fluorescence from single defects such as the NV centre in diamond.

Characterisation presented within this thesis was performed using multiple confocal microscopes of similar design, therefore the confocal microscope design presented within this section is representitive of all of these mircoscopes. Fig. 4.1 schematically describes a confocal fluorescence microscope used in characterising an NV^- centre. A 532 nm CW diode-pumped solid-state laser (Laser Quantum gem 532) was used to excite the NV^- with a typical laser power before the objective of $\approx$ 2 mW. A 75 mm lens focused the CW source through an acousto-optic modulator (AOM) (Isomet 1250C-974(M)) capable of gating the CW source to produce pulses. This is useful for performing characterisation techniques that require a pulsed excitation source, however this is not used throughout this thesis

and can be safely ignored. Output light from the AOM was refocused using another 75 mm lens. The beam ($1/e^2 = 0.9$ mm) was expanded by 6.785x to fill the back aperture of the objective. 637 - 800 nm fluorescence from the NV^- was collected through the same objective (Olympus Achromat oil-immersion objective lens, 100x magnification, NA = 1.25) and seperated from the exitation laser using a dichroic mirror (Semrock Di02-R532-25x36).

A 532 nm notch filter (Semrock NFD01-532-25x36) is used to filter out the remaining 532 nm laser light and an additional 630 nm long pass filter (Thorlabs FGL630) is used to filter out additional light from the diamond Raman lines (for 532 nm light; 575 nm and 616 nm) to ensure that only the NV^- emission is detected by the microscope. The beam is then focused with a 200 mm focal length lens into a 62.5 $/mu$m core diameter multimode optical fibre. The spot is magnified such that the core diameter of the fibre couple matches the Airy disk diameter shown in eq. 3.5 to ensure appropriate spatial filtering. Typically single photon avalanche detectors (SPAD) (Excelitas SPCM-AQRH-14-FC-32371) are used to count fluorescence, however this may be replaced with a HBT interferometer (discussed in more detail later in this chapter) or a spectrometer (Acton SpectraPro 500i) with an CCD camera (Princeton Spec-10 100B). Position of the focal spot was controlled through sample translation using 3-axis motion stages (Thorlabs 3-axis NanoMax Piezo stage). Electronic control of the confocal microscopes was performed using a data acquisition card and and controlled using Qudi[154]. A secondary widefield microscope is integrated into the system which can be used to assist with orientation about the sample.

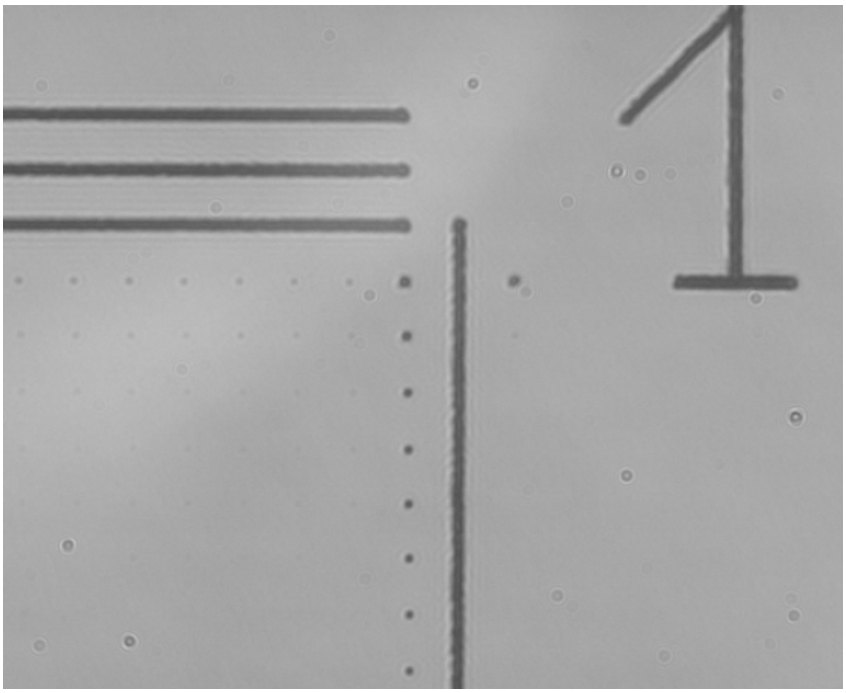

Figure 4.2: 75 μm $\times$ 75 μm widefield transmission image of graphitic marks written 10μm within diamond. Within are large graphitic lines and numbers used for easy identification of array bounds. Additionally graphitic points can be used to signify array rows and very faint graphitic marks that can be used to align a confocal microscopes pinhole against a small near point-like emitter.

4.2.1 Confocal fluorescence imaging

The single NV^- centre is not easily visible in widefield fluorescence microscopy, however laser written graphitic marks are visible in both widefield microscopy and confocal fluorescence microscopy. Due to reflections from the diamond surface (caused by the material's high refractive index) it is typically difficult to see graphitic marks written deeper than 5 μm into diamond. In transmission the graphitic marks heavily absorb and scatter light and therefore appear dark in images. Conversely graphite under confocal excitation produces a large fluorescence emission known as B-band emission[155] which cause the mark to appear bright in fluorescence images. Typically during fabrication, graphitic markers are used to guide characterisation to the correct area. Additionally graphitic point markers can

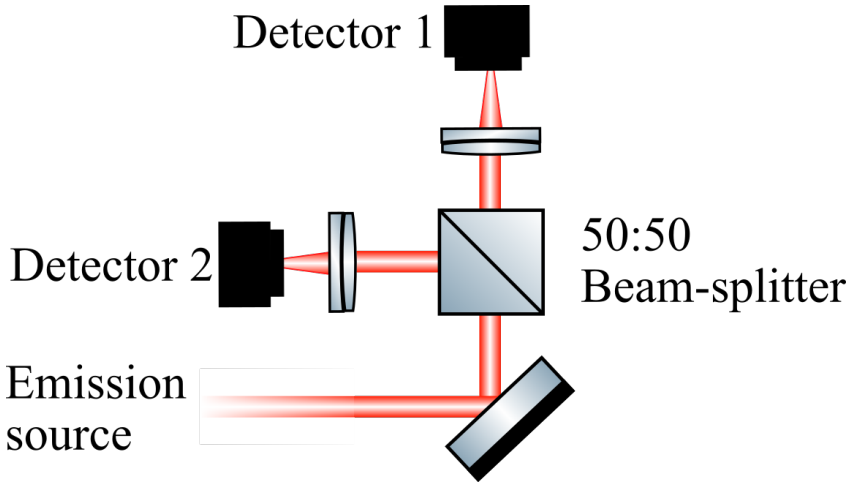

Figure 4.3: Schematic diagram a HBT interferometer. The emission of a defect is collected by a microscope and passed through the inteferometer, the light is than split using a 50:50 beam splitter down identical detection paths. The detection events of the two detectors are then time correlated to determine the singularity of an emitter.

be used to quickly check the performance of a confocal microscope if alignment is required. An example of these graphitic marks imaged by a widefield transmission microscope can be seen in fig. 4.2.

4.2.2 Measuring defect singularity

As discussed in Chapter 3, the singularity of a defect can be measured using a HBT interferometer. A schematic diagram of a HBT interferometer is shown in fig. 4.3. Instead of connecting to a single SPAD, the optical fibre carrying the spectrally filtered emission from the focal spot can be directed into 50:50 fibre splitter and coupled into seperate SPADs (Excelitas SPCM-AQRH-14-FC-32371). The detection events from these two SPADS are time correlated using a Time Tagger (Swabian Instruments).

The photon bunching behaviour described in fig. 3.6 can be reduced before performing HBT measurements. In the eq. 3.15 to eq. 3.19, the transition rate from the ground state to the excited state, k_{12}, is linearly proportional to the

excitation laser power. In the low excitation laser power limit, τ_2 tends towards the spontaneous emission lifetime of the excited state and c_3 decrease towards 0 resulting in the reduction of the photon bunching behaviour. This saturation power, P_{sat} can be found by measuring the NV^- centre's photoluminescence intensity response to the excitation laser power and fitting it to the equation:

$$I(P) = I(P = \infty)\frac{P}{P + P_{sat}} \tag{4.1}$$

where $I(P)$ is the count rate of a NV^- centre at excitation laser power P.

4.3 Diamond samples

Diamond samples used throughout chapter 6 are single-crystal type Ib diamonds produced by high pressure, high temperature (HPHT) fabrication. The sample, provided by De Beers Group Ltd, contained 1.8 ppm subsitutional nitrogen with no pre-existing NV centres within the processed areas. Diamonds were cut and polished to produce faces along the {110} crystal plane.[39]

Diamond samples used throughout Chapter 7 are commercially available single-crystal diamond plates made by chemical vapor deposition (CVD) by Element Six Ltd. The crystals are have {100} orientated faces. The nitrogen concentration within these samples is less than 5 ppb and the boron concentration is less than 1 ppb, as indicated by Element Six Ltd. The diamond samples also have little to no NV centres native witin them and posses a very low (if any) density of intrinsic vacancies. This material was selected due to its low vacancy concentration, which makes it an ideal sample to study NV formation under ultrafast laser fabrication. Additionally, the low intrinsic defect concentration helps preserve the isotopically

limited spin environment of diamond. During laser fabrication the source of nitrogen atoms is due to the 5 ppb substitutional nitrogen concentration.

Before fabriction, the birefringence of the diamond samples are characterised using cross polar imaging. Within the diamond sample is imaged using a linearly polarised transmission light source. Before detection, the transmitted light is passed through a linear polariser to remove any light matching the polarisation of the original light source. This results in dark field images in which the intensity is the result of diamonds birefringence modifying the polarisation of light as it passes through the sample. The origin of such birefringence in diamond is linked the strain[156] and therefore strain-free fabrication regions can be selected. This allows for both the fabrication laser to be uneffected by birefringence during processing and for the NV^- centres to be created within a strain-free environment. It is noted that strain produced in the commercially available single-crystal diamond plates is typically caused by the laser cutting of the diamond after growth and not caused during the growth stage.

4.4 Summary

This chapter has laid out the various experimental processes used throughout this thesis. Notably absent from this chapter is the construction of the ultrafast laser fabrication system itself. In fact, the design and build of such a setup is a considerable amount of the work presented within due to the uniqueness of its design. It is therefore appropriate to give a level of detail into such a system that it warrants its own chapter. Information on this system can be found in chapter 5.

One key thing to note throughout this chapter is that the majority of characterisation techniques presented within are purely optical. This is a natural consequence of the NV^- centres all optical spin initialisation and readout. Therefore its coherent properties can be measured through a purely optical technique. Additionally there has been particular attention paid to end user navigation of the sample. Laser fabrication is capable of producing graphitic structures within diamond which are very useful as markers to laser written NV^- centres. As discussed in chapter 2, these wires could eventually serve a dual purpose of being used as waveguides or electrodes pending future device development.

Chapter 5

Ultrafast laser fabrication system with fluorescence feedback

5.1 Introduction

The chapter will begin with a description of the home built laser fabrication set up, which can be broadly understood as three separate systems. One such system, the confocal fluorescence microscope, is broadly used throughout this research and, in some cases, not linked to laser fabrication itself. This chapter will also address the practical application of adaptive optics, which is used extensively throughout this thesis.

5.2 Ultrafast laser fabrication setup

One of the primary advantages of using ultrafast laser pulses to fabricate colour centres is to exploit the flexibility of having an optical fabrication method. As discussed in chapter 2, the drawback of using other fabrication methods is their inflexibility when it comes to fabricating broadly throughout a material due to the penetration depth of ions or electrons.

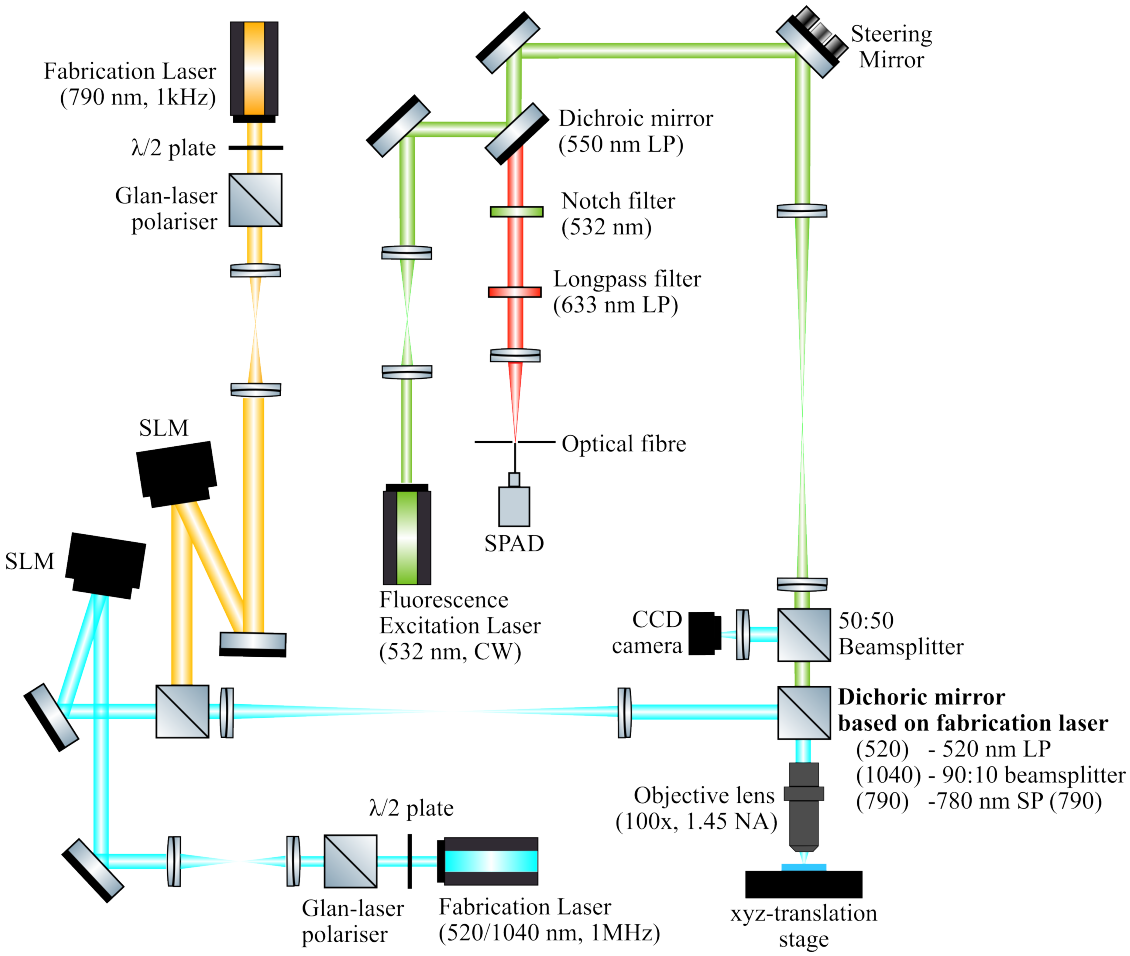

Figure 5.1: Schematic diagram of a homebuilt laser fabrication system. This can be seperated into three subsytems. Firstly a fabrication system for SLM assisted fabrication using 790 nm, 1kHz Ti:S pulses, whose beampath is shown in orange. Secondly a fabrication system for SLM assisted fabrication using 1040 nm (or 520 nm frequency doubled) Yb:KYW pulses with a maximum 1MHz repetition rate, whose beam path is shown in blue. Finally, a beam-scanning confocal fluorescence microscope which excites with a 532 nm CW laser and collects the NV^- emission (637 - 800 nm) on a single photon avalanche detector (SPAD). The excitation laser used in this microscope is shown in green and the filtered fluorescence collected by the microscope is shown in red. Each of these subsystems share a common beam path and objective lens. Additionally there is a widefield transmission microscope which contains a CCD camera for sample imaging.

Any laser fabrication system must be built to be able to preserve this flexibilty and operate sufficiently within the realms of single defect creation and local laser annealing. Much of the research conducted within this thesis uses a homebuilt laser fabrication system, which is illustrated in fig. 5.1. This system was made up of three main subsystems. The orange beam path in fig. 5.1 illustrates a system for SLM assisted fabrication system using a regeneratively amplified Ti:Sapphire laser (Spectra Physics Mai Tai and Spectra Physics Solstice amplifier), 790 nm, with a maximum 1kHz repetition rate.

Power control is achieved through the use of a $\lambda/2$ waveplate (Thorlabs WPHSM05-780) and a Glan-laser polariser (Thorlabs GL5). Adaptive optical elements such as the SLM are polarisation sensitive, so the polariser was positioned to allign with the fast axis of their corresponding SLM. If the output laser light was linearly polarised then the $\lambda/2$ waveplate can then be rotated to modulate the power through the polariser. The modulation of the output power, P, is determined by Malus' Law:[12]

$$P = P_0 \cos^2(2\theta) \tag{5.1}$$

where P_0 is the power before the $\lambda/2$ waveplate and θ is the angle between the $\lambda/2$ waveplate and polariser fast axes. It is important to note that the output intensity of pulsed lasers can be very high before it is modulated, therefore it is necessary to use components that are capable of maintaining function under that laser power. The beam is then expanded to overfill the SLM (Hamamatsu X10468-02), which is then imaged onto the objective ($\times$100 1.4NA Olympus PlanApo) using a 4f lens system (f_1 = 300 mm, f_2 = 250 mm). Further expansion of the beam profile, beyond simply filling the SLM, was used to ensure a uniformly illuminated SLM (instead of Gaussian), however this was at the expense of laser power.

The blue beampath in fig. 5.1 illustrates a fabrication system for SLM assisted fabrication system using 1040 nm (which can be frequency doubled to produce an additional 520 nm laser source) laser pulses produced by a Yb:KYW laser (Spectra Physics Spirit), both wavelengths couple achieve a maximum 1 MHz repetition rate. Power control of this laser is controlled by a $\lambda/2$ waveplate (Thorlabs WPHSM05-514/WPHSM05-1030) and a Glan-laser polariser (Thorlabs GL5) as outlined above. The beam is then expanded to overfill the SLM (dual-band Meadowlark HSP1920-500-1200-HSP8). This beam can then be combined into the same 4f lens system described for the Ti:Sapphire system using a flip mounted mirror.

The pulse duration of the fabrication lasers was measured using an intensity autocorrelator (APE Pulsecheck) and generally falls within the 250 - 350 fs range. The Ti:Sapphire laser source features a compressor which was capable of modulating the pulse length. The pulse length for this system could therefore be remotely controlled using a motor, the response of which is shown in fig. 5.2. The fixed pulse length of the Yb:KYW laser was 330 fs for the fundamental mode and 280 fs for the second harmonic generation (SHG). The average pulse energy was measured before the objective by dividing the measured power of a pulse train by its repetition rate. Note that the systems were engineered such that both fabrication lasers cannot operate simultaneously in order to avoid unecessary laser hazards with using multiple class-4 laser systems in a single enclosure.

Both fabrication systems could be operated in conjunction with a beam-scanning confocal fluorescence microscope in order to monitor the creation of NV^- centres within the focal spot. In fig. 5.2, this is shown by the green beam path and the fluorescence collected from this microscope is shown in red. The details of this microscope are discussed later in this chapter. All systems shared a common

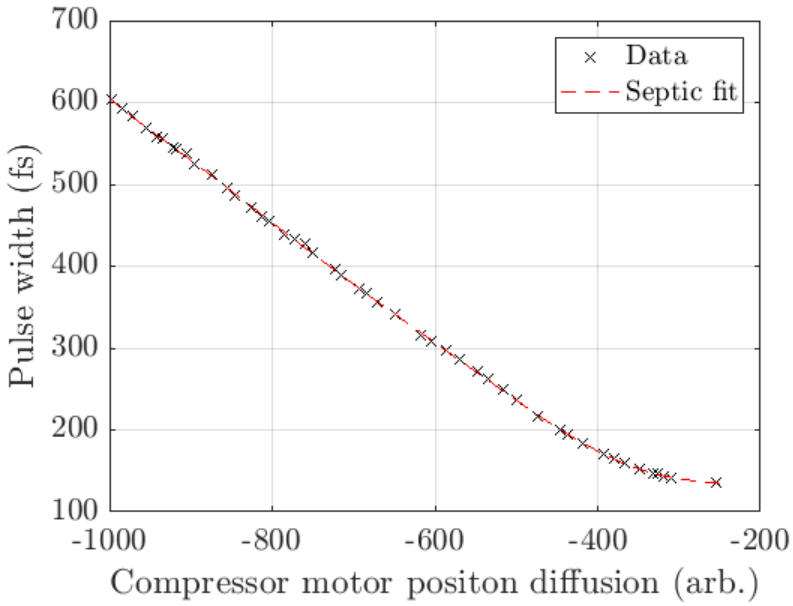

Figure 5.2: The dependence on the pulse width of ultrafast laser pulses produced by the Ti:Sapphire regeneratively amplified laser system as a function of the compressor motor position. The red dashed line indicates a fit to a 7th order polynomial in order for quick calculation of pulse widths.

beam path before the objective lens. Samples were mounted on translation stages (Aerotech x–y: ABL10100; z: ANT95-3-V) to provide 3D control of the sample. The samples were illuminated using an LED embedded into the translation stages for widefield transmission microscopy. All three subsystems shared a common oil immersion objective lens (×60 1.4NA Olympus PlanApo). The electronic control of the laser fabrication systems and confocal microscope was handled through home-built code written to a Field Programmable Gate Array (FPGA) (NI PCI-7830R) with a user interface written in LabVIEW.

5.3 Defect creation

In order to facilitate the creation of vacancies and interstitials (collectively referred to as Frenkel defects), the fabrication lasers must be capable of producing a single

laser pulse at a time. In both laser systems described this is performed using a Pockels cell. Both fabrication systems produce a square wave synchronisation output which can be measured by the homebuilt FPGA control system to determine when a laser pulse is produced by the system. When pulses are requested by the user, the FPGA times the Pockels cell trigger signal to correspond with this synchronisation output so that N (where $N \in \mathbb{Z}^+$) pulses are produced. This control can also be utilised in tandem with G-code used to control the translation stages to allow for the automated fabrication of arrays.

5.3.1 Pulse energy control

Power control implemented within the homebuilt fabrication systems is, as discussed, that of a counter propograting $\lambda/2$ waveplate and a Glan-laser polariser. The laser is pre-attenuated to ensure that normal operating energies can be achieved during the linear region of the cos^2 function in order to ensure a predictable system response. The angle between them is controlled by a DC servo motor (Thorlabs PRM1Z8) capable of making a minimum repeatable incremental motion of 0.03°. From eq. 5.1, this represents a modulation within the linear region of the cos^2 function, of I_0 by 38×10^{-3} %, where the value of I_0 can be preattenuated before reaching the power control. Fig. 5.3 shows the time averaged pulse energy, measured before the objective, transmitted through these waveplate/polariser pairs as a function of the motor controlling the waveplate. In both cases the recorded transmission has been pre-attenuated before the pair and does not represent the maximum laser power capable of being produced by these lasers.

This provides a relationship between the motor position of the $\lambda/2$ waveplate and the throughput pulse energy. Malus' law describes this attenuation as a function

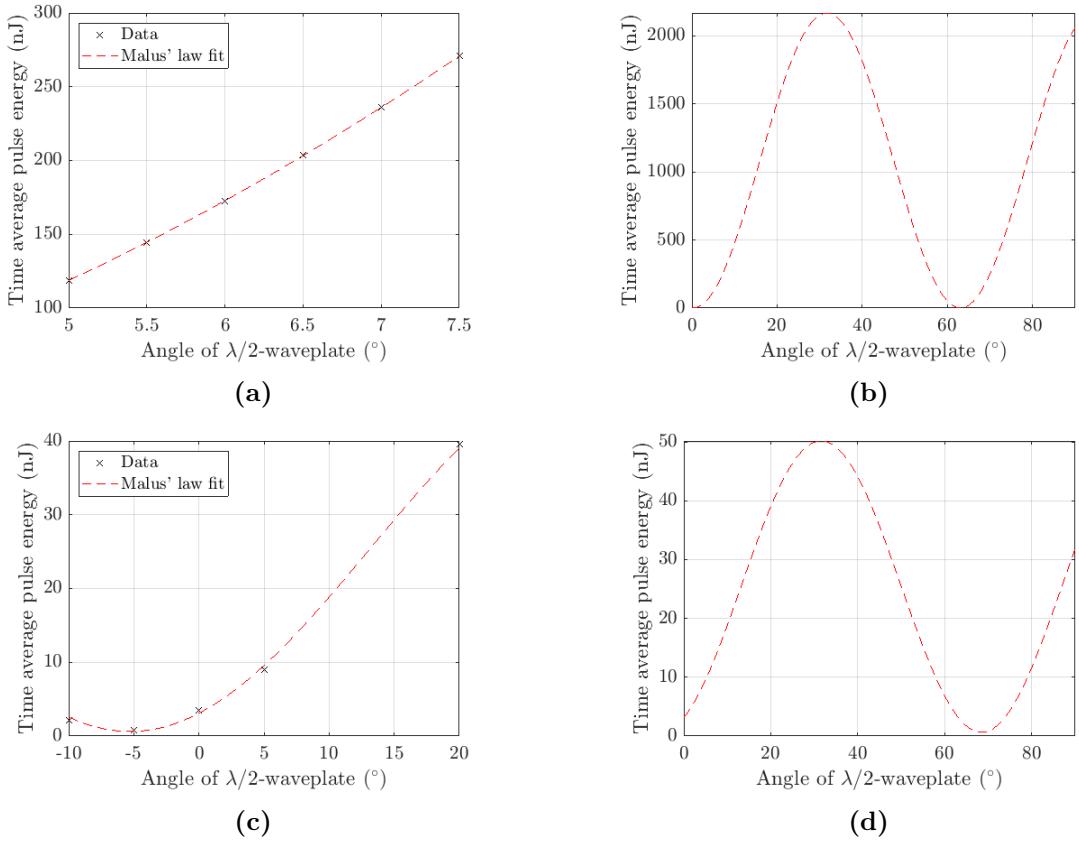

Figure 5.3: The measured time averaged pulse energy transmission before the objective through a $\lambda/2$-waveplate and counterpropograting polariser as a function of the measured motor position of the motor controlling the $\lambda/2$ waveplate. (a) The measured transmission for the Ti:Sapphire (790 nm 1 kHz) system which is fitted to Malus' law which is expanded in (b). (c) The measured transmission for the frequency doubled Yb:KYW (520 nm 1 MHz) system which is fitted to Malus' law which is expanded in (d). Note that a static attenuation has been applied before the waveplate/polariser pair.

of the angle between the fast axis of the waveplate/polariser pair, however this equation can be applied by using the linear relationship between the angle of the motor, θ' and the angle between the $\lambda/2$ waveplate and the polariser.

$$I = I_0 cos^2(2\theta' + c) \tag{5.2}$$

where c is a fitting constant. This calibration allows for a fast determination of the full laser power dependence on the motor control using a handful data points that avoid unecessarily high laser powers to be used. Once these curves have been created they can be adjusted for transmission through the objective lens ($\approx 70\%$)

and can be pre-attenuated to allow the majority of fabrication to occur in the linear region of the $cos^2(x)$ function.

5.4 Laser annealing and fluorescence feedback

The second function of a laser fabrication system is to be able to deliver a train of pulses into the diamond in order to convert fabricated vacancies into NV^- centres. The process of this involves reducing the pulse energy below the graphitisation threshold and excecuting a train of pulses into the fabrication site. The generation of NV^- centres is monitored using an in-situ confocal fluorescence microscope, shown diagramatically in fig. 5.1.

The homebuilt confocal fluorescence microscope uses a 532 nm CW diode-pumped solid-state laser (DPSSL) (Cobalt Samba) to excite the NV^- with a typical laser power before the objective of 2 mW. In order to ensure a flat intensity profile at the pupil the beam is expanded by $\times 50$. The expanded beam is then scanned using a 2-axis galvanometric mirror (Newport FSM-300-01) in order to enable an independent lateral position control of the microscope and fabrication focal spots. The galvometric mirror is imaged onto the back aperture of the objective using a $4f$ lens system. Fluorescence from the NV^- is collected through the same objective and imaged back onto the galvanometric mirror to be descanned and then separated from the excitation laser using a 550 nm longpass dichroic mirror.

A 532 nm notch filter, 633 nm long pass filter and various filters depending on fabrication laser used are then used to ensure that only the NV^- emission is detected by the microscope. The use of a 633 nm long pass filter does potentially cut off the

NV^- centre's 637 nm zero phonon line but, as discussed in chapter 2 the majority of NV^- centre's fluorscence occurs through its phonon side band which is still visible.

The beam is then focused into a fibre coupled single photon avalanche detector (SPAD) (Excelitas SPCM-AQRH-14-FC), where the fibre entrance is used as the spatial filter for the microscope. The spot is magnified such that the Airy disk diameter, shown in eq. 3.5, matches the core diameter of the fibre in order to ensure appropriate spatial filtering. Electronic control of this microscope, such as control over the 2-axis galvometric mirror and counting from the SPAD are integrated into the same FPGA control system that controls the fabrication laser. This allows for fluorescence feedback system to interact fully with the laser fabrication process.

5.4.1 Plasma emission during diffusion

During laser diffusion at high repetition rates ($>$ 100 kHz) the diffusion train contributes significant background counts to the detector, and as the diffusion train approaches 1 MHz this background easily exceeds the NV^- fluorescence intensity by several orders of magnitude. An example of the SPAD detection trace with a 100 kHz diffusion laser on is shown in fig. 5.4a. Fig. 5.5a shows the spectral nature of this background as measured by the confocal micrscope's spectral detection window. Since this background dominates within the NV^- detection window it can not be spectrally removed using filters.

Fig. 5.5b shows the time stamped detection events recorded by the SPAD, wrapped over a 1 MHz time scale. The opacity of the time stamped detections has been reduced in order for each detection event to be visible when overlapped. When the 1 MHz diffusion train is off, the detection events are uncorrelated over

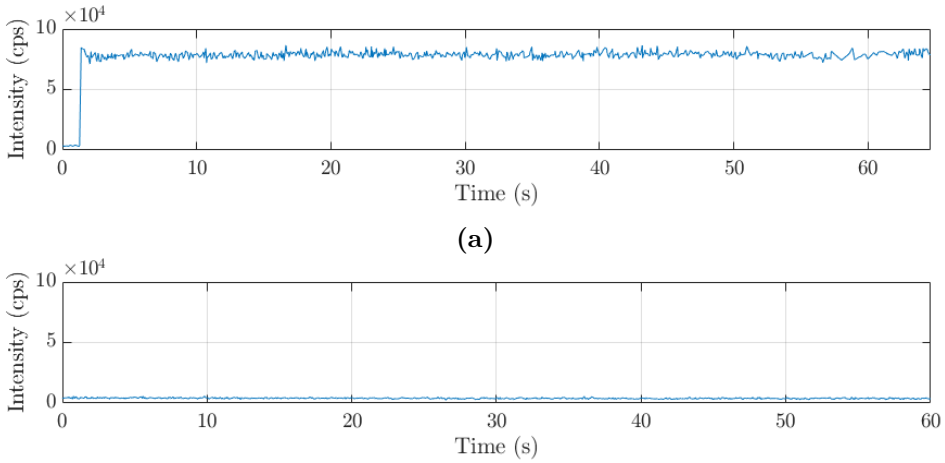

Figure 5.4: During laser diffusion a high repetition rate diffusion train can generate a significant fluorescence background on the detector. The effect on the detection trace is shown in (a). This background can be completely removed by gating the detector such that counts collected during the plasma's brief lifetime are ignored. The effect of such a time gating procedure on the detection trace is shown in (b).

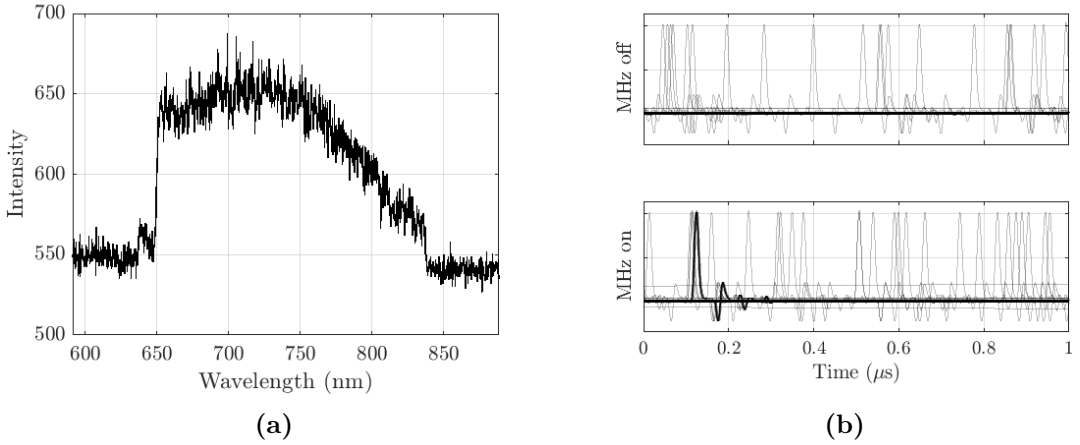

Figure 5.5: During laser diffusion a high repetition rate diffusion train can generate a significant fluorescence background on the detector. This background is shown spectrally in (a), where it coveres the entire NV^- emission window. (b) Shows the when the detection events occur over 1 MHz during diffusion using a 1 MHz diffusion train, the top figure in (b) shows the detection events when the diffusion train is off and the bottom figure shows the detection events when the diffusion train is on. This data was taken using a 520 nm pulse train.

this window. However, when the 1MHz diffusion train is turned on, there is a clear density of detection events occuring within the 100 - 200 ns window. This suggests that source of this background is caused by a short lived plasma generated by the

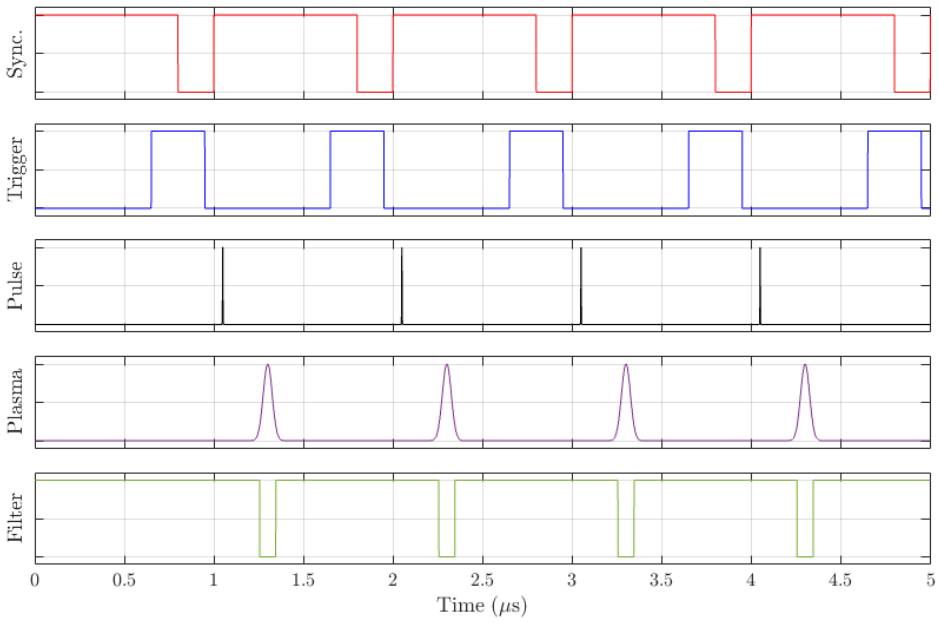

Figure 5.6: Pulse charts demonstrating the mechanism by which the plasma generated from the diffusion pulse is excluded. The sync. pulse train (red) is used to determine when a laser pulse is produced by the laser, and each pulse is gated by the user generated trigger signal (blue). Diagramatically shown are the temporal profiles of the ultrafast pulses (black) and the plasma (purple). Note that the size of these pulses are not accurate and have been exaggerated for the readers convinence. Finally, the detector is electrically gated using a temporal filter (green) which excludes detection events whilst the plasma is active

ultrafast pulses as the temporal nature of this signal is consistent with the plasma lifetimes theoretically predicted by Griffiths *et al.*[135]

The temporal nature of this signal does allow for temporal filtering to exclude this plasma background from the SPAD signal. Fig. 5.6 demonstrates diagramatically the filtering process. Shown in the upper-most pulse chart (red) is the pulse output synchronisation channel from the fabrication laser which is used as in inidication on when each pulse form the laser is gneerated. From this a user generated trigger signal (blue) is used to gate the laser pulses (black). The laser pulse then generates a plasma (purple) repeatably after each falling edge in the synchronisation channel. This allows a pulse signal to be constructed with respect to the initial pulse output

synchronisation channel which can repeatably exclude the detection events caused by the plasma. This filter channel (green) is used to electronically gate the SPADs during diffusion. As shown in fig. 5.4b, with this filtering procedure in effect the plasma background generated by the diffusion laser is completely removed.

5.5 Aberration correction

As previously discussed in chapter 3, a small intense focal spot is necessary to achieve the non-linear fabrication mechanisms possible in wide-band gap materials. However, this is at natural odds with fabricating inside of high-refractive index materials such as diamond. The large refractive index change between the objective immersion medium and the sample surface results in a large spherical aberration of the focal spot, reducing its volume. Low numerical aperture (NA) objectives are less sensitive to this spherical aberration, but do not provide a small enough focal volume to move to the regime of fabricating single localised NV centres, and instead create ensembles of NV centres that aggregate around laser-written graphite.[113]

Aberration correction is applied throughout this work to access high-NA optics that do not exhibit the large aberrations that would otherwise effect such optics. As discussed earlier in this section, this is achieved by applying phase patterns to liquid crystal spatial light modulators (SLM). The SLM use the birefringent properties of the liquid crystal to modify the effective refractive index that is seen by fabrication laser and therefore pre-aberrate the light before it reaches the sample and cancel any aberrations caused by the refractive index change or system misalignment. In chapter 3, the concept of remote focusing was discussed as a method of freely shifting an aberration corrected focal spot axially. Indeed, lateral shifting is also

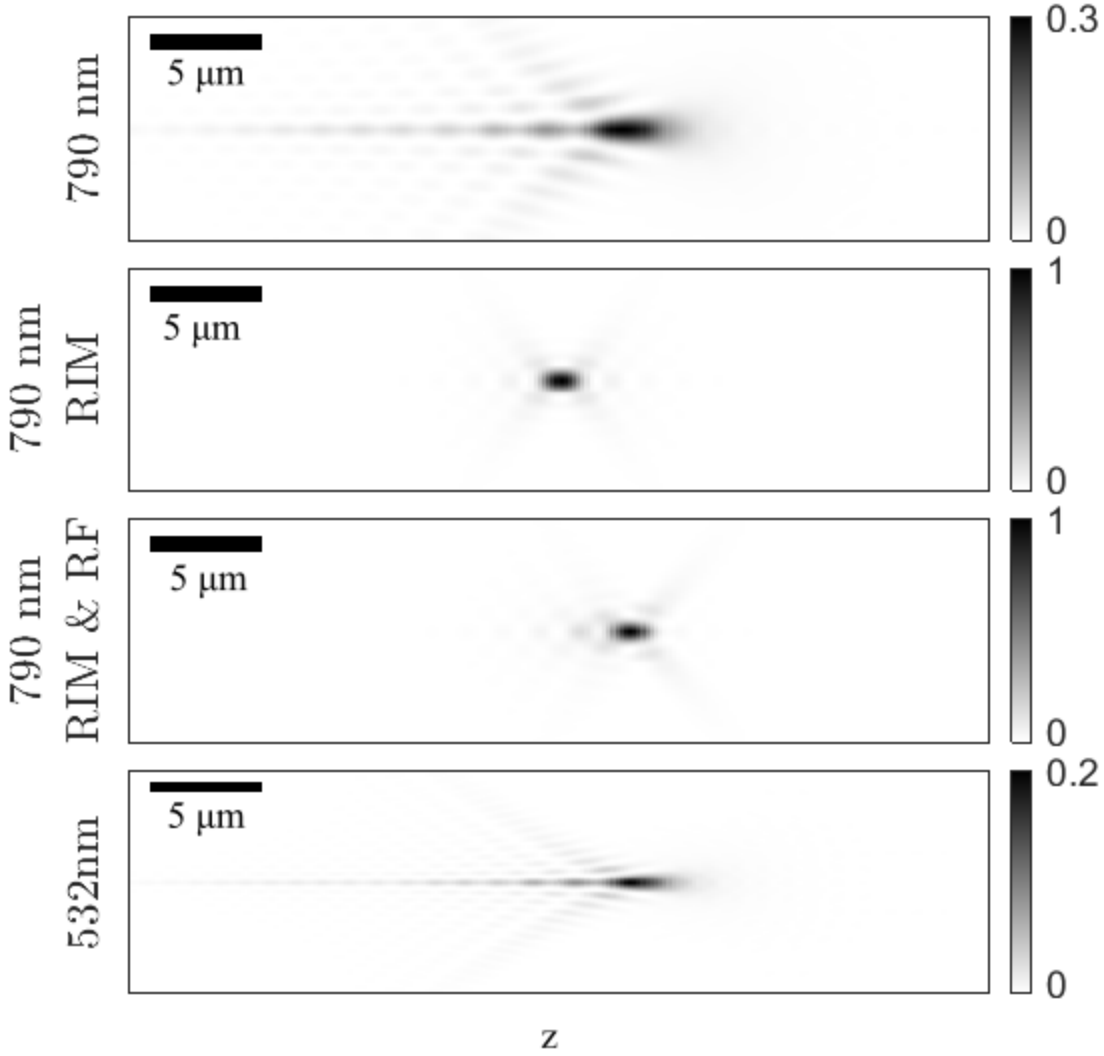

Figure 5.7: Phase-only intensity simulations of a 790 nm ultrafast fabrication laser spot and a 532 nm confocal fluorescence microscope spot focused 10 μm into diamond ($n_2 = 2.4$) using a 1.4NA oil objective ($n_1 = 1.51$). Depth is represented along the horizontal axis. The top and bottom most subfigures represent the 790 nm and 532 nm focal spots respectively, both are aberrated due to the refractive index mismatch (RIM) between the oil immersion medium and the diamond sample. The 790 nm spot is then corrected for the RIM and finally remotely focused (RF) to bring it into the same axial plane as the confocal laser. The intensity of all figures are normalised with respect to RIM corrected focal spot. The scale bars represent 5 μm.

possible using the tip and tilt functions shown in table 3.1. This process of spherical aberration correction and remote focusing is used in tandem throughout this work to produce and aberration free focal spot and then shift it axially to the same focal plane as the confocal fluorescence feedback microscope.

The process of correcting and shifting the focal spot is demonstrated using simulations in fig. 5.7. Within, the phase component of intensity was calculated from the magnitude of the Fourier transform for the phase component of the pupil function. These simulations were performed on a 790 nm ultrafast fabrication laser spot and a 532 nm confocal fluorescence microscope spot focused 10 μm into diamond ($n_2 = 2.4$) using a 1.4NA oil objective ($n_1 = 1.51$). The top and bottom most subfigures represent the 790 nm and 532 nm focal spots respectively, both are aberrated due to the refractive index mismatch (RIM) between the oil immersion medium and the diamond sample. Upon applying a RIM correction the 790 nm focal spot is shifted axially and does not overlap with the confocal microscope's focal spot. This RIM phase correction is calculated by substiuting the depth of focus into eq. 3.9.

The offset between the two focal spots is determined from the fluorescence response of a written graphitic mark by adjusting the stage depth. Adjusting the stage depth naturally adjusts the fabrication laser spots focus depth so the degree of RIM is adjusted to compensate for this change. Finally a remote focus (RF) phase, described by eq. 3.11, is applied to the fabrication laser spot to produce a RIM corrected and remote focused spot which lies at the same depth as the confocal microscope's spot. As mentioned in Chapter 3, remote focusing is entirely determined by the NA, the wavelength of light and the focal shift magnitude, Δ.

As discussed in chapter 3, non-radially symmetric aberrations can be corrected for as well. For convenience these aberrations are represented using the Zernike polynomials represented in table 3.1. These aberrations, excluding the radially symmetric piston, defocus and first spherical aberrations, are applied through a linear combination of radially asymmetric phases, $\Psi_a(\rho, \theta)$:

$$\Psi_{RA}(\rho, \theta) = \sum_i C_i Z_i(\rho, \theta) \tag{5.3}$$

where $Z_i(\rho, \theta)$ are the Zernike polynomials and C_i are weighting coeffecients. Adjusting the coeffecients C_i allows for each phase pattern to be applied to the total phase map and the effect of these aberrations can be observed through the change in fabrication performance. As the intensity profile of the focal spot becomes less aberrated it naturally becomes more intense and thus a lower pulse energy can be used to reach the optical breakdown threshold during fabrication. Therefore a simple pulse energy minimisation protocol can be used to ensure these radially asymmetric aberrations are corrected for. This can be compared to adaptive optic optimisation procedures used in confocal fluorescence microscope, however the process used within requires the active fabrication of a small area of a sample which is not ideal for automation.

These phase patterns are then combined linearly with the phase patterns for remote focus,$\Psi_{RF}(\rho)$, and RIM corrrection, $\Psi_{RIM}(h, \rho)$:

$$\Psi_{total} = \Psi_{RIM}(h, \rho) + \Psi_{RF}(\rho) + \Psi_{RA}(\rho, \theta) \tag{5.4}$$

From this equation, and the full expressions of each phase in chapter 3, it can be seen that once the fixed experimental inputs are set for a given laser wavelength and sample material, the user inputs of stage depth, axial focal spot offset and the

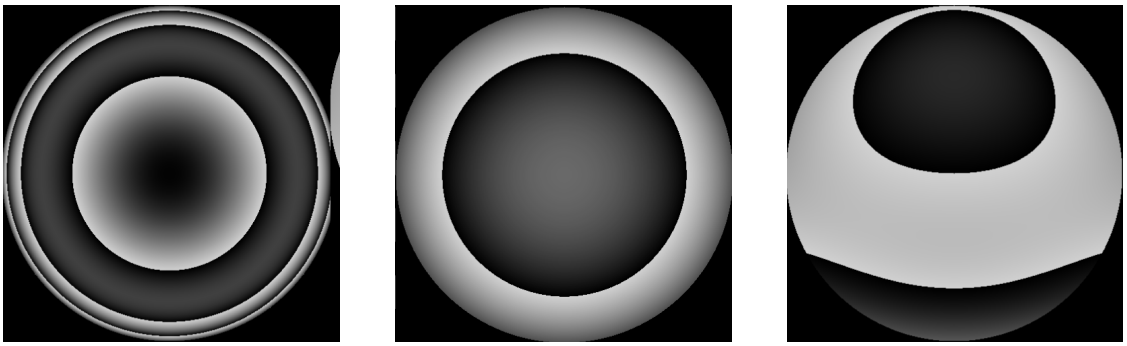

(a) **(b)** **(c)**

Figure 5.8: Examples of seperate phase maps applied to the SLM during laser fabrication of diamond ($n_2 = 2.42$) with 515 nm light using a NA=1.4 oil objective ($n_1 = 1.51$) focusing. (a) RIM correction, Ψ_{RIM}, for focusing 10μm into diamond. (b) A 2μm remote focus, Ψ_{RF}, into diamond. (c) An example of radially asymmetric Zernike modes, Ψ_{RA}, here $C_i = 0.5$ of Z5 (astigmatism) and Z7 (coma) have been applied.

coefficients C_i can be used to correct for aberrations in the system. An example of seperate phase maps for each of the terms in this equation are shown in fig. 5.8.

5.6 Summary

This chapter has explored the design and construction of an ultrafast laser fabrication system with a confocal fluorescence monitoring system. As discussed such a fabrication system must be capable of both single defect creation and laser diffusion. Whilst this is in itself is a complex system the added complexity of a confocal microscope provides a unique window into observables that may prove useful in understanding processes such as defect formation and migration, which is explored further in Chapter 6.

Superficially, the development of such a system may seem like a trivial step up from other lower repetition rate fabrication systems. However it has been shown the factor of 1000 increase in repetition rate proposed additional challenges to defect creation. Ultimately this system much be able to create single defects within

diamond and this chapter has tackled several challenges in being able to actually detect a single defect under such high intensity diffusion.

As a brief aside the author feels the need to point out an aspect of adaptive optical design, albeit not entirely relevant to the research presented within this thesis. It is discussed throughout this chapter that SLMs are limited to correcting a narrow window of wavelengths and polarisations and another common AO device, the deformable mirror, does not have these drawbacks. Deformable mirrors modify the phase at the pupil by physically deforming to introduce an additional path length, and therefore phase, to sections of the pupil. However the size of a similarly priced deformable mirror is (at the time of writing) typically only 40 to 80 actuators across, whilst the pixel density of an SLM is typically much higher. This allows for a much finer aberration correction during laser writing. An additional point in this area is to note that SLMs can be used to create holographic patterns by modulating phase and intensity, instead of purely phase modification as presented in this thesis. The additional intensity modulation does allow one to achieve intensities beyond what the diffraction limit will allows. However, there are applications of this use of an SLM to create multiple focal spots and even graphitic patterns within the diamond.

As discussed in chapter 2, Simmonds *et al.*demonstrated the application of a dual DM and SLM fabrication setup to produce graphite in diamond, where the deformable mirror is capable of correcting for large amplitude aberrations, whilst the SLM can be used for finer tuning.

Chapter 6

Ab initio simulations of interactions of between laser written defects

6.1 Introduction

As an alternative to thermal annealing, the processed site can be exposed to a low energy ultrafast pulse train which delivers enough energy to the lattice to migrate the vacancy through the lattice.[39] The formation of an NV^- centre can be monitored using a confocal fluorescence microscope to observe the 637 - 800 nm fluorescence window. The principle of this method can be understood through energetics. Lagomarsino *et al.* reported on a detailed study of non-linear photoionisation of diamond by Ti:Sapphire laser pulses wherein the intensity required for optical breakdown is 1-10 $TWcm^{-1}$.[103]

Further investigation by Griffiths *et al.* modelled Frenkel generation via the recombination of a bound biexciton as the electron plasma cools which demonstrated a good agreement with experimental data,[135] and within it was assumed that the minimum energy required for defect generation was 8 eV based on the 7.14

eV formation energy of the neutral vacancy[157] and the 0.6 eV energy difference between a perfect diamond lattice and the Frenkel defect[158]. Where formation energy is defined as the energy difference between the perfect diamond lattice and one containing a single neutral vacancy. In contrast, the neutral vacancy and carbon self-interstitial diffusion have comparably low activation energies of 2.3 eV and 1.6 eV respectively. Therefore, by reducing the ultrafast pulse energy, vacancy migration can be achieved without further Frenkel defect generation in the lattice.

Additionally, the confocal fluorescence monitoring system provides a unique window into defect formation dynamics. A common fluorescence trace can be seen in fig. 6.1a, where transient fluorescent events are detected before the NV centre emits stabily. An example of the stable emission from the NV^- after these fluorescence transients is shown in fig. 6.1b. Chen *et al.* suggested these transient detections are due to the formation of an NV centre being disrupted by a nearby carbon self-interstitial.[39] The existence of these transients represent a unique window into the single defect formation process which has not yet been realised. Unlike many post processing fabrication techniques ultrafast laser pulses do not prohibit the use of accurate diagnostic tools, such as confocal fluorescence monitoring, which are capable of measuring changes to single defects.

This chapter presents the first use of ultrafast laser fabrication to investigate single defect formation, in particular that of the negatively charged NV centre in diamond. Density Functional Theory (DFT) is used to investigate the interactions between the NV centre and the carbon self-interstitial involved in laser writing and report on simulations which suggest that the intermittent fluorescence spiking could be caused by the NV's emission being suppressed by interactions between the two defects. This chapter investigates simulated strain and electronic interactions

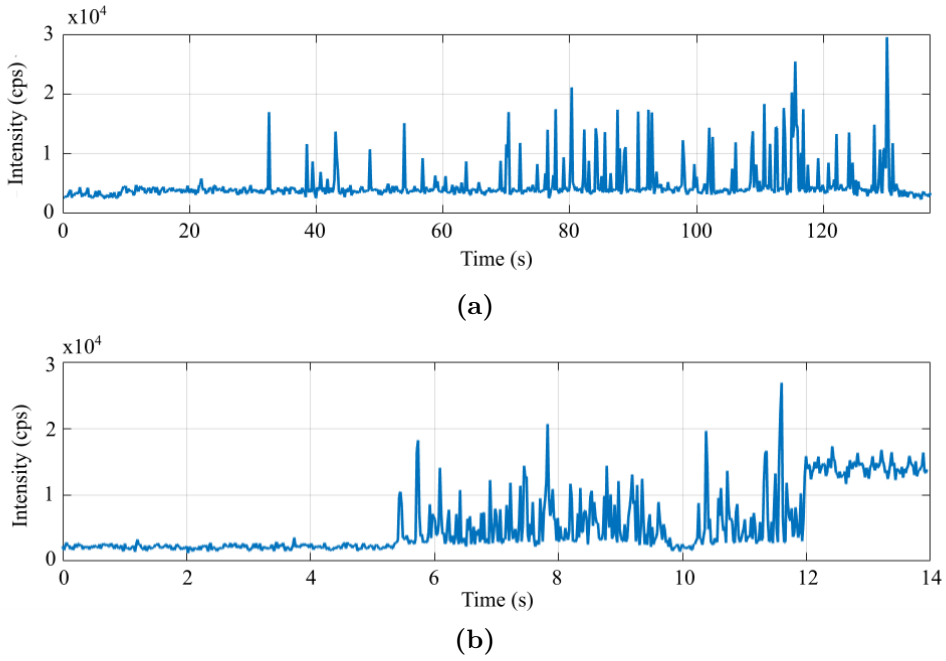

Figure 6.1: (a) An example fluorescence trace of the NV^- emission window during the laser diffusion of defects in diamonds, this figure demonstrates the transient peaks that occur before the fluorescence signal is stabilised. (b) An example of this fluorescence trace where in which an NV^- centre emission stabilises at the 12 s mark and after which the transient behaviour stops.

between the two defects and the effect of these interactions on the NV centre's band structure and the specific excitation pathway that leads to NV emission. Additionally, we use a simple Monte-Carlo random walk to demonstrate how this model translates into the observed transient detection events.3.

6.1.1 Experimentally observed transients

As presented by Chen *et al.*[39] deterministic creation of NV^- centres in 1.8 ppm nitrogen containing diamond can be achieved. This fabrication is performed using the Ti:Sapphire (790 nm) 1kHz laser described in chapter 5 to produce deterministic NV^- centres in 1.8 ppm nitrogen containing diamond. As reported the NV^- centres are stable in the negative charge state during diffusion within no photoluminescence reported from the NV^0 charge state. Vacancies, or more precisely Frenkel pairs,

are created using a single laser of energy 27 nJ and pulse width of 250 fs. Defect migration was achieved by a subsequent train of pulses of energy 19 nJ in which the fluorescence of the NV^- centre's spectral window is monitored.

During the diffusion process a commonly observed phenomena is the presence of transient peaks in the fluorescence prior to the stabilisation of the NV^- centre fluorescence signal. An example of these transient peaks can be shown in fig. 6.1a. Importantly, if the diffusion pulse train is terminated during one of these transient peaks, a stable NV^- signal remains. Furthermore Chen *et al.* reported no signal from the NV^0 during diffusion, thus these transient peaks are unlikely to be the result of rapid charge state switching.[39] Diagnosing the spectrum of these transients are difficult since the signal from the transients is very low, however only the NV^- emission window is monitored during diffusion so the likelihood of the emission being caused by other defects is unlikely.

6.2 Convergence tests

As discussed in chapter 3, convergence tests are required to determine appropriate values for various parameters used throughout this chapter's simulations. Such variables include the plane wave basis size, the supercell size, the k-point sampling size, the pseudopotential form and the type of exchange correlation functional used. The functionals tested within this chapter are the LDA and three GGAs; PBE, RPBE and PW91.[149, 150, 159, 160] In addition, two pseudopotentials are tested. Firstly the norm-conserving pseudopotential described previously and an ultrasoft pseudopotential in which the norm-conserving restrictions are lifted.

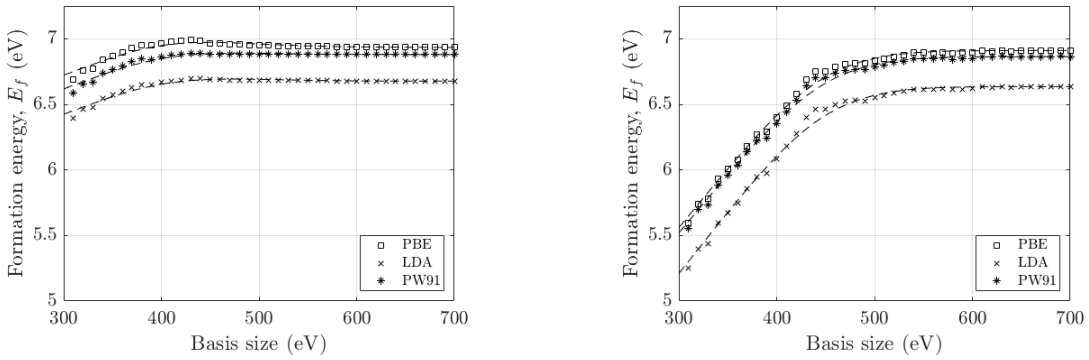

(a) USP **(b)** NCP

Figure 6.2: The convergence of the formation energy of the NV centre in diamond, with respect to basis size, for different exchange-correlation functionals. The pseudopotentials used in these calculations are (a) ultrasoft pseudopotentials (USP) and (b) norm-conserving pseudopotentials (NCP).

Convergence tests are performed by a parameter using various configurations of the mentioned variables and determining convergent behaviour in the calculated parameter. Within this section we present convergence tests for the formation energy, E_f, of an NV centre in diamond which was calculated by:

$$E_f = E_{tot} - (\mu_N + n_C \mu_C) \tag{6.1}$$

where E_{tot} is the total energy of the NV centre simulation, n_C is the number of carbon atoms within the simulations and $\mu_{N/C}$ is the chemical potential of nitrogen and carbon respectively. These chemical potentials where calculated using ammonium for nitrogen and a pure diamond lattice for carbon. During these calculations all other parameters were kept consistent whilst only changing the basis size.

Fig. 6.2 demonstrates the convergence of the formation energy of the NV centre in diamond, with respect to basis size, for different exchange-correlation functionals. In addition, this figure compares the difference in this convergent behaviour between the two pseudopotentials. These are ultrasoft pseudopotentials (USP) and norm-conserving pseudopotentials (NCP), which put additional restrictions

on the pseudopotential known as the Hamann-Schluter-Chiang conditions.[161] Comparing the two pseudopotentials shows that ultrasoft pseudopotentials leads to a reduction in converged basis size of approximately 25%. In addition this pseudopotential leads to a more consistent value for the converged formation energy across the exchange-correlation functionals trialled.

This could be attributed to the difficulty in developing accurate norm-conserving psuedopotentials for first row elements, such as carbon and nitrogen.[162, 163] However it is the case that in lifting the norm-conserving conditions the pseudopotential is allowed to take a form that further reduces the complexity of the wavefunction within the core region, reducing the basis size. Therefore the pseudopotential used throughout this chapter, unless otherwise stated, is ultrasoft pseudopotentials with a basis size of 600 eV.

The formation energy of a NV centre in diamond has been calculated through DFT to be 6.21 eV,[164] using the HSE06 exchange-correlation functional.[165–167] HSE06 is particularly reliable since it has almost no self-interaction error in diamond,[164] however the functional is non-local leading to computation times that are much too long for the scope of research proposed within this chapter. Formation energies of the neutral NV centres using PBE does not appear to have a well defined literature value, since HSE06 is typically used, so a direct comparison is not available.

From this convergence test it seems all functionals appear to perform similarly when compared to HSE06, apart from LDA which provides a more accurate formation energy. However PBE was chosen as the exchange-correlation functional due to increased previlance of literature surrounding the functionals use in diamond. In

addition, due to collaborations associated with this project, it was decided that the simulations within this thesis used PBE in order to remain consistent with prior work.

The Monkhorst-Pack (MP)[153] grid spacing was converged to be 0.075 $Å^{-1}$ and decreasing the MP grid spacing by 0.05 $Å^{-1}$ lead a change in formation energy of <1 meV. The diamond lattice parameter was calculated to be 3.59 Å. Deak *et al.* determined the lattice parameter to be 3.57 Å using PBE with a 0.034 $Å^{-1}$ grid spacing. For reference the precise diamond lattice constant is 3.567 Å. Decreasing the grid spacing any further, however, was not possible for the work within this thesis due to the scale of the simulations and time constraints.

6.3 Defect interaction

6.3.1 Strain interactions

In order to investigate strain field interactions the strain fields surrounding the interstitial and vacancy were simulated. Each defect state was placed in an isolated $3 \times 3 \times 3$ diamond supercell and the geometric ground state was calculated using BFGS-based geometry optimisation. A variable cell geometry was considered optimised based on the minimisation of four parameters, the two most relevant of which, due to their direct relationship to strain, was the maximum change in any atomic position and the maximum force allowed on any atom. The tolerance of which was set to 0.001 Å and 0.05 eV/Å, respectively. In the case of the <100>-split interstitial, the supercell used was expanded, along the defect axis, to $3 \times 3 \times 6$ due to the range of its strain field. The effects of the strain field on the band structure of the NV^- centre were calculated by placing the NV^- centre in a $3 \times 3 \times 3$ supercell and applying the appropriate lattice deformation to the supercell.

Fig. 6.3a shows the relative magnitude of the strain fields surrounding the <100>-split interstitial and the vacancy. The vacancy demonstrates a small localised negative strain field close the the defect state however the interstitial strain field is of a much higher magnitude and longer range. As shown in fig. 6.3c, this strain field is highly directional along the defect axis. This would suggest that strain field interactions would therefore be dominated by the <100>-split interstitial if the other defects lie along the interstitial axis.

The effects of the simulated strain on the NV centre's emission bands are shown in fig. 6.3b. The strain field was applied perpendicular to the NV axis since parallel strain only resulted in a slight perturbation of the a-e energy gap. Which is expected since a parallel strain field would not break the symmetry of the e-manifold. It is seen that this strain results in a splitting of the otherwise degenerate e-manifold. When the interstitial is within 4.5 Å of the NV centre the energy levels are split by 75 meV, however the splitting rapidly increases, as the defect separation approaches 6.1 Å, to 280 meV. The phenomenological behaviour of these bands are consistent with theory developed by Davies *et al.* for uniaxial stress applied to the NV centre.[26, 168]

Strain fields in diamond have already been demonstrated to be capable of splitting the e-manifold of the NV centre, leading to spectral broadening of its fluorescence line width.[169, 170] The substitutional nitrogen defect strain field has been shown to create strain in the lattice[171] which has been suggested to be why the single substitutional is an efficient vacancy trap.[172] However, in cases where the interstitial is nearby, its large compressive strain field will likely disrupt that action or lead to recombination. However, this does support the idea that strain field interactions may cause competition during NV formation, a thought expanded at the end of this chapter.

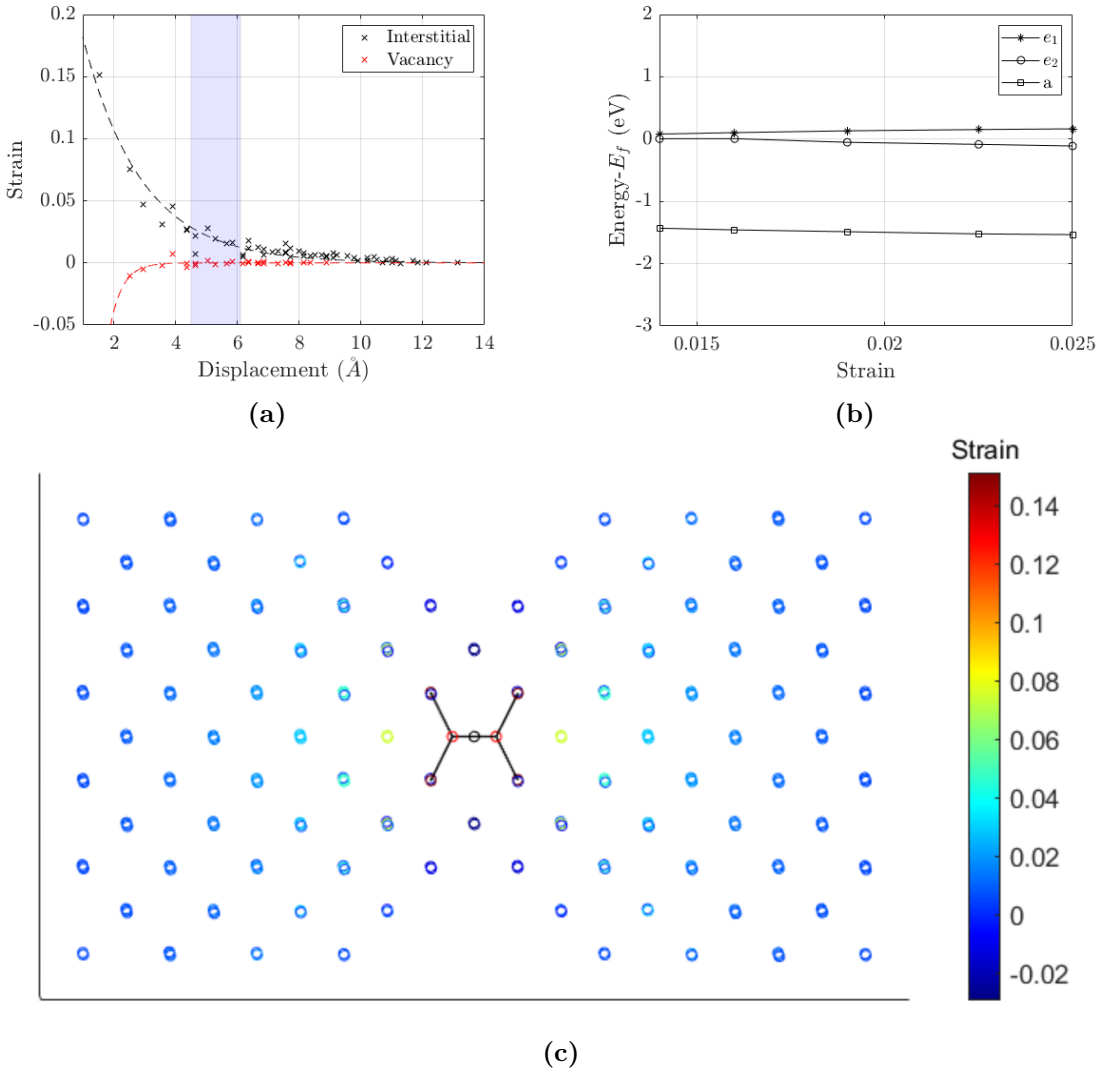

Figure 6.3: (a) The simulated strain field in the diamond lattice surrounding a vacancy and <100>-split interstitial. The interstitial strain field is sampled along the defect axis due to its high directionality. (b) The behaviour of the NV centre's band gap energy levels as a function of lattice strain. The strain sampled corresponds to a spatial separation, between the NV and <100>-split interstitial, shown by the blue shaded area in figure (a). (c) A diagram of the compressive strain field surrounding the <100>-split interstitial.

6.3.2 Electronic interactions

Electronic interactions between configurations of the NV centre and <100>-split interstitial were simulated by generating all symmetrically unique second and third near neighbour ensembles of the two defects in $3 \times 3 \times 3$ carbon supercells. The basis size is increased to $\approx 150\%$ of the calculated converged value for electronic interactions. Due to the large amount of configurations it was not computationally viable to calculate convergence tests for each individual case, therefore a healthy overestimation of the basis size was employed. Values with literature references, such as bond lengths and unit cell size, were monitored to ensure the stability of the simulations under this new basis size. After geometry optimisation of each ensemble their new structures were used to calculate band structures. The c2x programme was then used to extract volumetric orbital data from the band structures.[173] In some cases there was significant electronic interactions occurring through the periodic boundary conditions of the super cell. Such cases were identified by extending the offending boundary, resulting in a $3 \times 3 \times 6$ supercell. In all cases these interactions would be prevented by extending the super cell size to $3 \times 3 \times 6$.

By examining the isolated band structures of the NV^- centre and the interstitial we can identify that the electronic interactions are likely to occur between the energetically similar NV e-manifold and the degenerate π-orbitals of the Ic. Some configurations of the <100>-split interstitial and the NV centre demonstrate hybridisation between the defects. Out of the 48 total configurations simulated, 8 lead to reconstruction and 15 resulted in hybridisation. In such cases hybridisation occurs between one of the degenerate π-orbitals of the <100>-split interstitial and the *e*-manifold of the NV centre in the ground state. The π-orbital involved in

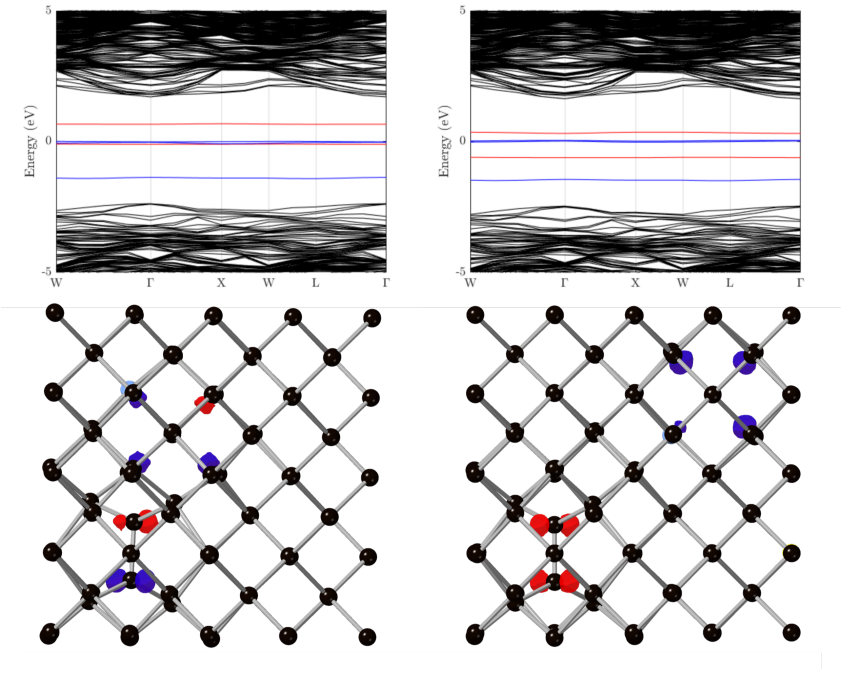

(a)

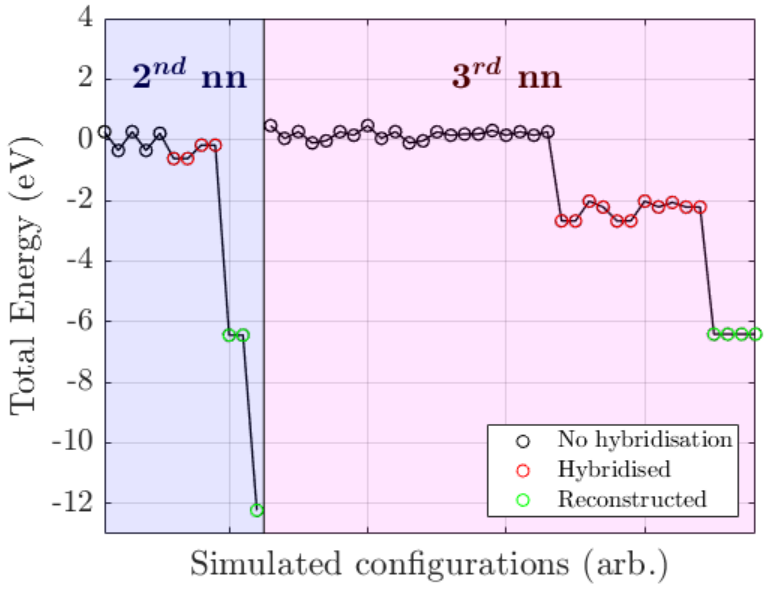

(b)

Figure 6.4: Band structure and orbital population plots of the electronic interactions between a NV^- centre and <100>-split self interstitial in diamond, where (a left) the defect centres have hybridised and (a right) where they have not. Hybridisation occurs between the NV centre's e-manifold and the π-orbitals of the interstitial. In both plots the energy levels in the band structure and the orbital populations have been colour coded blue for the NV centre and red for the interstitial. (b) A plot of the energy difference between each simulated configuration of the two defect centres, where reconstruction and hybridisation occur with a distinct drop in the energy compared to un-hybridised configurations.

hybridisation is usually the closest to the NV centre. Hybridisation does not occur with the a orbital surrounding the nitrogen atom since it is energetically distinct from the <100>-split interstitials orbitals. It is also noted that in nearly every configuration results in breaking of the interstitials degenerate energy states which is more significant the closer the two defects are to each other.

Electronic hybridisation may lead to the creation of non-radiative path ways for fluorescence, which would quench the NV emission since the decay through these pathways is typically much faster than the lifetime of the NV centre excited state. The excited state that leads to the NV^- centre's fluorescence does not involve the population of previously unoccupied states, but rather a change in the population of occupied states relative to the ground state. Therefore this hybridisation is likely to also occur in the excited state. Fig. 6.4b shows that at the 3 nearest neighbour position, the energy difference between hybridised and non-hybridised configurations is approximately 2 eV. Such an energy gap is comparable to the vacancy and carbon self-interstitial activation energies of 2.3 eV and 1.6 eV respectively and it is therefore reasonable to assume that, if these defects are able to migrate under the laser diffusion train, then their configurations could not be trapped into a hybridised arrangement.

6.4 Simulated diffusion SPAD traces

Fig. 6.5 shows a map of all of the positions configurations of the <100>-split interstitial that results in hybridisation with the NV. This map is expanded to include symmetrically degenerate configurations and those cases in which the

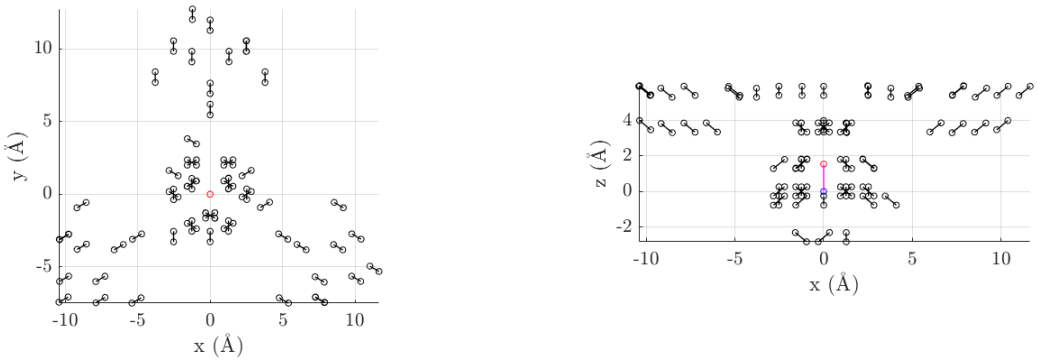

(a) **(b)**

Figure 6.5: (a) a x-y map and (b) x-z map of all of the combinations of carbon self-interstitial and NV^- centre which result in hybridisation. This map includes combinations which are not simulated but are symmetrically equivalent to simulated combinations. The z axis corresponds with the $\langle 111 \rangle$ direction.

boundary conditions suggest a longer range interaction. From this figure we can see that there are two general instances in which hybridisation occurs.

Firstly, at shorter ranges ($\leq$ 5 Å), the interstitial is able to hybridise with the e-manifold regardless of the orientations of the defects. Secondly, at longer ranges ($\leq$ 15 Å), hybridisation is limited to an interstitials that exist on the vacancy side of the NV centre. In the second case, hybridisation can occur over much longer distances. Geometrically this is consistent with the localisation of these orbitals which are formed by anti bonding between the dangling bonds that point into the vacancy from the three carbon atoms that surround it.

A potentially important result in the longer range cases is how hybridisation only occurs when the interstitial is closer to the vacancy than the nitrogen atom. This observation opens an interesting dynamic for fluorescence spiking, where the nitrogen atom of the NV centre can migrate into the vacancy's position, essentially inverting the orientation of the NV centre. The energy barrier height of this migration has been reported to be 4.8 eV[157, 174, 175] which is less than the formation energy

of the NV^- centre and therefore accessible to the laser annealing process. It is important to note that the NV^- centre inverting is not itself solely responsible for the intermittent spiking. It has been observed that once the NV^- centres emission signal has stabilised, it typically remains stable under further exposure to the diffusion train. If the NV orientation flipping was the sole mechanism for florescence spiking then we should reasonably see no stable phase in the experimental SPAD traces.

This mechanism for the observed experimental phenomena can be explored further using a Monte Carlo simulation model. By simulating a random walk of interstitials on the diamond lattice around a NV^- centre one can build a pattern of the NV^- centre hybridisation as migration occurs over large time scales.

6.4.1 Outline of simulation

Within a discrete random walk is used to migrate interstitials around an NV^- centre on a diamond lattice. Using the geometry of hybridised configurations shown in fig. 6.5, the emission of the NV^- centre can be turned on and off over time. A full and detailed breakdown of the Monte Carlo simulation can be found in Appendix A.

A discrete random walk is justified as an appropriate way of simulating the motion of defects under laser diffusion so long as there is no interaction between laser pulses. Griffiths *et al.* demonstrates that the plasma formed during Frenkel defect generation decays within 1 ns of the pulse[135] and there is therefore no interaction between the plasma generated from a pulse and the subsequent pulse at a 1 kHz repetition rate. Additionally there has been no reported regime of cumulative heating in diamond, this is due to diamond's high thermal conductivity. Evidence of this can be found by solving the heat equation in diamond, as shown in Appendix B.

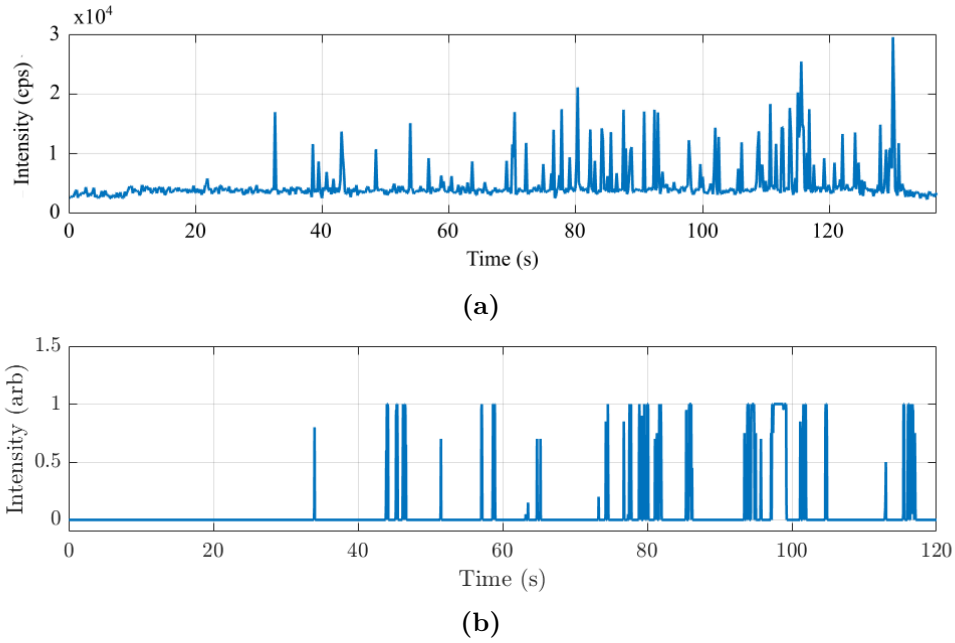

Figure 6.6: Examples of SPAD traces during NV^- formation in low purity diamond. (a) Experimentally observed transients during diffusion with a 790 nm 250 fs 1 kHz diffusion train. (b) Diffusion traces simulated by a Monte Carlo method using the hybridisation model of NV^- fluorescence suppresion. This demonstrates that the transient fluorescent signal can be replicated phenomenologically using the Monte Carlo simulation presented.

6.4.2 Comparison to experiment

Fig. 6.6 shows typical examples of experimentally observed and simulated SPAD traces. It can be seen that using hybridisation model to control the fluorescence of an NV^- centre during the described random walk simulation produces transients of similar phenomenological nature to those seen experimentally. The simulation even accomodates for phenomena such as transients being of different intensities, which is thought to be a consequence of how long the NV^- is able to fluoresce before it is suppressed.

These peaks can be counted in order to determine the dependence of the frequency of the transient peaks with respect to the diffusion pusle energy and diffusion pulse width. Peak counting is performed automatically using the first

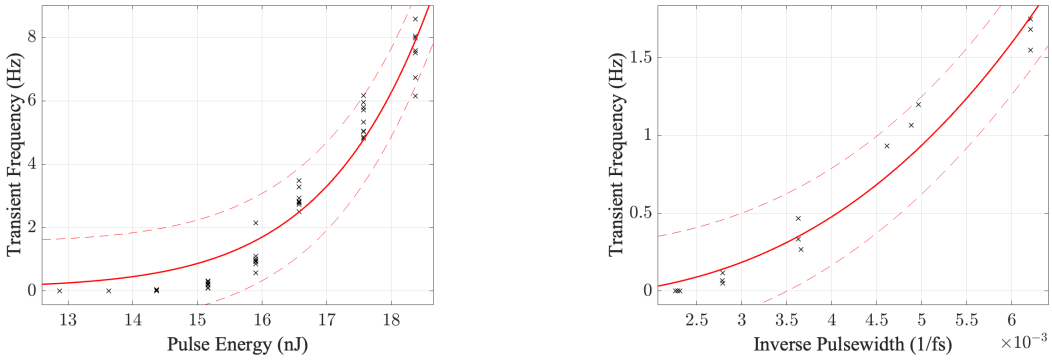

(a) **(b)**

Figure 6.7: The dependence of the frequency of transient peaks that occur during ultrafast laser diffusion of NV^- centres as a function of (a) diffusion pulse energy and (b) diffusion pulse width. The pulse energy and width of the seed pulses used to create this data set remained constant thoughout. Each data set was fit to the equation $y = Ax^B + C$ in order to determine the nonlinearity of the processing. The dashed red lines represents the 95% confidence interval of the fit.

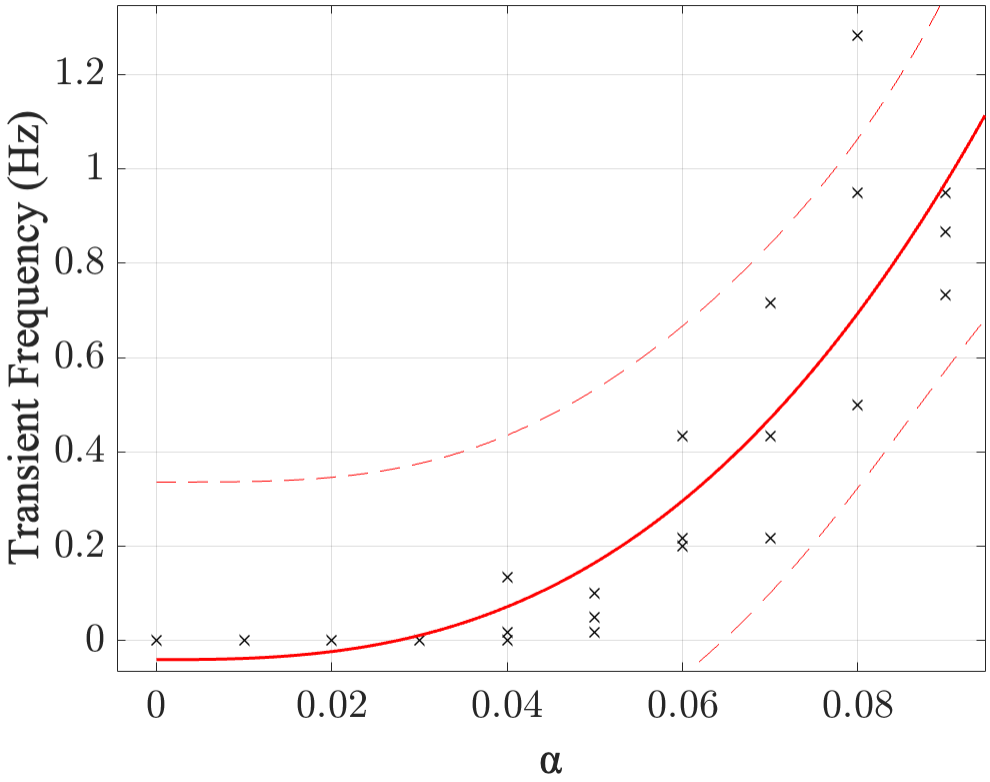

Figure 6.8: The simulated dependence of the frequency of transient peaks that occur during ultrafast laser diffusion of NV^- centres as a function of the free energy variable α. The dashed red lines represents the 95% confidence interval of the fit.

derivative of the trace to find turning points in the signal and then these turning points by their corresponding signal intensity (i.e. filtering turning points on the peaks from turning points in the noise).

Experimentally there are two available controls with which to influence the diffusion traces. The pulse width and the pulse energy, both of which can be independently controlled to establish a dependence between the controls and the frequency of the transient peaks. A Ti:Sapphire (790 nm) pulsed laser, as described in Chapter 5 was used for vacancy creation and diffusion within 1.8 ppm substitutional nitrogen containg diamond. Within both of these experiments the seed pulse energy used to create the vacancies was 21 nJ and the pulse width 250 fs. The seed pulse was kept constant throughout all fabrication attempts. Each processing site was exposed to a diffusion train of 60 s duration, and the resulting detector traces were collected. In fig. 6.7a the diffusion pulse width was kept at 250fs whilst the pulse energy was modulated between fabrication sites. In fig. 6.7b, the pulse energy was kept at 16 nJ whilst the pulse width was modulated between 150 and 400 fs using a compressor described in chapter 5.

An interesting result of this experiment is the different non-linear dependence in controlling the pulse energy and pulse width. Both these datasets have been fit to the power function $y = Ax^B$. In fig. 6.7a, the dependence of the frequency of transient events with pulse energy is seen to have a non-linearity of $B = 11.53 \pm 0.26$. This non-linearity is significantly less than the non-linearity seen in optical feedback mechanisms for Frenkel pair generation, which is typically ≈ 30. In fact the non-linearity shown here is similar to that seen in exciton generation,[135] suggesting that this lower energy diffusion processes is mediated by excitons. The evidence for exciton mediated diffusion is further discussed in Chapter 7.

The processes involved in laser writing are non-linear with respect to the number of photons, and therefore typically investigated with respect to pulse energy. However the width of a pulse is directly related the pulses spectral bandwidth, thereby influencing those nonlinear processes. This effect is investigated in fig. 6.7b, where the non-linearity produced by modulating pulse width is a factor of 4 lower at $B = 2.80 \pm 0.13$ when compared to modulating the pulse energy. A secondary effect on this non-linearity is likely caused by the reduction in free carrier absorption and subsequent impact ionisation seen in shorter pulse fabrication.[176]

This same analysis can be performed on the Monte Carlo simulated detector traces. By varying the free energy parameter α one can build an equivalent dependence on the transient frequency. This is shown in fig. 6.8, and this dependence demonstrates a fitted non-linearity of $B = 2.97 \pm 0.26$ which demonstrates a similar non-linearity to that seen experimentally by modulting the pulse width, however it also demonstrates poor agreement with the non-linearity shown by sweeping pulse energy. It is important to note that the singular free energy parameter used to control the energetics in a random walk does not capture the full complexity of the intensity profile during laser writing. Griffiths *et al.* demonstrated the non-linearity involved in vacancy creation is heavily influenced by the objective lens NA, wavelength, pulse energy and the pulse duration.[135] These influences are likely present, although somewhat more difficult to probe experimentally, in the diffusion process. It is also likely that the relationship between pulse parameters and the parameter α is not necessarily linear as this analysis presumes. Finally, it shows that the theory of hybridisation being the root cause of the transient peaks can produce similar behaviours in the SPAD trace to those seen experimentally.

6.5 Summary

This chapter has presented a unique study of using the confocal feedback system to produce observables that can be used to inform theoretical studies in defect interactions. Such a study demonstrates the value of ultrafast laser fabrication to the greater fields of defect formation and migration. These observables, when combined with studies of electronic and strain interactions between the NV^- centre and the carbon self-interstitial in diamond, have been used to inform a Monte Carlo simulation which agrees with the experimental observables.

Additionally, it is important to note that this is just one of the models presented to explain the origin of these transients. Chen *et al.* initially proposed a model that does not assume the NV^- centre is formed before any transient events and that the NV^- centre formation is perturbed by the strain field of a nearby interstitial leading to a successive formation and destruction of the NV^- centres photoluminescence orbitals. This chapter does suggest that the strain field is insufficient to disrupt the fluorescent orbitals of NV^- centre. however did not investigate dynamic distortions of the NV^- centre. Evidence for this could be found through nudged elastic band (NEB) simulations[177] which would determine if the NV^- centre is physically perturbed enough to disrupt its fluorescence.

The chapter also demonstrates how the in-situ confocal fluorescence monitor can generate observables that might provide a key insight into defect migration and creation. The optical window into these processes is unique, especially in its used of high NA optics and sensitive detectors. Typically these processes occur during thermal annealing which produce additional design constraints and thermal noise to any optical probe.

Chapter 7

Deterministic fabrication of NV^- centres in high purity diamond

7.1 Introduction

As discussed throughout this thesis, Chen *et al.* pioneered a technique of determinsitic fabrication of NV centres in diamond.[39] This technique involved a single high energy ultrafast laser pulse to generate vacancies inside of the diamond. Instead of thermally annealing, a low energy 1 kHz pulse train can be used to migrate the vacancies to form NV^- centres with subtitutional nitrogen. NV creation can therefore be monitored using an in-situ confocal fluorecence microscope to monitor the NV^- fluorescence window and termiate the diffusion train once a stable NV^- signal is detected.

Whilst this process was a step forward in NV^- fabrication it had only been demonstrated in a single non-standard sample and could not be replicated in commercially available diamond. Moreover, this diamond sample is of 1.8 ppm N concentration and there was little known about the prescence of other defects within. This raises questions about whether this deterministic fabrication scheme is reproduceable and its true impact in photonic devices. The motivation for

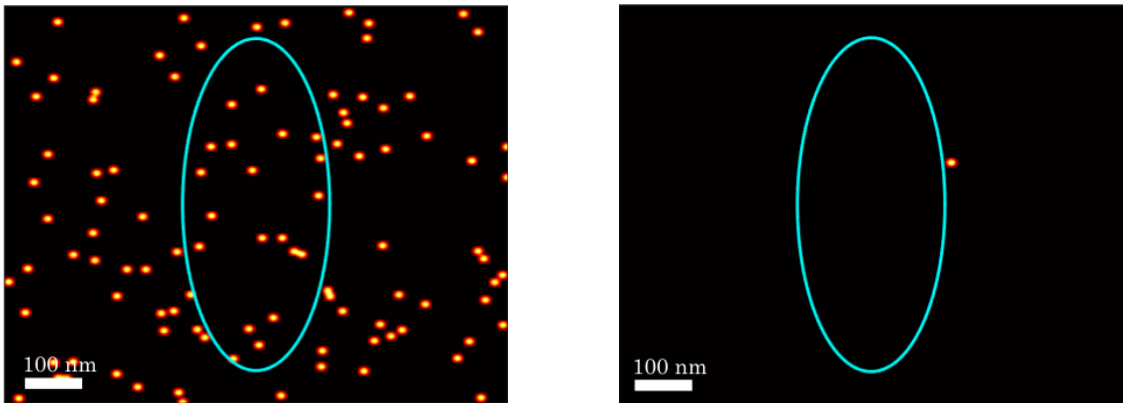

(a) **(b)**

Figure 7.1: Schematic diagrams of the difference in nitrogen concentration across a 2D slice of a diffraction limited focal spot represented by the teal ellipse. Concentrations represented are (a) 1.8 ppm and (b) 1 ppb.

answering these questions is that a determinsitic NV^- fabrication technique would be a dramatic step forward in NV^- based quantum devices. Such a technique would also be able to benefit from laser writings high fabrication accuracy and much more flexible writing as discussed in Chapter 2.

This Chapter reports the successful implementation of deterministic NV^- fabrication within commercially available high purity diamond. This chapter will begin with an outline of the fabrication process, which is significantly different to that reported by Chen *et al.* before moving onto reporting various characterisations of the fabricated NV^- centres.

7.2 Fabrication process

Within the quantum diamond community, a commonly used and commercially available high purity single crystal diamond is typically of 1 ppb nitrogen concentration and no other defects. This represents a factor of 1000 reduction in nitrogen concentration compared to the diamond used in Chen *et al.*[39] This significant

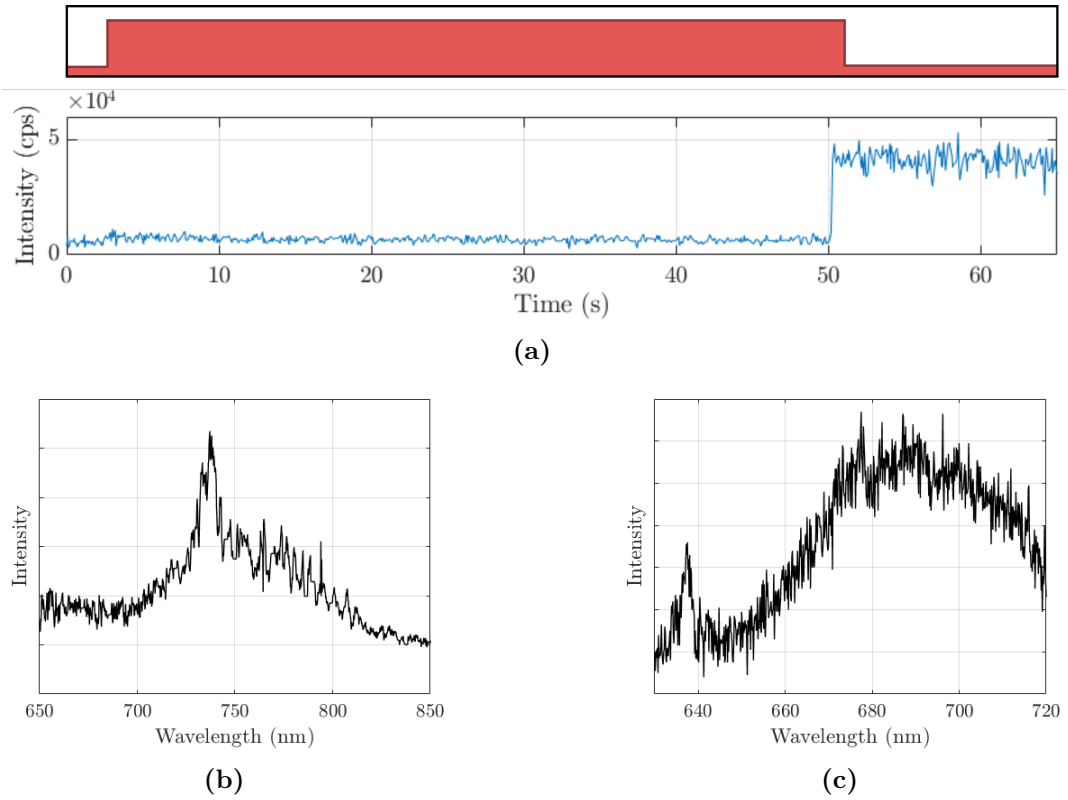

Figure 7.2: (a) Typical detector trace of the NV^- fabrication process. The red pulse chart demonstrates when the diffusion pulse train is on. (a) Spectral feature indicating the generation of isolated vacancies after the seed pulse and (b) the characteristic NV^- spectral feature measured after the jump in the detector trace at 50 s.

change can be diagrammatically seen in fig. 7.1. These diagrams are produced by populating a blank image with bright pixels at the corresponding concentration of substitutional nitrogen, a Gaussian blur filter is then applied in order to make each bright pixel more visible. This dramatic reduction in the available nitrogen dramatically increases the effective path length a vacancy must travel in order to form an NV^- centre. For 1.8 ppm nitrogen containing diamond the average seperation between nitrogen atoms is $\langle r \rangle \sim 1/\sqrt[3]{n} = 21.7$ nm, where as for 1 ppb nitrogen containg diamond this increases to 178 nm. As a result, previous attempts to fabricate NV^- centres in such high purity material without adequtely high repetition rates demonstrate that the effects of drift within a laser system precludes any length annealing.[178]

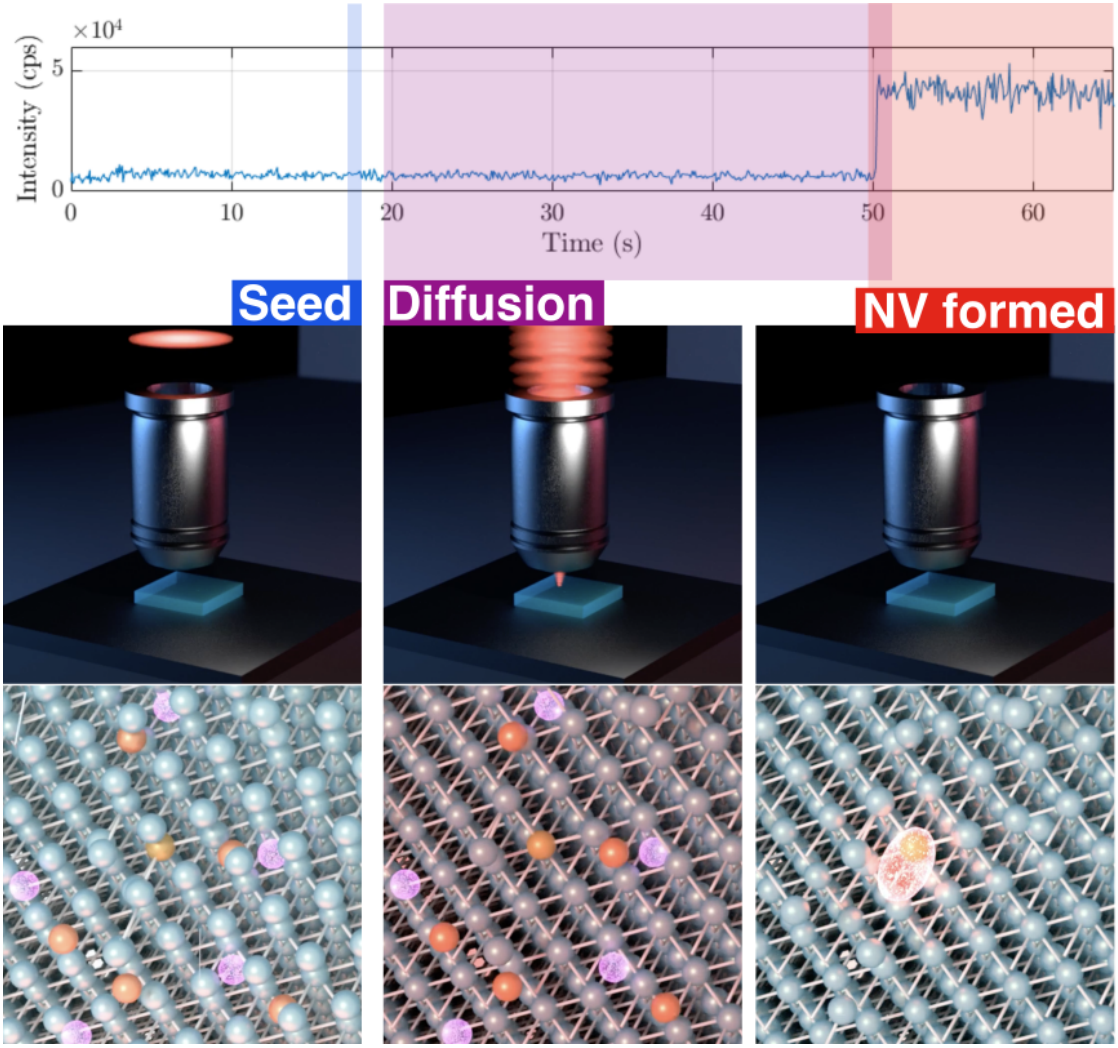

Figure 7.3: A diagramatic break down of the laser fabrication process. The line plot represents the counts from the *in-situ* confocal fluorescence microscope. The process begins with a single high energy seed pulse, which creates vacancies (shown in the diamond structure render as pink) and interstitials (shown in red). This is followed by a low energy pulse train which diffuses the vacancies and interstitials. When a vacancy finds a substitutional nitrogen atom (shown in orange) it forms an NV^- centre and the emission from that defect can be measured on the fluorescence monitor. The diffusion pulse train is then switched off and the NV^- centre remains stable. Images rendered by Dr. Shannon Nicley and reused with permission.

In order to perform fabrication within this high purity material a homebuilt 1 MHz repetition rate fabrication system was used. This system used a 520 nm frequency doubled Yb:KYW laser (Spectra Physics Spirit) with an in situ beam-scanning confocal fluorescence microscope to monitor NV^- creation. In order to achieve a small focal spot a 1.4 NA oil objective was used to focus light into the diamond, in addition this system used a SLM to correct for aberrations produced by the oil-diamond interface. The use of an SLM additionally allows the implementation of remote focusing techniques to allow for independent control of the xyz positioning of the fabrication laser and confocal fluorescence focal spots. This system, and other key insights that made deterministic fabrication possible is presented with more detail in Chapter 5.

The process of ultrafast laser fabrication is shown diagramatically in fig. 7.3. A single high energy ultrafast laser pulse is used to drive vacancy generation in diamond. During this process the in situ confocal microscope can monitor the generation of vacancies within the diamond.[179–181] This can be confirmed by the weak GR1 spectral feature observed after laser writing, as shown in fig. 7.2b. Throughout this chapter a seed pulse energy of 1.65 nJ was used.

Following the generation of vacancies, the pulse energy can be reduced to typically 90% of the seed pulse energy and a train of ultrafast laser pulses are delivered at 1 MHz in order to diffuse the vacancies and produce NV^- centres. The generation of NV^- centres is monitored using the detection trace from the confocal fluorescence microscope. A typical detection trace is shown in fig. 7.2a, where at the end of the diffusion process there is a step-like increase in the fluorescence intensity which remains stable after the termination of the diffusion train. Spectroscopy of

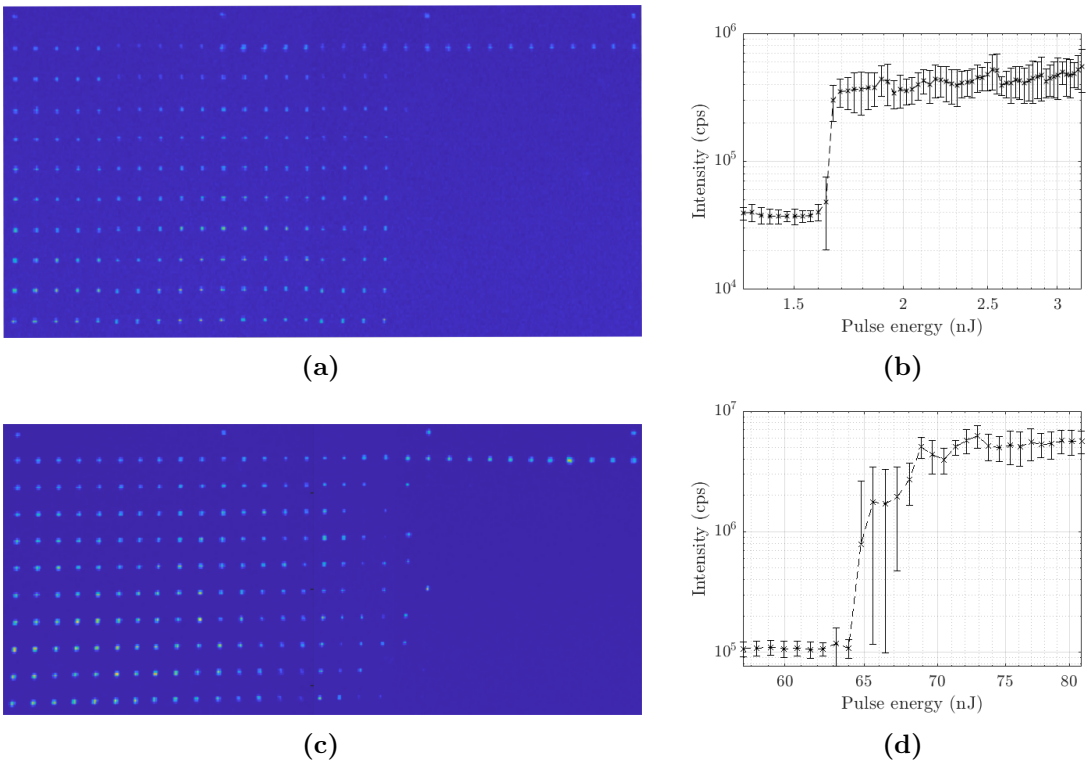

Figure 7.4: Example of vacancy array created through single pulse fabrication. Fabrication arrays were created using (a) 520 nm pulses and (c) 1040 nm pulses. Fabrication sites decrease in pulse energy from left to right, with each column being repeat fabrications at a single energy. The top most row of each array are markers denoting each column. The fluorescence intensiy of these points are plotted in log graphs for (b) 520 nm light and (d) 1040 nm light.

the fabricated emitters demonstrates a characteristic spectral feature, confirming the creation of a NV^- centre, as shown in fig. 7.2c.

7.2.1 Wavelength dependance on fabrication

Defect creation is using ultrafast laser fabrication is a challenging milestone for a fabrication system to achieve. Griffiths *et al.* demonstrated that the wavelength, NA and pulse duration have a significant effect on the generation of Frenkel defects at the focal spot.[135] The simplest way to determine the boundary of vacancy creation is to measure the material's response to a single pulse and different pulse energies. Fig. 7.4 demonstrates this technique with the Yb:KYW laser using both the fundamental

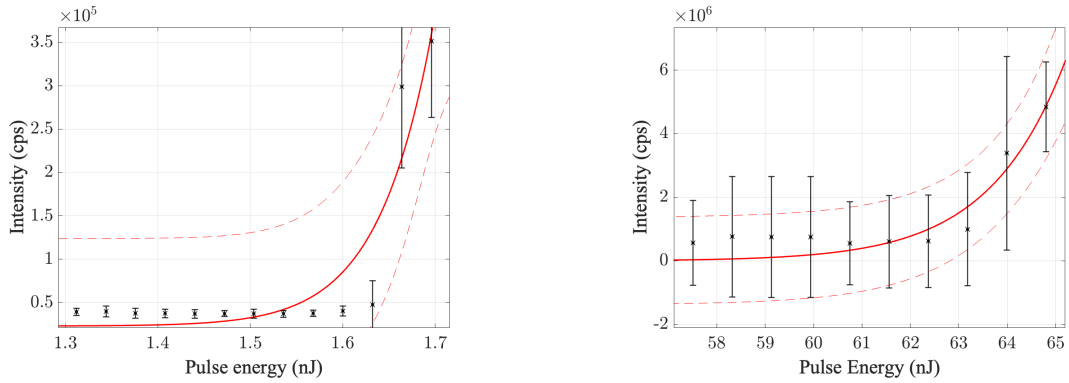

Figure 7.5: The non-linearity of vacancy creation after a single pulse of (a) 520 nm and (b) 1040 nm light. The estimated non-linearity is 28.69±3.13 and 41.56±4.31 respectively. These fits are calculated using the S-curves in fig. 7.4b and fig. 7.4d. The linear graphitic regions of these curves are excluded to find the non-linearity in vacancy creation. The dashed red lines represent the 95% confidence interval of the fit.

1040 nm wavelength and its 520 nm second harmonic. Confocal fluorescence images of the arrays fabricated with 1040 nm pulses and 520 nm pulses are shown in figs. 7.4c and 7.4a respectively. These images were produced by the confocal fluorescence microscope described in Chapter 5. Fabrication sites decrease in pulse energy from left to right, with each column being repeat fabrications at a single energy. The first row are intentional graphitic marks that serve as visual aid markers for the columns.

Figures 7.4b and 7.4d show the intensity of these fabricated array sites as a function of pulse energy. Each S curve generally shows three regimes from low pulse energy to high. Firstly there is a region of no fabrication, where there is no breakdown of the materials. As pulse energy is increased the flourescence at the array points increases, indicating the generation of some fluorescent defects. Griffiths *et al.* demonstrated this is an indication of when vacancy formation begins to occur at the focal spot.[135] This behaviour can also be seen using 790 nm Ti:Sapphire pulses in research conducted by Chen *et al.*[104]

The non-linear behaviour of this vacancy creation is shown in fig. 7.5 and the

estimated non-linearity is 28.69±3.13 and 41.56±4.31 for 520 nm and 1040 nm pulses respectively. These fits are calculated using the S-curves in fig. 7.4b and fig. 7.4d. The linear graphitic regions of these curves are excluded to find the non-linearity in vacancy creation. These values of non-linearity are consistent with the concept of multiphoton ionisation. As photon energy is decreased the number of photons required to excite an electron across the bandgap is likewise increased. Griffiths *et al.* reported the nonlinearity for an equivalent system with 790 nm light was 33,**??** which agrees well with the results presented here. Finally, as pulse energy is further increased this fluorescence increase begins to asymptote, an indication of the phase change from sp3 phase diamond, into a semi sp2 phase of graphite.[104]

Importantly from these figures it can be seen that the pulse energy required for graphitisation using 520 nm pulses is ≈1.75 nJ, which is significantly lower than the ≈70 nJ pulse energy requirement for 1040 nm pulses. The demonstrated dependence of the wavelength on vacancy creation shown here is the first confirmation of the results simulated by Griffiths *et al.* and demonstrates a change in the non-linear nature of defect formation in diamond.[135] Additionally second phase of modification in diamond, that of vacancy formation, is significantly larger for 1040 nm pulses then it is for 520 nm pulses. This demonstrates a key consideration that must be taken into account when designing a fabrication system in terms of a systems ability to control the pulse energy.

7.2.2 Vacancy fluorescence decay

As reported by Chen *et al.*[39] diffusion with a 1 kHz train in a high N containing diamond results in commonly observed transient peaks in the fluorescence trace before an NV^- centre forms. However these transient peaks are very rare under

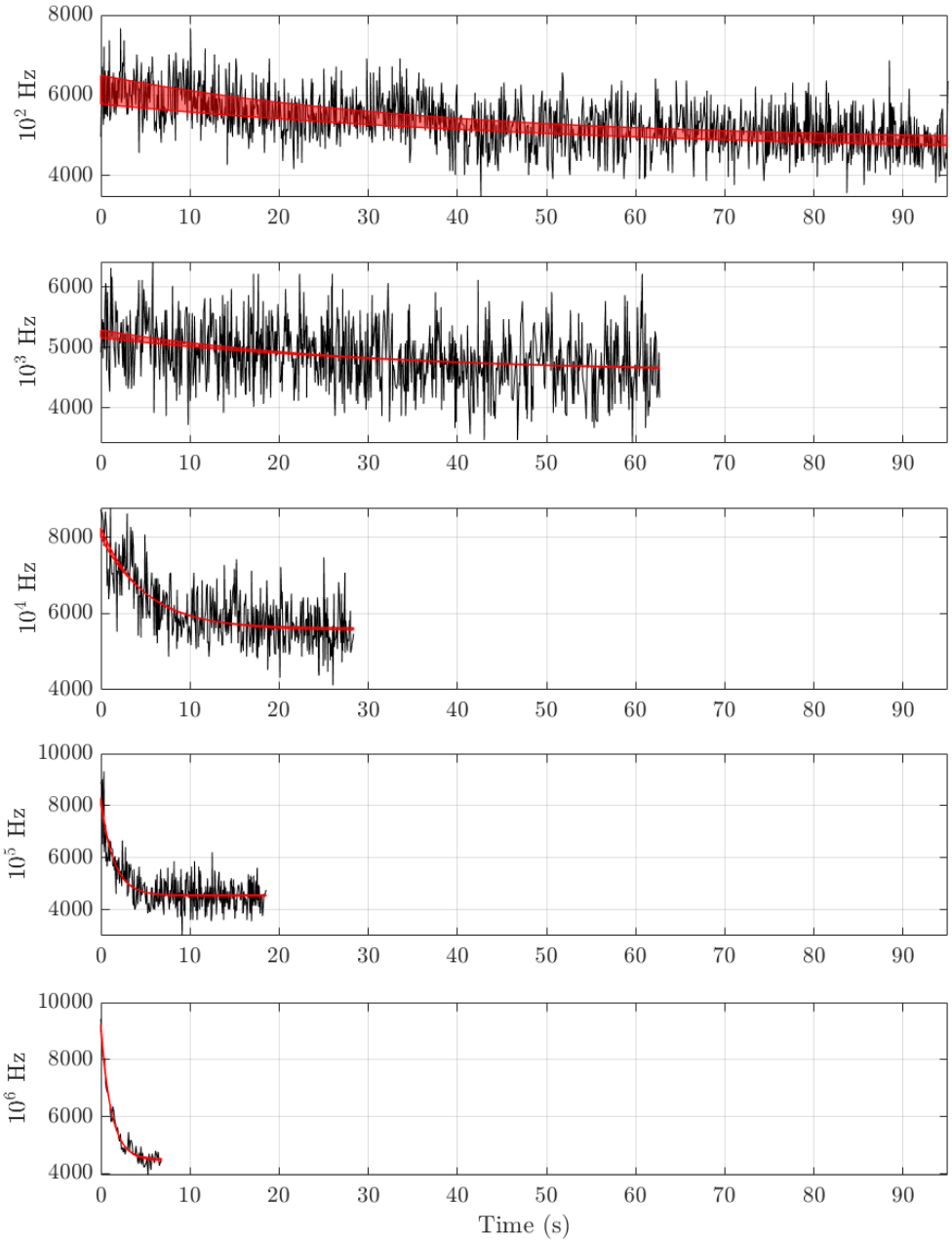

(a)

Figure 7.6: (a) Traces demonstrating the decay of the GR1 fluorescent signal under diffusion trains of different repetition rate, ranging from 100 Hz (top) to 1 MHz (bottom). The dashed red lines represent a fit to the exponential decay function $y = I_0 e^{-\gamma x} + I_{bkg}$.

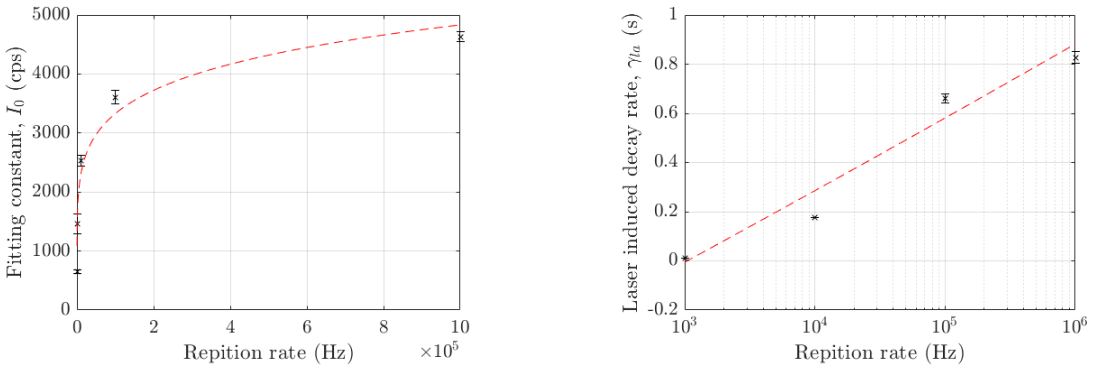

(a) **(b)**

Figure 7.7: The behaviour of the decay rate of the GR1 fluorescence signal under diffusion pulse trains prior to NV^- formation. Each decay is fit to the exponential decay function $y = I_0 e^{-(\gamma_{th}+\gamma_{la})x} + I_{bkg}$. Where the decay rate can can be seperated into thermal and laser induced components. Figures demonstrate the behavior of fitting constants I_0 and γ_{la} as a function of repetition rate in (a) and (b) respectively.

a 1 MHz diffusion train. This can be purely attributed to the timescales involved between the two regimes of laser writing. Transient peaks are caused by one diffusion pulse producing an arrangement of defects that allows the NV^- centre to fluoresce until some subsequent pulse destroys that arrangement. It is unlikely that a laser pulse induces a fluorescent arrangement which naturally decays into a non-fluorescent transition independently of subsequent laser pulses because of the reported phenomena of being able to achieve a stable NV^- signal if the diffusion train is terminated during one of these transient peaks.[39]

Under a 1 kHz diffusion pulse train the time in which this fluorescent state can exist is at least 1000 times greater than the time it can exist under a 1 MHz diffusion pulse train. Therefore, the lack of transient peaks can simply be attributed to the fact that the fluorescent arrangement emits far less light during its lifetime and cannot be resolved above the background by the detector. This presents a challenge to the fabrication process, since without the presence of transient peaks there is otherwise little indication of the efficacy of the diffusion process.

However, an alternative mechanism can be used to monitor the efficacy of the diffusion pulses. As mentioned, 532 nm light can be used to excite the single vacancy to produce the GR1 spectral feature. Under diffusion this signal decays as single vacancies annihilate with interstitial carbon atoms within the lattice. This vacancy decay can be seen as a function of repetition rate in figure 7.6. These decay patterns can be fit to a exponential decay model:

$$I(t) = I_0 e^{-\gamma t} + I_{bkg} \tag{7.1}$$

where $I(t)$ is the photon intensity at time t and I_0, γ and I_{bkg} are fitting constants. These fitting constants can be attributed physical meaning. I_{bkg} is the background fluorescence of the detector and therefore I_0 is the background subtracted counts from the GR1 at the beginning of the decay procedure. Finally γ is a decay rate.

In the ideal scenario where all the single vacancies are saturated by the confocal excitation laser one can make a prediction on the vacancy population from these decay curves, however this was not a possibility with the system used. This can clearly be demonstrated by the relationship between the fitting constant I_0 and the repetition rate, as shown in fig. 7.7a. The maximum intensity, I_0, is directly related to the number of vacancies at the start of the diffusion process and therefore should not be dependent on the diffusion train repetition rate. However, if the diffusion train is also fluorescently driving the vacancies, such as the case where the vacancy fluorescence is not saturated, then there would be relationship between the diffusion laser repetition rate and I_0.

Since the diffusion train is 520 nm it also induces fluorescence within the vacancies present after seeding, therefore as the repetition rate is increased there is a greater pumping of the fluorescent transitions within the vacancies and hence

a higher background subtracted amplitude from the vacancy ensemble. However this phenomenon would have no effect on the rate of decay of the fluorescence, which would scale linearly with the repitition rate.

This linear behaviour can be found by treating the extracted decay rates into two parts. Firstly the reduction in fluorescence due to the room temperature decay in the fluorescence due to the natural thermal motion of interstitials and a second term which is the decay rate induced by the diffusion laser pulse, which would be dependent on the repitition rate. Thus the decay rate γ can be split into thermal, γ_{th}, and laser induced, γ_{la}, terms:

$$\gamma = \gamma_{th} + \gamma_{la} \tag{7.2}$$

by assuming that the 100Hz diffusion decay rate is mostly thermal a linear relationship in the other decay rates can be found with respect to repition rate, as shown in fig. 7.7b. Finally the background counts, I_{bkg}, shows no correlation with the repetition rate of the diffusion laser.

Most importantly for the fabrication process, the onset of decay of the GR1 fluorescence is dependant on the pulse energy of the ultrafast fabrication laser. Typically, using a 520 nm diffusion train a diffusion pulse energy of 90% of the seed pulse energy is sufficient in order to induce the fluorescence decay. This is important since it allows for a measurable metric for diffusion. As the diffusion energy starts to approach the seed pulse energy there is an increasing risk of runaway graphitisation occuring at the focal spot. Being able to avoid this regime of fabrication by using the GR1 fluorescence as a monitor prevents graphitisation from occuring during fabrication.

7.3 Post fabrication analysis

An important metric in the fabrication of any NV^- centres is the quality of the NV^- centres created afterwards. Several methods of post fabrication can be used to determine the fabrication accuracy, spectroscopy and singularity of the NV^- centres created. Within, this section presents results from a 3x3 array of NV^- centres fabricated through the high repitition rate diffusion process. Some data presented within uses data from NV^- centres fabricated outside of this array in order to add to any statistical properties of the defects. Defects were fabricated with a 3 μm separation in x-y at a depth of 20 μm axially. Vacancies were fabricated using a seed pulse from the Yb:KYW laser (520 nm, 300 fs) with a pulse energy of 1.6 nJ. This was followed up by a 1 MHz pulse train of the same laser with a pulse energy of 1.2 nJ. Characterisation was performed using a confocal fluorescence microscope as outlined in Chapter 4.

7.3.1 Positioning accuracy

A key characterisation of NV^- fabrication techniques is the accuracy with which defects can be placed within a photonic device. This can be estimated by fabricating a small graphitic marker to act as a position reference for an NV^- centre array. In order to compensate for drift during the experiment, the fluorescence signal from the reference mark was used to re-centre the stages in between each array point. After fabrication, a 3-D image stack of the array can be collected and used as a comparison to the absolute stage movements. The ability for a microscope to accurately localise a single photon fixed dipole emitter is a non-trivial task,[182–186] but an estimate of error has been estimated from the fitting error.

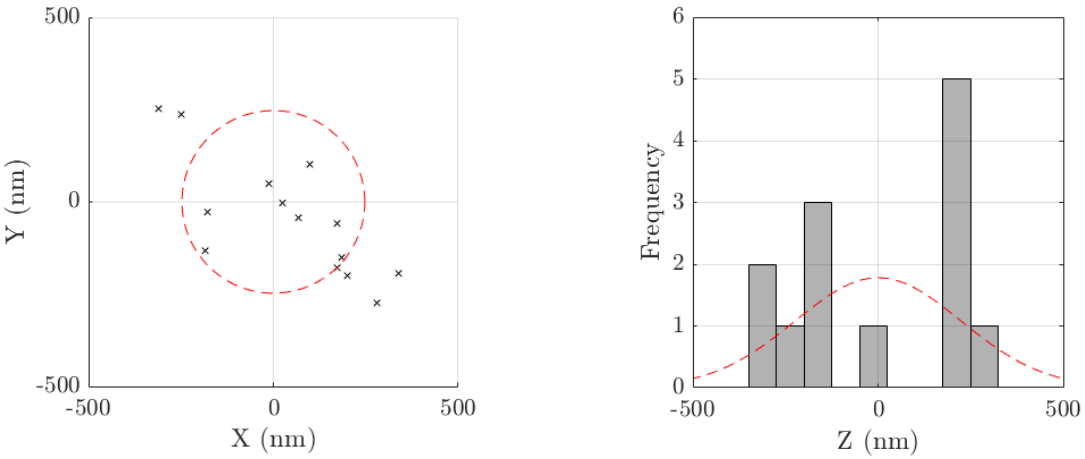

Figure 7.8: The (a) xy and (b) z positioning accuracy of NV^- fabricated through the deterministic laser writing process in high purity diamond. FHWM of these distributions give an xy positioning accuracy of 249±35 nm, and z positioning accuracy of 260±80 nm.

Fig. 7.8 demonstrates the xy and z fabrication precision. From these distributions the fabrication error can be estimated by fitting these errors to a gausian distribution, the FWHM of these distribution were determined to be 249±35 nm and 260±80 nm in xy and z respectively. This is significantly lower than the fabrication accuracy reported for 1 kHz diffusion in a 1.8 ppm diamond[39] and is infact more similar to that produced by thermally annealing laser written vacancies.[104] This suggests that the fabrication accuracy for NV^- centres produced by laser diffusion is limited to the nitrogen concentration of the sample, which would additionally explain why the fabrication accuracy is isotropic and has not adopted the same xy and z anisotropy as might be expected from an all optical process. Indeed, one can estimate the mean distance, $\langle r \rangle$, between substitutional nitrogen atoms as:

$$\langle r \rangle \sim \frac{1}{\sqrt[3]{n}} = 178\ nm \tag{7.3}$$

where n is the density of subsitutional nitrogen in nitrogen at 1 ppb concentration. This estimation for the mean separation of substitutional nitrogen atoms

demonstrates the same order of magnitude as the fabrication precision of the laser writing process.

Importantly this also provides feedback into the laser writing process, since the focal spot diameter of the confocal fluorescence microscope is $\approx$ 350 nm and only slightly larger than the fabrication accuracy. Therefore by underfilling the back aperture of the objective and opening the detection pinhole the NA of the confocal microscope can be reduced and sample a larger area around the fabrication laser. Thus, when an NV^- centre is formed far away from the centre of the confocal microscope spot it is still efficiently detected by the microscope.

Interestingly this provides some insight into the mechanism at to why vacancies are diffused. It was presumed in Chen *et al.*[104] that the increased fabrication accuracy was due to the same non-linear process being responsible for the vacancy diffusion of vacancies, however if that was true then defects would only be produced in the non-linear region, estimated to be $\approx$100 nm.[135] It is therefore more likely that the diffusion process is mediated by excited carriers or excitons, which have a much higher mobility within diamond. The length scales of diffusion of these particles are 53 μm[187] and 34 μm respectively,[188] which allows the vacancies to diffuse much further before meeting a substitutional nitrogen. The activation energy for vacancy diffusion is indeed less than the exciton energy, this hypothesis is however a subject of further research.

7.3.2 Defect singularity and yield

A key consideration of the ultrafast diffusion laser process is whether the technique is capable of creating single NV^- centres. Fig. 7.9a shows an image of the

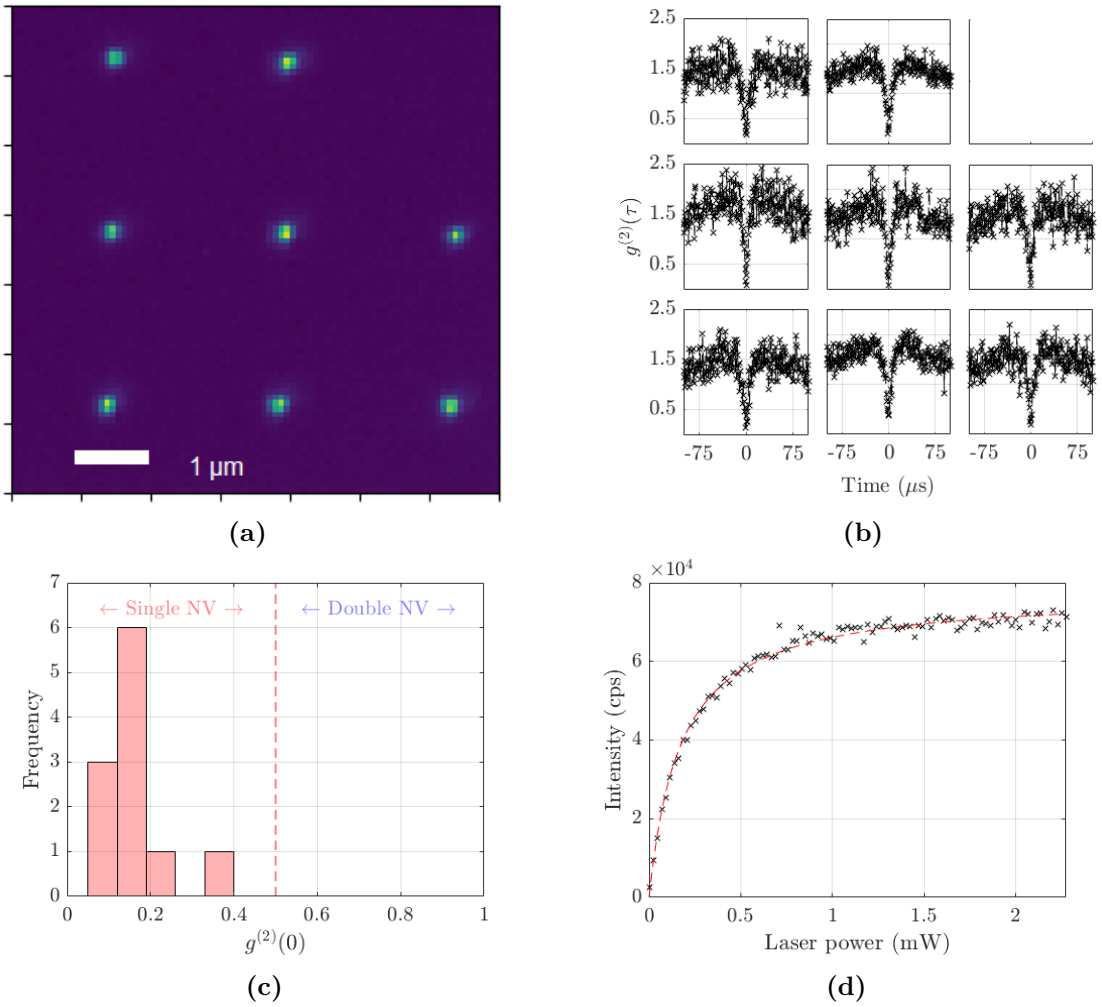

Figure 7.9: (a) Confocal fluorescence microscopy image of regular array of NV^- centres created by the ultrafast laser diffusion process in high purity diamond. (b) Corresponding photon correlation histograms of the array collected by HBT interferometer. (c) HBTs correlated into a histogram demonstrating that all fabricated defects are single NV^- centres. (d) A typical power saturation measurement for a single NV^- centre fabricated using the determinisitic ultrafast fabrication method in high purity diamond. This behaviour was fit to the function $I(P) = I_\infty \frac{P}{P+P_{sat}}$, where I_∞ and P_{sat} are fitting parameters.

fabricated regular array and each centres corresponding HBT signal in fig. 7.9b. This demonstrates that 8 of the fabricated emitters are single NV^- centres with $g^{(2)}(\tau) < 0.5$. It can be seen that the autocorrelation measurments exceeds 1 in these HBTs. This is partly due to photon bunching described in 3, this is also a result of signal-to-noise ratio effects and schemes do exist to remove their effect.**??** However, since all defects are clearly below the single defect limit these

corrections have not be applied.

One array site appears to have no fabricated emitters at all, suggesting that between fabrication and characterisation, that the defect has either switched charge state or has been destroyed by a nearby interstitial. One potential source of charge state instability is the prescence of nearby vacancy aggregates created during the seed or diffusion process. It is currently unknown if laser diffusion is capable of dissociating these aggregates, which have been thought to be successfully removed during thermal annealing.[104] One of the simplest of these structures, the divacancy, has been shown to be highly stable[189] and may act as a charge trap for the NV^- centre.

One method of probing the charge state stability is through power saturation measurements described in Chapter 4. Fig. 7.9d demonstrates a typical power saturation curve for a NV^- centre fabricated through this ultrafast method. From the good fit to eq. 4.1 demonstrated in this figure it can be seed that there is no charge state issues with the associated defect. However, one of the advantages of this technique is that fabrication is local, therefore processing could easily be repeated in order to restore the emitter to the fabrication site.

Furthermore this technique is capable of monitoring the creation of two NV centres within the same focal spot. As discussed earlier in the chapter, there is sufficient substitutional nitrogen within one focal spot for such an event to occur, however the creation of two NV centres simply requires additional diffusion time. Diffusing for longer periods does increases the chance of a interstitial recombining with an NV centre, because of this reason and to potentially inject additional vacancies into the focal spot, the seed pulse may need to be repeated. Figure 7.10

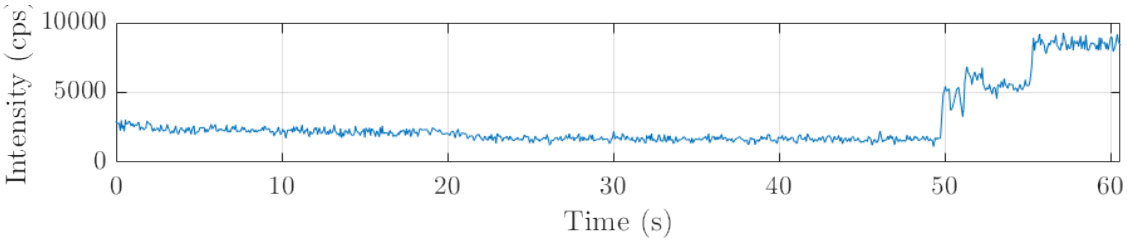

Figure 7.10: A typical detection trace demonstrating the formation of two NV^- centres within a single focal spot under ultrafast laser diffusion. The first NV^- centre is formed at 50 seconds, signalled by the jump in detected fluorescence. The second NV^- centre is formed 10 seconds later at the second jump in fluorescence.

demonstrates the fabrication of two NV centres within a single focal spot using this laser diffusion process. NV centres in such proximity are of scientific interest because they do not necessarily require photons to mediate their interactions and can instead directly interact via their spin, which is required for some quantum processes, such as transferring spin state.

7.4 Summary

In conclusion, this chapter has demonstrated the deterministic fabrication of NV^- centres in high purity, commerical grade diamond. Whilst this technique was initially proposed by Chen *et al.* the low purity and unique nature of the sample raised questions on how applicable the technique is to NV^- based quantum devices. Now that the technique has been demonstrated in high purity material, it represents a significant step forward in NV^- based quantum devices. The difficulty of achieving this regime of fabrication in high purity diamond is the necessity to use pulsed lasers that can achieve both accurate vacancy generation and high repetition rate diffusion. The engineering difficulties of this process have been outlined and discussed in Chapter 5.

It is important to note that the SPAD traces presented within this chapter do

not exhibit the frequency of transient peaks as shown within Chapter 6. The key difference between them is that due to the lower nitrogen concentration samples used in that chapter, a much higher repetition rate diffusion train, 1MHz instead of 1kHz, is required to produce NV^- centres within a reasonable time. A consequence of this is that the the effective time step in vacancy migration becomes 1 μs instead of 1 ms. Therefore if the transients are the result of the model presented within this chapter the NV^- centres would be permitted to emit within a much smaller time frame before their fluorescence is supressed again, which would lead to emission being below the noise on the detector. In principle, this could be probed using the Monte Carlo simulation presented in 6, however due to the increased complexity of the model (decreasing the time step by a factor of 1000) this could not be achieved within this thesis.

Furthermore, the experimental non-linearity of the transient peak frequency with respect to pulse energy, contained within Chapter 6, indicated an exciton mediated diffusion mechanism. This is further corroborated by the positioning accuracy presented within this chapter, which too suggests a longer range mechanism of diffusion than that involved in vacancy creation.

Additionally, this chapter has outlined that the experimental observables during laser diffusion can provide insight into the mechanics of defect creation and diffusion. One such observable is the decay of the GR1 signal as diffusion occurs. Vacancies are the only part of the NV centre that can move under the laser pulse and they can either annihilate with an interstitial or create an NV centre. The decays are evidence that the vacancies are being annihilated, and since it shown that NV centres are being created there is no reason to think those the vacancies are not migrating. A cross correlation between NV and V emission is not possible since

typically only a single vacancy becomes a NV, however this might be possible at very high nitrogen containing diamond.

Using laser writing observables to inform simulations was first introduced in Chapter 6, which showed how transient peaks in the diffusion trace can be replicated in simulations. This demonstrates the power of this technique, which provides an optical window into the diffusion and defect creation process and is likely a fruitful area of further research.

Finally, it is important to mention that these defects must be further characterised to assess their efficacy in a quantum device. Important charactersitic such as T_2 times and photoluminescence lifetime measurements are key in determining how the technique can be modified in order to determinsitically create long life time emitters.

Chapter 8

Conclusions and outlook

8.1 Conclusion

This thesis has demonstrated the determinsitic fabrication of NV^- centres in high purity, commerically available diamond through the used of ultrafast laser fabrication. In Chapter 5 the process and engineering challenges in building an optical system capable of this fabrication is broken down. In order to achieve the high degree of accuracy required for vacancy fabrication, the use of high NA optics, ultrafast pulses, fine pulse energy control and aberration correction was used.

Additionally, this system is capable of high repetition rate diffusion, which is necessary in order to speed up the rate of vacancy diffusion in high purity material. This is coupled with an *in situ* beamscanning confocal fluorescence microscope in order to detect NV^- centre creation and terminate the diffusion process. It has been shown that the use of the high repetition rate laser produces significant background noise on the microscope detector due to plasma generated at the focal spot, this however can be filtered by appropriately time-filtering the detector. This sytem is particularly powerful in its ability to provide independent lateral and axial

control of both the fabrication laser and confocal microscope through the use of beam-scanning mirrors and remote focusing techniques using an SLM.

In Chapter 6, various experimental observables under ultrafast laser fabrication have been analysed. Transient peaks previously reported at low repetition rates may provide a observable window into the process of diffusion under the focal spot. Using a DFT based theoretical study, various defect interactions between the NV^- centre and the carbon self-interstitial where investigated. It was discovered that hybridisation can occur between the π-bonds of the carbon self-interstitial and the e-manifold of the NV^- centre. Importantly, this e-manifold is directly involved in the excited state fluorescence transition of the defect and hybridisation of this manifold might be responsible for the supression of the NV^- centres fluorescence during diffusion.

It was proposed that under migration, the action of interstitials leaving and entering states of hybridisation with the NV^- centre results in the transient peaks seen experimentally. And indeed, by the using the DFT simulation as a basis for a random walk model of intersitial migration the same transient peak patterns can be replicated in simulation. Additionally, the behaviour of these transients follows similarly to behaviours seen experimentally.

Finally Chapter 7 presented the first deterministic fabrication of single NV^- centres in high purity, commerically available diamond. The fabrication process did not demonstrate the same transient peaks observed at lower repetition rates in low purity diamond however an additional feedback mechanism using the GR1 fluorescence signal from the single vacancy can be used to determine the efficacy of diffusion. This decay rate was analysed at different repetition rates.

A fabricated array of NV^- centres were analysed and confirmed to be single emitters in every fabrication attempt. Additonally, the fabrication accuracy was analysed and it was found that the accuracy of the technique was limited to the nitrogen concentration within diamond. This suggests that the highly non-linear mechanism responsible for vacancy creation was not responsible for diffusion and various mechanisms for vacancy migration were proposed. This work represents a signifcant step forward in NV^- based photonic devices, which are now no longer limited by the low yield of thermal techniques.

8.2 Future prospects

The most obvious aspect missing from this analysis is coherence measurements of the fabricated NV^- centres. Due to the COVID-19 pandemic, which prevented research for a significant portion of this project some key data has not been taken. Premier amongst these are the coherence properties of the fabricated defects. Depending on the results of this analysis, further improvements to the mechanism can be employed in order to potentially increase the coherence times. A potentially major limiting factor is nearby interstitials interacting with the defect, therefore further laser diffusion or potentially thermal annealing could be employed to diffuse these interstitials away from the NV^- centre.

Futhermore, it is thought that laser fabrication can create vacancy aggregates and it is unknown if those aggregates are still present after diffusion. These aggregates would served to both slower the coherence times of any fabricated defect and act as a recombination site for carriers generated during diffusion. Further work can

be performed in ideally identifiying a fabrication regime which does not lead to the generation of significant vacancy aggregates.

This process also demands demonstration in various photonic devices. This fabrication process opens the door to potentially directly placing NV^- centres within photonic microstructures such as solid immersion lenses. Many of these techniques are destructive and the benefit of being able to fabricate defects directly into microstructures will help avoid cases where the microstructure fabrication quenches target emitters. Additionally, the all-optical laser fabrication process is simple to allign with such microstructures.

The novel ultrafast laser fabrication system described in Chapter 5 is unique in not only its ability to create defects in high purity diamond. It is also the first multiwavelength ultrafast fabrication system capable of fabricating defects using three wavelengths. Whilst some theoretical studies have been produced about the fabrication of defects at different wavelengths there has been no experimental study on the differences between the fabrication regimes. It is possible that studying the wavelength, and therefore the non-linear processes within, would lead to a further understand of the theory of ultrafast laser writing and to the creation of higher performance defects for photonic applications.

This thesis also touched on various ways in which the observables in ultrafast laser fabrication can be used to analyse both defect creation and migration mechanisms. Laser fabrication offers a unique optical window into both processes and further developments in the theoretical study presented in Chapter 6 could further elucidate those mechanisms.

One obvious direction is to use time dependent DFT techniques to directly address the excited state fluorescent transition during hybridisation. Additonally the behaviour of the fluorescence orbitals during defect migration, through the use of molecular dynamics DFT simulations, could provide further information on how the transient peaks occur during fabrication. Furthermore, the Monte-Carlo simulation presented in Chapter 6 could be expanded to include specific mechanisms involved in defect migration, or potentially extended to higher repetition rate fabrication regimes.

Finally whilst the techniques presented within this thesis are very much focused on using diamond NV^- centres as a medium, there is no strict exclusion to other defect centres or indeed materials. Expanding this laser writing regime into new colour centres in different materials may provide further fruitful advances in quantum technology. Additionally, the optical probe during defect formation and migration can be used to discover more about how defects these form within the solid state. Such a technique could even be used to probe the library of currently unknown fluorescent defects in natural diamonds in order to help identify them. This is just the beginning.

Appendices

Appendix A

Monte Carlo simulation

Within it is assumed that a defect is permitted to perform a single step per pulse from the diffusion laser, this essentially discretises the walk into 1 ms steps under a 1 kHz diffusion train. In a discrete random walk on the diamond crystal structure evolves the position of a walker as follows:

$$\boldsymbol{X}_{N+1} = \boldsymbol{X}_N + (-1)^N \boldsymbol{d}_i \tag{A.1}$$

where $\boldsymbol{X}_n$ is the position of a walker after N steps and $\boldsymbol{d}_i$ is one of the diamond bond directions which are the set of directions tetrahedrally symmetric (T_d) to $\left[\bar{1} \quad \bar{1} \quad \bar{1}\right]$:

$$\boldsymbol{D} = \begin{bmatrix} \boldsymbol{d}_1 \\ \boldsymbol{d}_2 \\ \boldsymbol{d}_3 \\ \boldsymbol{d}_4 \end{bmatrix} = \begin{bmatrix} \bar{1} & \bar{1} & \bar{1} \\ \bar{1} & 1 & 1 \\ 1 & \bar{1} & 1 \\ 1 & 1 & \bar{1} \end{bmatrix} \tag{A.2}$$

where the probability of walking in any of these directions are equal.

By assuming the hopping opportunities have the same frequency as the repetition rate than the time step of the walk can be directly calculated. Within this thesis, unless otherwise stated, the time step is 1 ms for a 1 kHz diffusion train. The random number generator used during the random walk is based on the Mersenne Twister general-purpose pseudorandom number.[190] This is implemented

by creating a binary probability vector P and randomly distributing a single unity value to its elements:

$$\boldsymbol{P} = \begin{bmatrix} P_1 & P_2 & P_3 & P_4 \end{bmatrix} \tag{A.3}$$

where P_i is the probability of a walker moving along direction i described by matrix $\boldsymbol{D}$. This allows the position of a walker to be calculated as:

$$\boldsymbol{X}_{N+1} = \boldsymbol{X}_N + (-1)^N \boldsymbol{P} \cdot \boldsymbol{D} \tag{A.4}$$

The probability of hopping is determined by the distribution:

$$P(\alpha) = 1 - e^{-\alpha / E_b} \tag{A.5}$$

where E_b is the energy barrier to hopping. As discussed in Chapter 6, the energy barrier for vacancy and carbon self-interstitial migration is 2.3 eV and 1.6 eV respectively. Additionally, the energy barrier for a site swapping of an NV^- centre is 4 eV.

The simulation is initialised with a random distrobution of 1.8 ppm substiutional nitrogen. Griffiths *et al.* estimated the concentration of Frenkel pair fabrication after the seed pulse is in the range of 100 to 500 ppm. Within the simulation a Frenkel concentration of 300 ppm is used in order to optimise compute time. Within the simulation if an interstitial becomes a near neighbour of any vacancy or NV^- centre both defects are destroyed.

The goal of the simulation is to generate fluorescence traces and test if they replicate the spiking phenomena shown in the experimental fluorescence traces. The emission characteristics from an NV^- centre is simulated by a simple flag based system. For any given time step, if an interstitial meets the requirements for

hybridisation proposed in fig. 6.5 then the emission flag is set to 0, otherwise it is set to 1. In order to quickly determine if any carbon self-interstitial j falls within the criteria of hybridisation the critera has been broken down into three conditions, firstly the code checks the displacement, Δx, between the interstitial and NV^- centre:

$$\Delta x = ||\boldsymbol{X}_j - \boldsymbol{X}_N|| \tag{A.6}$$

where $\boldsymbol{X}_j$ is the position of interstitial j, $\boldsymbol{X}_N$ is the position of the nitrogen atom. The interstitial is considered hybridised if $\Delta x \leq 4$Å. If 4Å$< \Delta x \leq 15$Å then a second condition is checked to determine if the interstitial falls within the cone described in fig 6.5. This condition uses the dot product to calculate the V-N-I_C angle, which is checked against the angle of the cone:

$$\frac{(\boldsymbol{X}_j - \boldsymbol{X}_N) \cdot (\boldsymbol{X}_V - \boldsymbol{X}_N)}{||\boldsymbol{X}_j - \boldsymbol{X}_N||||\boldsymbol{X}_V - \boldsymbol{X}_N||} > 0.5 \tag{A.7}$$

where $\boldsymbol{X}_V$ is the position of the vacancy. This provides a fast method of checking the hybridisation critera which is checked serveral times per step of the random walk. This binary emission flag is then processed using a rolling average in order to represent the SPAD acquisition time present experimentally. Unless otherwise stated this window is 20 ms.

Appendix B

Heat equation simulations in diamond

One of the potentially more obvious methods for diffusion is to consider the possibility of a thermal diffusion induced by elevated lattice temperature when the plasma relaxes. Griffiths *et al.* reports that during Frenkel defect creation the lattice temperature within the focal spot can rise to $\approx$ 1300 K,[135] which is certainly high enough to thermally activate carbon self-interstitials and vacancies.[191] Moreover, regimes of cumulative heating during irradiation under a pulsed laser has been reported in glasses,[192] where heat build up between pulses eventually thermalises in a direct comparison to thermal annealing.

This possibility can be explored by solving the heat equation:

$$\frac{\partial T}{\partial t} = \frac{k}{\rho c_p}\Big[\frac{\partial^2 T}{\partial x^2} + \frac{\partial^2 T}{\partial y^2} + \frac{\partial^2 T}{\partial z^2}\Big] \tag{B.1}$$

where k is the thermal conductivity of diamond, ρ is the density of diamond and c_p is the specific heat capacity of diamond. Within the maximum temperature of the focal spot is overestimated by using the peak lattice temperature during Frenkel defect formation found in the study from Griffiths *et al.* the distribution of temperature is assumed to be gaussian with a FWHM equal to the non-linear

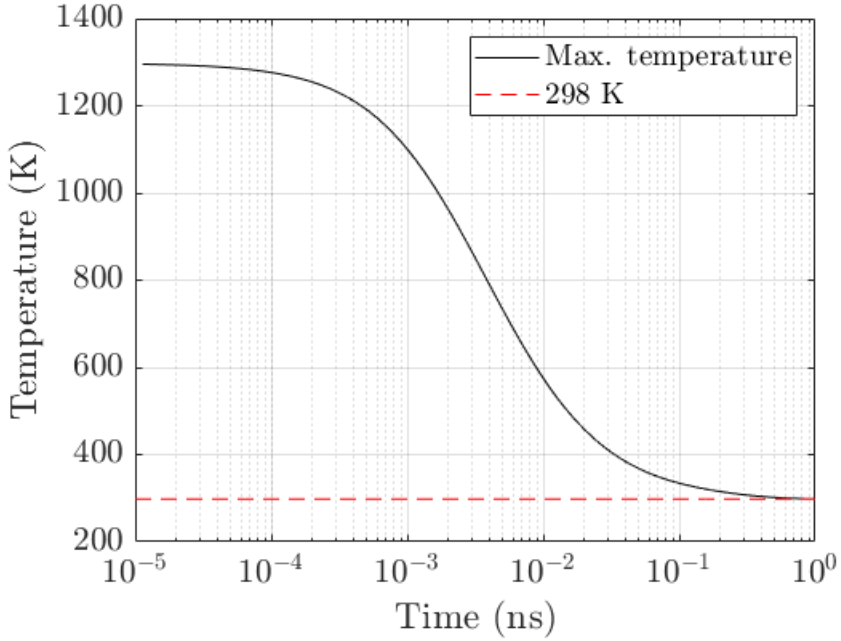

Figure B.1: The evolution of the maximum temperature of a focal spot in diamond after an ultrafast laser pulse, as predicted by the heat equation.

region described by Griffiths *et al.*[135] Since diamond is an electrical insulator the majority of heat conduction at room temperature is phonon mediated, therefore the speed of sound within diamond is used to ensure the simulation's Courant number is < 0.7.[193] The total simulated volume was $10\times$ the focal volume with the boundaries acting as a 298 K heat sink.

Figure B.1 shows the evolution of the maximum temperature of the focal spot over time. From this it is clear to see that the temperature generated from a laser pulse is almost entirely lost over the course of 1 ns and therefore cumulative heating is not possible in diamond without a laser repetition rate of ≥ 1 GHz. This is due to diamond large thermal conductivity of 2000 $\mathrm{Wm^{-1}K^{-1}}$, which is five times higher than that of copper. This does not exclude the possiblity that defects are able to migrate during the brief window of elevated lattice temperature.

References

[1] B. Hensen et al. “Loophole-free Bell inequality violation using electron spins separated by 1.3 kilometres”. In: *Nature* 526 (2015), 682—686.

[2] I. Aharonovich and E. Neu. “Diamond Nanophotonics”. In: *Advanced Optical Materials* 2 (2014), 911—928.

[3] L. Childress and R. Hanson. “Diamond NV centers for quantum computing and quantum networks”. In: *MRS Bulletin* 38.2 (2013), pp. 134–138.

[4] T. M. Babinec et al. “A diamond nanowire single-photon source”. In: *Nature Nanotechnology* 5 (2010), pp. 195–199.

[5] Y. Tao et al. “Single-Crystal Diamond Nanomechanical Resonators with Quality Factors Exceeding One Million”. In: *Nature Communications* 5 (2014), p. 3638.

[6] E. R. MacQuarrie et al. “Cooling a Mechanical Resonator with Nitrogen-Vacancy Centres Using a Room Temperature Excited State Spin–Strain Interaction”. In: *Nature Communications* 8 (2017), p. 14358.

[7] A. Sipahigil et al. “An Integrated Diamond Nanophotonics Platform for Quantum-Optical Networks”. In: *Science* 354 (2016), pp. 847–850.

[8] B. J. M. Hausmann et al. “Integrated High-Quality Factor Optical Resonators in Diamond”. In: *Nano Letters* 13 (2013), p. 1898.

[9] J. Bochmann et al. “Nanomechanical Coupling between Microwave and Optical Photons”. In: *Nature Physics* 9 (2013), pp. 712–716.

[10] M. Jamali et al. “Microscopic diamond solid-immersion-lenses fabricated around single defect centers by focused ion beam milling”. In: *Review of Scientific Intstruments* 85 (2014), p. 123703.

[11] A. Beveratos et al. “Room temperature stable single-photon source”. In: *The European Physical Journal D - Atomic, Molecular, Optical and Plasma Physics* 18 (2002), pp. 191–196.

[12] E. Hecht. *Optics*. 4th ed. Reading, Mass: Addison-Wesley, 2002.

[13] C. Kittel. *Introduction to Solid State Physics*. Wiley, 2004.

[14] J Walker. “Optical absorption and luminescence in diamond”. In: *Reports on Progress in Physics* 42.10 (1979), pp. 1605–1659.

[15] G. Balasubramanian et al. “Ultralong spin coherence time in isotopically engineered diamond”. In: *Nature Materials* 8.5 (2009), pp. 383–387.

[16] I Aharonovich et al. “Diamond-based single-photon emitters”. In: *Reports on Progress in Physics* 74.7 (2011), p. 076501.

[17] A. M. Zaitsev. “Vibronic spectra of impurity-related optical centers in diamond”. In: *Physical Review B* 61.19 (2000), pp. 12909–12922.

[18] C. D. Clark et al. “The absorption spectra of natural and irradiated diamonds”. In: *Proceedings of the Royal Society of London. Series A. Mathematical and Physical Sciences* 234.1198 (1956), pp. 363–381.

[19] R. A. Dugdale. “The colouring of diamonds by neutron and electron bombardment”. In: *British Journal of Applied Physics* 4.11 (1953), pp. 334–337.

[20] C. A. Coulson and M. J. Kearsley. “Colour centres in irradiated diamonds. I”. In: *Proceedings of the Royal Society of London. Series A. Mathematical and Physical Sciences* 241.1227 (1957), pp. 433–454.

[21] C. D. Clark, J. Walker, and R. W. Ditchburn. “The neutral vacancy in diamond”. In: *Proceedings of the Royal Society of London. A. Mathematical and Physical Sciences* 334.1597 (1973), pp. 241–257.

[22] C. D. Clark and C. A. Norris. “Photoluminescence associated with the 1.673, 1.944 and 2.498 eV centres in diamond”. In: *Journal of Physics C: Solid State Physics* 4.14 (1971), pp. 2223–2229.

[23] G. Davies. “Charge states of the vacancy in diamond”. In: *Nature* 269.5628 (1977), pp. 498–500.

[24] T. Bilodeau et al. “Calorimetric absorption spectroscopy and photoluminescence study of defects in diamond”. In: *Diamond and Related Materials* 2 (1993), pp. 699–703.

[25] Du Preez L. “Electron paramagnetic resonance and optical investigations of defect centres in diamond”. PhD thesis. Place of publication not identified: [publisher not identified], 1965.

[26] G. Davies and M. F. Hamer. “Optical studies of the 1.945 eV vibronic band in diamond”. In: *Philosophical Transactions of the Royal Society A* 348 (1976), pp. 285–298.

[27] J. H. N. Loubser and J. A. v. Wyk. “Electron spin resonance in the study of diamond”. In: *Reports on Progress in Physics* 41.8 (1978), pp. 1201–1248.

[28] A. Lenef and S. C. Rand. “Electronic structure of the N-V center in diamond: Theory”. In: *Physical Review B* 53.20 (1996), pp. 13441–13455.

[29] J. P. Goss et al. “Comment on “Electronic structure of the N-V center in diamond: Theory””. In: *Physical Review B* 56.24 (1997), pp. 16031–16032.

[30] Y. Mita. “Change of absorption spectra in type-Ib diamond with heavy neutron irradiation”. In: *Physical Review B* 53.17 (1996), pp. 11360–11364.

[31] M. W. Doherty et al. “The nitrogen-vacancy colour centre in diamond”. In: *Physics Reports*. The nitrogen-vacancy colour centre in diamond 528.1 (2013), pp. 1–45.

[32] E. v. Oort, N. B. Manson, and M. Glasbeek. “Optically detected spin coherence of the diamond N-V centre in its triplet ground state”. In: *Journal of Physics C: Solid State Physics* 21.23 (1988), pp. 4385–4391.

[33] A. Gali, M. Fyta, and E. Kaxiras. “Ab initio supercell calculations on nitrogen-vacancy center in diamond: Electronic structure and hyperfine tensors”. In: *Physical Review B* 77.15 (2008), p. 155206.

[34] N. B. Manson and R. L. McMurtrie. “Issues concerning the nitrogen-vacancy center in diamond”. In: *Journal of Luminescence*. Proceedings of the Ninth International Meeting on Hole Burning, Single Molecule, and Related Spectroscopies: Science and Applications 127.1 (2007), pp. 98–103.

[35] L. J. Rogers et al. “Infrared emission of the NV centre in diamond: Zeeman and uniaxial stress studies”. In: *New Journal of Physics* 10.10 (2008), p. 103024.

[36] C. A. Ryan, J. S. Hodges, and D. G. Cory. “Robust Decoupling Techniques to Extend Quantum Coherence in Diamond”. In: *Physical Review Letters* 105.20 (2010), p. 200402.

[37] F. F. de Oliveira et al. “Effect of Low-Damage Inductively Coupled Plasma on Shallow NV Centers in Diamond”. In: *Applied Physics Letters* 107.7 (2015), p. 073107.

[38] J. Wang et al. “Coherence times of precise depth controlled NV centers in diamond”. In: *Nanoscale* 8.10 (2016), pp. 5780–5785.

[39] Y.-C. Chen et al. “Laser writing of individual nitrogen-vacancy defects in diamond with near-unity yield”. In: *Optica* 6.5 (2019), p. 662.

[40] T. Yamamoto et al. “Extending spin coherence times of diamond qubits by high-temperature annealing”. In: *Physical Review B* 88.7 (2013), p. 075206.

[41] S. Johnson et al. “Tunable cavity coupling of the zero phonon line of a nitrogen-vacancy defect in diamond”. In: *New Journal of Physics* 17.12 (2015), p. 122003.

[42] A. Faraon et al. “Coupling of Nitrogen-Vacancy Centers to Photonic Crystal Cavities in Monocrystalline Diamond”. In: *Physical Review Letters* 109.3 (2012), p. 033604.

[43] A. M. Edmonds et al. “Electron paramagnetic resonance studies of silicon-related defects in diamond”. In: *Physical Review B* 77.24 (2008), p. 245205.

[44] E. Neu et al. “Single photon emission from silicon-vacancy colour centres in chemical vapour deposition nano-diamonds on iridium”. In: *New Journal of Physics* 13.2 (2011), p. 025012.

[45] L. J. Rogers et al. “Multiple intrinsically identical single-photon emitters in the solid state”. In: *Nature Communications* 5.1 (2014), p. 4739.

[46] A. Sipahigil et al. “Indistinguishable Photons from Separated Silicon-Vacancy Centers in Diamond”. In: *Physical Review Letters* 113.11 (2014), p. 113602.

[47] R. E. Evans et al. “Narrow-Linewidth Homogeneous Optical Emitters in Diamond Nanostructures via Silicon Ion Implantation”. In: *Physical Review Applied* 5.4 (2016), p. 044010.

[48] B. Pingault et al. “Coherent control of the silicon-vacancy spin in diamond”. In: *Nature Communications* 8.1 (2017), p. 15579.

[49] J. N. Becker et al. “Ultrafast all-optical coherent control of single silicon vacancy colour centres in diamond”. In: *Nature Communications* 7.1 (2016), p. 13512.

[50] K. D. Jahnke et al. “Electron–phonon processes of the silicon-vacancy centre in diamond”. In: *New Journal of Physics* 17.4 (2015), p. 043011.

[51] B. Pingault et al. “All-Optical Formation of Coherent Dark States of Silicon-Vacancy Spins in Diamond”. In: *Physical Review Letters* 113.26 (2014), p. 263601.

[52] L. J. Rogers et al. “All-Optical Initialization, Readout, and Coherent Preparation of Single Silicon-Vacancy Spins in Diamond”. In: *Physical Review Letters* 113.26 (2014), p. 263602.

[53] D. Sukachev et al. “Silicon-Vacancy Spin Qubit in Diamond: A Quantum Memory Exceeding 10 ms with Single-Shot State Readout”. In: *Physical Review Letters* 119.22 (2017), p. 223602.

[54] K. D. Jahnke et al. “Electron–phonon processes of the silicon-vacancy centre in diamond”. In: *New Journal of Physics* 17.4 (2015), p. 043011.

[55] L. J. Rogers et al. “All-optical initialization, readout, and coherent preparation of single silicon-vacancy spins in diamond”. In: *Physical review letters* 113.26 (2014), p. 263602.

[56] B. Pingault et al. “All-optical formation of coherent dark states of silicon-vacancy spins in diamond”. In: *Physical review letters* 113.26 (2014), p. 263601.

[57] B. Green et al. “Neutral Silicon-Vacancy Center in Diamond: Spin Polarization and Lifetimes”. In: *Physical Review Letters* 119.9 (2017), p. 096402.

[58] S. Dhomkar et al. “On-Demand Generation of Neutral and Negatively Charged Silicon-Vacancy Centers in Diamond”. In: *Physical Review Letters* 120.11 (2018), p. 117401.

[59] B. C. Rose et al. “Observation of an environmentally insensitive solid-state spin defect in diamond”. In: *Science* 361.6397 (2018), pp. 60–63.

[60] J. Görlitz et al. “Coherence of a charge stabilised tin-vacancy spin in diamond”. In: *npj Quantum Information* 8 (2022), pp. 1–9.

[61] G. Thiering and A. Gali. “Magneto-optical spectra of the split nickel-vacancy defect in diamond”. In: *Physical Review Research* 3 (2021), p. 043052.

[62] M. Vollmer, K.-P. Möllmann, and J. A. Shaw. “The optics and physics of near infrared imaging”. In: *Education and Training in Optics and Photonics*. Optica Publishing Group. 2015, TPE09.

[63] J. R. Hannay and G. G. Stokes. “VI. On the artificial formation of the diamond”. In: *Proceedings of the Royal Society of London* 30.200-205 (1880), pp. 450–461.

[64] S. Koizumi, M. Suzuki, and J. Pernot. “n-Type Doping of Diamond”. In: *Physics and Applications of CVD Diamond*. John Wiley & Sons, Ltd, 2008, pp. 237–256.

[65] A. Stacey et al. “Controlled synthesis of high quality micro/nano-diamonds by microwave plasma chemical vapor deposition”. In: *Diamond and Related Materials* 18.1 (2009), pp. 51–55.

[66] J. C. Angus, H. A. Will, and W. S. Stanko. “Growth of Diamond Seed Crystals by Vapor Deposition”. In: *Journal of Applied Physics* 39.6 (1968), pp. 2915–2922.

[67] A. Argoitia, C. S. Kovach, and J. C. Angus. “Hot-Filament CVD Methods”. In: *Handbook of Industrial Diamonds and Diamond Films*. CRC Press, 1998.

[68] J. E. Butler et al. “Understanding the chemical vapor deposition of diamond: recent progress”. In: *Journal of Physics: Condensed Matter* 21.36 (2009), p. 364201.

[69] P. K. Bachmann. “Microwave Plasma Chemical Vapor Deposition of Diamond”. In: *Handbook of Industrial Diamonds and Diamond Films*. CRC Press, 1998.

[70] I. Aharonovich et al. “Formation of color centers in nanodiamonds by plasma assisted diffusion of impurities from the growth substrate”. In: *Applied Physics Letters* 93.24 (2008), p. 243112.

[71] I. Aharonovich et al. “Enhanced single-photon emission in the near infrared from a diamond color center”. In: *Physical Review B* 79.23 (2009), p. 235316.

[72] J. Michl et al. “Perfect alignment and preferential orientation of nitrogen-vacancy centers during chemical vapor deposition diamond growth on (111) surfaces”. In: *Applied Physics Letters* 104.10 (2014), p. 102407.

[73] M. Lesik et al. “Perfect preferential orientation of nitrogen-vacancy defects in a synthetic diamond sample”. In: *Applied Physics Letters* 104.11 (2014), p. 113107.

[74] H. Ozawa et al. “Formation of perfectly aligned nitrogen-vacancy-center ensembles in chemical-vapor-deposition-grown diamond (111)”. In: *Applied Physics Express* 10.4 (2017), p. 045501.

[75] C. Osterkamp et al. “Engineering preferentially-aligned nitrogen-vacancy centre ensembles in CVD grown diamond”. In: *Scientific Reports* 9.1 (2019), p. 5786.

[76] A. M. Edmonds et al. “Production of oriented nitrogen-vacancy color centers in synthetic diamond”. In: *Physical Review B* 86.3 (2012), p. 035201.

[77] M. W. Doherty et al. “Measuring the defect structure orientation of a single NV-centre in diamond”. In: *New Journal of Physics* 16.6 (2014), p. 063067.

[78] J. R. Rabeau et al. “Fabrication of single nickel-nitrogen defects in diamond by chemical vapor deposition”. In: *Applied Physics Letters* 86.13 (2005), p. 131926.

[79] J. O. Orwa et al. “Raman investigation of damage caused by deep ion implantation in diamond”. In: *Physical Review B* 62.9 (2000), pp. 5461–5472.

[80] J. Meijer et al. “Generation of single color centers by focused nitrogen implantation”. In: *Applied Physics Letters* 87.26 (2005), p. 261909.

[81] J. R. Rabeau et al. “Implantation of labelled single nitrogen vacancy centers in diamond using N15”. In: *Applied Physics Letters* 88.2 (2006), p. 023113.

[82] M. Lesik et al. “Maskless and targeted creation of arrays of colour centres in diamond using focused ion beam technology”. In: *Physica Status Solidi A* 210.10 (2013), pp. 2055–2059.

[83] S. Pezzagna et al. “Nanoscale Engineering and Optical Addressing of Single Spins in Diamond”. In: *Small* 6.19 (2010), pp. 2117–2121.

[84] D. M. Toyli et al. “Chip-Scale Nanofabrication of Single Spins and Spin Arrays in Diamond”. In: *Nano Letters* 10.8 (2010), pp. 3168–3172.

[85] P Spinicelli et al. “Engineered arrays of nitrogen-vacancy color centers in diamond based on implantation of CN $^-$ molecules through nanoapertures”. In: *New Journal of Physics* 13.2 (2011), p. 025014.

[86] S. Sangtawesin et al. “Highly tunable formation of nitrogen-vacancy centers via ion implantation”. In: *Applied Physics Letters* 105.6 (2014), p. 063107.

[87] S. Pezzagna et al. “Creation of colour centres in diamond by collimated ion-implantation through nano-channels in mica”. In: *Physica Status Solidi A* 208.9 (2011), pp. 2017–2022.

[88] S Becker et al. “Nitrogen implantation with a scanning electron microscope”. In: *Scientific reports* 8.1 (2018), pp. 1–6.

[89] J. Schwartz et al. “In situoptimization of co-implantation and substrate temperature conditions for nitrogen-vacancy center formation in single-crystal diamonds”. In: *New Journal of Physics* 13.3 (2011), p. 035022.

[90] Z. Huang et al. “Diamond nitrogen-vacancy centers created by scanning focused helium ion beam and annealing”. In: *Applied Physics Letters* 103.8 (2013), p. 081906.

[91] K. Ohno et al. “Three-dimensional localization of spins in diamond using 12C implantation”. In: *Applied Physics Letters* 105.5 (2014), p. 052406.

[92] S. B. van Dam et al. “Optical coherence of diamond nitrogen-vacancy centers formed by ion implantation and annealing”. In: *Physical Review B* 99.16 (2019), p. 161203.

[93] V. M. Acosta et al. “Diamonds with a high density of nitrogen-vacancy centers for magnetometry applications”. In: *Physical Review B* 80.11 (2009), p. 115202.

[94] E. Kim et al. “Electron spin resonance shift and linewidth broadening of nitrogen-vacancy centers in diamond as a function of electron irradiation dose”. In: *Applied Physics Letters* 101.8 (2012), p. 082410.

[95] K. Ohno et al. “Engineering shallow spins in diamond with nitrogen delta-doping”. In: *Applied Physics Letters* 101.8 (2012), p. 082413.

[96] C. A. McLellan et al. “Patterned Formation of Highly Coherent Nitrogen-Vacancy Centers Using a Focused Electron Irradiation Technique”. In: *Nano Letters* 16.4 (2016), pp. 2450–2454.

[97] J. A. v. Wyk et al. “The dependences of ESR line widths and spin - spin relaxation times of single nitrogen defects on the concentration of nitrogen defects in diamond”. In: *Journal of Physics D: Applied Physics* 30.12 (1997), pp. 1790–1793.

[98] M. J. Beesley. *Lasers and their applications*. London: Taylor & Francis, 1972.

[99] J. C. Ion. “Chapter 1 - Introduction”. In: *Laser Processing of Engineering Materials*. Ed. by J. C. Ion. Oxford: Butterworth-Heinemann, 2005, pp. 1–11.

[100] W. M. Steen and J. Mazumder. *Laser Material Processing*. Springer Science & Business Media, 2010.

[101] R. F. Haglund. “Photophysics and Photochemistry of Ultrafast Laser Materials Processing”. In: *3D Laser Microfabrication*. John Wiley & Sons, Ltd, 2006, pp. 139–179.

[102] T. P. Mollart et al. “Factors affecting the optical performance of CVD diamond infrared optics”. In: *Semiconductor Science and Technology* 18.3 (2003), S117–S124.

[103] S. Lagomarsino et al. “Photoionization of monocrystalline CVD diamond irradiated with ultrashort intense laser pulse”. In: *Physical Review B* 93.8 (2016), p. 085128.

[104] Y.-C. Chen et al. “Laser writing of coherent colour centres in diamond”. In: *Nature Photonics* 11.2 (2017), pp. 77–80.

[105] S. M. Pimenov et al. “Picosecond-laser bulk modification induced enhancement of nitrogen-vacancy luminescence in diamond”. In: *Journal of the Optical Society of America B* 33.3 (2016), B49–B55.

[106] R. R. Gattass and E. Mazur. “Femtosecond laser micromachining in transparent materials”. In: *Nature Photonics* 2.4 (2008), pp. 219–225.

[107] A. D. Papadopoulos and E. Anastassakis. “Optical properties of diamond”. In: *Physical Review B* 43.6 (1991), pp. 5090–5097.

[108] M. J. Booth, M. a. A. Neil, and T. Wilson. “Aberration correction for confocal imaging in refractive-index-mismatched media”. In: *Journal of Microscopy* 192.2 (1998), pp. 90–98.

[109] A. Jesacher and M. J. Booth. “Parallel direct laser writing in three dimensions with spatially dependent aberration correction”. In: *Optics Express* 18.20 (2010), pp. 21090–21099.

[110] I. Escobar et al. “Reduction of the spherical aberration effect in high-numerical-aperture optical scanning instruments”. In: *Journal of the Optical Society of America A* 23.12 (2006), pp. 3150–3155.

[111] M. Schwertner, M. J. Booth, and T. Wilson. “Characterizing specimen induced aberrations for high NA adaptive optical microscopy”. In: *Optics Express* 12.26 (2004), pp. 6540–6552.

[112] O. H. Y. Zalloum et al. “On femtosecond micromachining of HPHT single-crystal diamond with direct laser writing using tight focusing”. In: *Optics Express* 18.12 (2010), pp. 13122–13135.

[113] T. Kononenko et al. “Microstructuring of diamond bulk by IR femtosecond laser pulses”. In: *Applied Physics A* 90.4 (2008), pp. 645–651.

[114] M. Schwertner, M. J. Booth, and T. Wilson. “Simple optimization procedure for objective lens correction collar setting”. In: *Journal of Microscopy* 217.3 (2005), pp. 184–187.

[115] R. D. Simmonds et al. “Three dimensional laser microfabrication in diamond using a dual adaptive optics system”. In: *Optics Express* 19.24 (2011), pp. 24122–24128.

[116] B. Sun, P. S. Salter, and M. J. Booth. “Pulse front adaptive optics: a new method for control of ultrashort laser pulses”. In: *Optics Express* 23.15 (2015), pp. 19348–19357.

[117] S Lawson et al. “Migration energy of the neutral vacancy in diamond”. In: *Journal of Physics: Condensed Matter* 4.9 (1992), p. L125.

[118] G. Davies et al. “Vacancy-related centers in diamond”. In: *Physical Review B* 46.20 (1992), pp. 13157–13170.

[119] G. Davies. “The effect of nitrogen impurity on the annealing of radiation damage in diamond”. In: *Journal of Physics C: Solid State Physics* 5.17 (1972), pp. 2534–2542.

[120] n. Bernholc et al. “Mechanism of self-diffusion in diamond”. In: *Physical Review Letters* 61.23 (1988), pp. 2689–2692.

[121] A. Mainwood. “Point Defects in Natural and Synthetic Diamond: What They Can Tell Us about CVD Diamond”. In: *Physica Status Solidi A* 172.1 (1999), pp. 25–35.

[122] C. J. Stephen et al. “Deep Three-Dimensional Solid-State Qubit Arrays with Long-Lived Spin Coherence”. In: *Physical Review Applied* 12.6 (2019), p. 064005.

[123] A. Mainwood. “Substitutional impurities in diamond”. In: *Journal of Physics C: Solid State Physics* 12.13 (1979), pp. 2543–2549.

[124] J. O. Orwa et al. “Nickel related optical centres in diamond created by ion implantation”. In: *Journal of Applied Physics* 107.9 (2010), p. 093512.

[125] R. John et al. “Bright optical centre in diamond with narrow, highly polarised and nearly phonon-free fluorescence at room temperature”. In: *New Journal of Physics* 19.5 (2017), p. 053008.

[126] V. Yurgens et al. “Low-Charge-Noise Nitrogen-Vacancy Centers in Diamond Created Using Laser Writing with a Solid-Immersion Lens”. In: *ACS Photonics* 8 (2021), pp. 1726–1734.

[127] M. Watanabe et al. “Two-photon readout of three-dimensional memory in silica”. In: *Applied Physics Letters* 77 (2000), pp. 13–15.

[128] E. N. Glezer et al. “Three-dimensional optical storage inside transparent materials”. In: *Optics Letters* 21 (1996), pp. 2023–2025.

[129] C. B. Schaffer, A. Brodeur, and E. Mazur. “Laser-induced breakdown and damage in bulk transparent materials induced by tightly focused femtosecond laser pulses”. In: *Measurement Science and Technology* 12.11 (2001), pp. 1784–1794.

[130] S. Mao et al. “Dynamics of femtosecond laser interactions with dielectrics”. In: *Applied Physics A* 79.7 (2004), pp. 1695–1709.

[131] L. V. Keldysh. “Ionization in the Field of a Strong Electromagnetic Wave”. In: *Soviet Physics: Journal of Experimental and Theoretical Physics* 20.5 (1965), pp. 1307–1314.

[132] S. C. Jones et al. “Recent Progress On Laser-Induced Modifications And Intrinsic Bulk Damage Of Wide-Gap Optical Materials”. In: *Optical Engineering* 28.10 (1989).

[133] M Hasegawa et al. “Characterisation of nitrogen-implanted CVD homoepitaxial diamond”. In: *Diamond and related materials* 13.4-8 (2004), pp. 600–603.

[134] R Kalish et al. “Nitrogen doping of diamond by ion implantation”. In: *Diamond and Related Materials* 6.2-4 (1997), pp. 516–520.

[135] B. Griffiths et al. “Microscopic processes during ultrafast laser generation of Frenkel defects in diamond”. In: *Physical Review B* 104 (2021), p. 174303.

[136] M. J. Booth et al. “Adaptive aberration correction in a confocal microscope”. In: *Applied Physical Sciences* 99 (2002), pp. 5788–5792.

[137] M. R. Foreman and P. Török. “Computational methods in vectorial imaging”. In: *Journal of Modern Optics* 58 (2011), pp. 339–364.

[138] R. J. Noll. “Zernike polynomials and atmospheric turbulence”. In: *Journal of the Optical Society of America* 66 (1976), pp. 207–211.

[139] F. Zernike and F. J. M. Stratton. “Diffraction Theory of the Knife-Edge Test and its Improved Form, The Phase-Contrast Method”. In: *Monthly Notices of the Royal Astronomical Society* 94 (1934), pp. 377–384.

[140] M. Born and E. Wolf. *Principles of Optics*. 5th ed. United Kingdom: Pergamon Press, 1975.

[141] V. N. Mahajan. “Symmetry properties of aberrated point-spread functions”. In: *Journal of the Optical Society of America A* 11 (1994), pp. 1993–2003.

[142] J. Cui et al. “Generalised adaptive optics method for high-NA aberration-free refocusing in refractive-index-mismatched media”. In: *Optics Express* 30 (2022), pp. 11809–11824.

[143] R. H. Brown and R. Q. Twiss. “A new type of interferometer for use in radio astronomy”. In: *Philosophical Magazine* 45 (1954), pp. 663–682.

[144] C. Kurtsiefer et al. “Stable solid-state source of single photons”. In: *Physical Review Letters* 85 (2000), p. 290.

[145] W. Koch and M. C. Holthausen. *A Chemist’s Guide to Density Functional Theory*. Wiley-VCH Verlag GmbH, 2001.

[146] M. Born and J. R. Oppenheimer. “Zur Quantentheorie der Molekeln”. In: *Annalen der Physik* 389 (1927), pp. 457–484.

[147] A. Szabo and N. S. Ostlung. *Modern Quantum Chemistry*. Dover Publications, Inc, 1996.

[148] S. J. Clark et al. “First principles methods using CASTEP”. In: *Zeitschrift für Kristallographie* 220.5-6 (2004), pp. 567–570.

[149] J. P. Perdew, K. Burke, and M. Ernzerhof. “Generalized Gradient Approximation Made Simple”. In: *Physical Review Letters* 77.18 (1996), p. 4.

[150] M. Ernzerhof and G. E. Scuseria. “Assessment of the Perdew–Burke–Ernzerhof exchange-correlation functional”. In: *Journal of Chemical Physics* 110.11 (1999), pp. 5029–5036.

[151] V Milman et al. “Electronic structure, properties, and phase stability of inorganic crystals: A pseudopotential plane-wave study”. In: *International Journal of Quantum Chemistry* 77.5 (), p. 16.

[152] P. Kratzer and J. Neugebauer. “The basics of electronic structure theory for periodic systems”. In: *Frontiers in chemistry* 7 (2019), p. 106.

[153] H. J. Monkhorst and J. D. Pack. “Special points for Brillouin-zone integrations”. In: *Physical review B* 13.12 (1976), p. 5188.

[154] J. M. Binder et al. “Qudi: A modular python suite for experiment control and data processing”. In: *SoftwareX* 6 (2017), pp. 85–90.

[155] A. M. Zaitsev. *Optical properties of diamond: a data handbook*. Springer Science & Business Media, 2013.

[156] A. Lang. “Causes of birefringence in diamond”. In: *Nature* 213.5073 (1967), pp. 248–251.

[157] P. Deák et al. “Formation of NV centers in diamond: A theoretical study based on calculated transitions and migration of nitrogen and vacancy related defects”. In: *Physical Review B* 89.7 (2014), p. 075203.

[158] S. Salustro et al. “The V + I defects in diamond: An ab initio investigation of the electronic structure, of the Raman and IR spectra, and of their possible recombination”. In: *Journal of Chemical Physics* 145 (2016), p. 184701.

[159] J. P. Perdew, M. Ernzerhof, and K. Burke. “Rationale for mixing exact exchange with density functional approximations”. In: *The Journal of chemical physics* 105 (1996), pp. 9982–9985.

[160] C. Adamo and V. Barone. “Toward reliable density functional methods without adjustable parameters: The PBE0 model”. In: *The Journal of chemical physics* 110 (1999), pp. 6158–6170.

[161] D. R. Hamann, M. Schlüter, and C. Chiang. “Norm-Conserving Pseudopotentials”. In: *Physical Review Letters* 43.20 (1979), pp. 1494–1497.

[162] G. B. Bachelet, D. R. Hamann, and M. Schlüter. “Pseudopotentials that work: From H to Pu”. In: *Physical Review B* 26.8 (1982), p. 4199.

[163] G. Kerker. “Non-singular atomic pseudopotentials for solid state applications”. In: *Journal of Physics C: Solid State Physics* 13.9 (1980), p. L189.

[164] A. Gali. “Ab initio theory of the nitrogen-vacancy center in diamond”. In: *Nanophotonics* 8 (2019), pp. 1907–1943.

[165] J. Heyd and G. E. Scuseria. “Hybrid functionals based on a screened Coulomb potential”. In: *Journal of Chemical Physics* 118 (2003), p. 8207.

[166] J. Paiera et al. “Screened hybrid density functionals applied to solids”. In: *Journal of Chemical Physics* 124 (2006), p. 154709.

[167] J. Paiera et al. “Erratum: “Screened hybrid density functionals applied to solids” [J. Chem. Phys. 124, 154709 (2006)]”. In: *Journal of Chemical Physics* 125 (2006), p. 249901.

[168] G. Davies. “Dynamic Jahn-Teller distortions at trigonal optical centres in diamond”. In: *Journal of Physics C: Solid State Physics* 12 (1979), pp. 2551–2566.

[169] A. Batalov et al. “Low Temperature Studies of the Excited-State Structure of Negatively Charged Nitrogen-Vacancy Color Centers in Diamond”. In: *Physical Review Letters* 102 (2009), p. 195506.

[170] P Olivero et al. “Splitting of photoluminescent emission from nitrogen–vacancy centers in diamond induced by ion-damage-induced stress”. In: *New Journal of Physics* 15.4 (2013), p. 043027.

[171] A. R. Lang et al. “On the dilatation of synthetic type Ib diamond by substitutional nitrogen impurity”. In: *Philosophical Transactions of the Royal Society A* 337.1648 (1991), pp. 497–520.

[172] K. Iakoubovskii and G. J. Adriaenssens. “Trapping of vacancies by defects in diamond”. In: *Journal of Physics: Condensed Matter* 13 (2001), p. 5.

[173] M. J. Rutter. “C2x: a tool for visualisation and input preparation for Castep and other electronic structure codes”. In: *Computer Physics Communications* 225 (2018), pp. 174–179.

[174] E. B. Lombardi et al. “Computational models of the single substitutional nitrogen atom in diamond”. In: *Journal of Physics: Condensed Matter* 15.19 (2003), pp. 3135–3149.

[175] H. Pinto et al. “On the diffusion of NV defects in diamond: On the diffusion of NV defects in diamond”. In: *Physica Status Solidi A* 209.9 (2012), pp. 1765–1768.

[176] T. Kurita et al. “Efficient generation of nitrogen-vacancy center inside diamond with shortening of laser pulse duration”. In: *Applied Physics Letters* 113 (2018), p. 211102.

[177] B. J. Berne, G. Ciccotti, and D. F. Coker. *Classical and quantum dynamics in condensed phase simulations: Proceedings of the International School of Physics*. World Scientific, 1998.

[178] B. Griffiths. “Laser engineering of defects in diamond for quantum technologies”. PhD thesis. University of Oxford, 2021.

[179] C. A. Coulson and M. J. Kearsley. “Colour centres in irradiated diamonds. I”. In: *Proceedings of the Royal Society A* 241 (1957), p. 433.

[180] T. Yamaguchi. “Electronic states of single vacancies in diamond”. In: *Journal of the Physical Society of Japan* 17 (1962), p. 1359.

[181] C. A. Coulson and F. P. Larkins. “Electronic structure of the neutral isolated divacancy in diamond”. In: *Journal of Physics and Chemisty of Solids* 30 (1969), p. 1963.

[182] H. Deschout et al. “Precisely and accurately localizing single emitters in fluorescence microscopy”. In: *Nature methods* 11.3 (2014), pp. 253–266.

[183] M. P. Backlund et al. “Simultaneous, accurate measurement of the 3D position and orientation of single molecules”. In: *Proceedings of the National Academy of Sciences* 109.47 (2012), pp. 19087–19092.

[184] S. Stallinga and B. Rieger. “Position and orientation estimation of fixed dipole emitters using an effective Hermite point spread function model”. In: *Optics express* 20.6 (2012), pp. 5896–5921.

[185] F. Aguet et al. “Super-resolution orientation estimation and localization of fluorescent dipoles using 3-D steerable filters”. In: *Optics express* 17.8 (2009), pp. 6829–6848.

[186] K. I. Mortensen et al. “Optimized localization analysis for single-molecule tracking and super-resolution microscopy”. In: *Nature methods* 7.5 (2010), pp. 377–381.

[187] P. Grivickas et al. “Carrier recombination and diffusion in high-purity diamond after electron irradiation and annealing”. In: *Applied Physics Letters* 117 (2020), p. 242103.

[188] H. Morimoto et al. “Exciton lifetime and diffusion length in high-purity chemical-vapor-deposition diamond”. In: *Diamond & Related Materials* 63 (2016), pp. 47–50.

[189] B. Slepetz and M. Kertesz. “Divacancies in diamond: a stepwise formation mechanism”. In: *Physical Chemistry Chemical Physics* 16 (2014), pp. 1515–1521.

[190] M. Matsumoto and T. Nishimura. “Mersenne twister: a 623-dimensionally equidistributed uniform pseudo-random number generator”. In: *ACM Transactions on Modeling and Computer Simulation* 8 (1998), pp. 3–30.

[191] K. Iakoubovskii et al. “Annealing of vacancies and interstitials in diamond”. In: *Physica B: Condensed Matter* 340-342 (2003), pp. 67–75.

[192] S. Eaton et al. “Heat accumulation effects in femtosecond laser-written waveguides with variable repetition rate”. In: *Optics Express* 13 (2005), pp. 4708–4716.

[193] R. Courant, K. Friedrichs, and H. Lewy. “Über die partiellen Differenzengleichungen der mathematischen Physik”. In: *Mathematische Annalen (in German)* 100 (1928), pp. 32–74.